Development of the Clinical Application of miRNA with Proregenerative Effect on the Heart

Thesis

Development of the Clinical Application of miRNA with Pro-regenerative Effect on the Heart

Giulia Prosdocimo

A Thesis submitted in fulfilment of the requirements of the Open University (UK) for the degree of Doctor of Philosophy

The Open University (UK)

International Centre for Genetic Engineering and Biotechnology (ICGEB), Trieste, Italy

Director of the studies: Prof. Mauro Giacca
External supervisor: Prof. Costanza Emanueli

Submitted January, 2018

TABLE OF CONTENTS

ACKNOWLEDGMENTS

I am very grateful to Professor Mauro Giacca for the opportunity to work in the Molecular Medicine Group at the ICGEB in Trieste and for the great scientific mentorship over the last years. I also wish to thank Dr. Serena Zacchigna for the all the fruitful discussions we have had during my PhD studies, Prof. Rossana Bussani for having guided me through the immunohistochemical analysis of pig samples and Drs. Lorena Zentilin and Chiara Collesi for the great scientific and personal support.

A special thanks goes to all my colleagues at ICGEB, in particular to Ilaria, Consuelo, Nadja, Alice, Francesca, Silvia, Michele, Valentina, Elena, Giulia, Luca, Edoardo and Hashim.

I would like to thank the ICGEB for the stimulating environment and the financial support.

CONTRIBUTIONS

For the work reported in this Thesis, I wish to acknowledge the essential contributions of:

- Prof. Fabio Recchia, Dr. Kathia Gabisonia and Dr. Giovanni Aquaro, for performing all the experimental procedures in pigs, including surgery and MRI analysis, which were held at the Istituto di Fisiologia Clinica of the CNR in Pisa, Italy;
- Dr. Lorena Zentilin and Ms. Marina Dapas at the ICGEB AAV Vector Unit for the generation of AAV vectors;
- Drs. Pierluigi Lesizza and Simone Vodret for performing surgery and echocardiography in mice.

LIST OF ABBREVIATIONS

2'-F	2'-fluoro
2'-MOE	2'-O-methoxyethyl
2'-OMe	2'-O-methyl ribose-modified RNA
A	anterior
AAR	area at risk
AAV	Adeno-associated virus
AKT	Protein kinase B
AL	anterolateral
AMI	Acute myocardial infarction
ANP	atrial natriuretic peptide
AS	anteroseptal
AUC	area under curve
BNP	brain natriuretic peptide
BRDU	5-bromo-2'-deoxyuridine
BSA	bovine serum albumin
BZ	border zone
CDK	cyclin dependent kinase
Chr	Chromosome
CM	cardiomyocyte
CMRI	cardiac magnetic resonance
CSC	cardiac stem cell
DAG1	destroglycan 1
DDR	DNA damage repair
DGC	dystrophin-glycoprotein complex
DGCR8	DiGeorge syndrome chromosomal [or critical] region 8
DNM2	Dynamin 2
ECC	circumferential strain
EDT	end-diastolic thickness

EdU	ethynyl-29-deoxy-uridine
EF	ejection fraction
EGR1	Early growth response protein 1
EL	elongation
ERK	extracellular signal-regulated kinases
ERR	radial strain
ESC	embryonic stem cell
EST	end-systolic thickness
FBS	fetal bovine serum
FGF1	fibroblast growth factor 1
FSTL1	Follistatin-like 1
Gd-DE	gadolinium delayed enhanced
Gd-DTPA	gadolinium diethylenetriamine penta-acetic acid
GSK3β	Glycogen synthase kinase-3
H&E	Hematoxylin and eosin
HAND2	Heart- and neural crest derivatives-expressed protein2
HCC	hepatocellular carcinoma cell line
hfCM	human fetal cardiomyocyte
HGF	hepatocyte growth factor
HIF1α	Hypoxia-inducible factor 1-alpha
HSPG	Heparan sulfate proteoglycan
I	inferior
I.V.	intravenous
I/R	ischemia reperfusion
IGF1	insulin-growth factor 1
IL	inferolateral
iPS	induced pluripotent stem cell
IRX5	Iroquois homeobox protein 5
IS	inferoseptal
ITRs	long inverted terminal repeats

IV	intravenous
IVSd	Interventricular septal end diastole
KO	knock out
L	lateral
LAD	left anterior descending coronary artery
LGE	late gadolinium enhancement
LNA	locked nucleic acid
LV	left ventricle
LVAWd	left ventricle anterior wall end dyastole
LVAWs	left ventricle anterior wall end systole
LVECC	left ventricle circumferential strain
LVEDV	left ventricle end diastolic volume
LVERR	left ventricle radial strain
LVWT	Left ventricle wall thickening
MAP3K11	Mitogen-activated protein kinase kinase kinase 11
MEF2C	myocyte-specific enhancer factor 2C
MI	myocardial infarction
MiRNA	microRNA
mRNA	messanger RNA
MTOR	mechanistic target of rapamycin
MYH6	myosin heavy chain 6
NLS	nuclear localization signal
NOS	Nitric oxide synthases
NRG1	Neuregulin1
PAS	periodic acid-shiff
PBS	phosphate buffer saline TBS
PDGF	Platelet-derived growth factor
PE	phenylephrine
PET	positron emission tomography
pH3	phospho histone 3

PLGA	poli-lactide-co-glycolide
PPAR-γ	peroxisome proliferator-activated receptor gamma
PTEN	phosphatase and tensin homolog
RISC	RNA-induced silencing complex
S	septal
SAV	Salvador
SD	signal density
SEM	standard error mean
SI	signal intensity
siRNA	short interfering RNA
SRF	serum response factor
STAT3	Signal transducer and activator of transcription 3
TAC	transient aortic constriction
TAZ	Tafazzin
TBX5	T-box protein 5
TRBP	TAR-RNA binding protein
TUNEL	Terminal Uridine Nick-End Labeling
UTR	untranslated region
VEGF	vascular endothelial growth factor
VF	venticular fibrillation
vPLA2	viral phospholipase A2
WGA	wheat germ agglutinin
WNT	Wingless pathway
WT	wall thickening
YAP	Yes-associated protein

WT	wall thickening
YAP	Yes-associated protein

ABSTRACT

Rationale: Cardiovascular disorders are the first cause of mortality and morbidity worldwide. This is due, at least in part, to the poor regenerative capacity of the heart and the lack of drugs able to foster cardiac regeneration. Our recent work has identified a few human microRNAs (miRNAs), in particular hsa-miR-199a-3p, able to stimulate proliferation of cardiomyocytes and, once expressed in the mouse heart using viral vectors, to induce cardiac regeneration after myocardial infarction.

Objective: As a first step towards clinical translation, in this study we assess the efficacy of the pro-regenerative miR-199a after myocardial infarction, delivered using an AAV vector in a pig model of ischemia-reperfusion and as a synthetic RNA molecule after a single intracardiac injection in mice.

Methods and Results: We evaluated the efficacy of miR-199a in a pig model of ischemia-reperfusion after direct myocardial injection of an AAV6 vectors carrying the miR-199a precursor. Cardiac function was evaluated at days 2 and 28 by gadolinium-enhanced cardiac magnetic resonance imaging (cMRI). The results showed significant reduction of infarct size and increased cardiac function in the animals treated with AAV6 miR-199a at one month after treatment. Histological analysis uncovered a significant increase in cardiomyocyte proliferation in the infarct border zone, paralleled by the expression of markers of cardiomyocyte de-differentiation. Despite these remarkably positive signs of cardiac regeneration, pigs treated with AAV6-miR-199a died of sudden death at weeks 7-8 after treatment. In three of these pigs, clusters of small, proliferating cells with a phenotype of undifferentiated myogenic progenitors were apparent.

In parallel, we comparatively analyzed the efficacy different lipid formulations in delivering hsa-miR-199a-3p as a naked RNA mimic in both primary neonatal rat cardiomyocytes and in vivo. We established a transfection protocol allowing persistence of miR-199a-3p mimics, carrying different chemical modifications, for at least 12 days after a single intracardiac injection, with minimal dispersion to other organs and long-term preservation of miRNA functional activity, as assessed by monitoring the expression of two direct mRNA targets. We administered this synthetic formulation immediately after myocardial infarction in mice and found that a single intracardiac injection was sufficient to reduce scar size and improve global cardiac function up to

two months. Histology confirmed reduced scar extension and immunofluorescence showed increased cardiomyocyte proliferation in the miR-199a-3p mimic injected animals.

Conclusions: AAV6-miR-199a injection after ischemia-reperfusion in pigs significantly improves cardiac function and reduce scar size. However, AAV6-driven miR-199a persistent expression in the pig myocardium is fraught with safety issues.

A single administration of mir-199a-3p mimic is sufficient to stimulate adult mouse cardiac repair and restoration of cardiac function. Together, these results are concordant in indicating that a miRNA-based therapy aimed at inducing cardiomyocyte proliferation might be pursued to stimulate cardiac regeneration, however that the duration of the miRNA effect needs to be tightly controlled.

1. INTRODUCTION

1.1 Myocardial infarction and heart failure still remain unsolved diseases

Heart failure is the most common outcome of cardiomyocyte dysfunction or death, which is most frequently caused by myocardial infarction, hypertension, valve disease, infection, chemotherapy or genetic cardiomyopathy [1].

It represents a global disease challenge that affects 38 million people worldwide [2] and is the leading cause of hospitalization, adverse quality of life, and death. Its survival rate is only 50% at 5 years, which is worse than many types of cancer, and the incidence may be even increasing owing to improved early survival with primary percutaneous coronary intervention after myocardial infarction.

Existing therapies target the maladaptive counter-regulatory mechanisms activated in a chronic phase by left ventricular dysfunction after damage. After acute myocardial infarction, for example, loss of cardiomyocytes for ischemic death, which occurs in the first hours, is followed by a cascade of compensatory mechanisms, detrimental for global heart function. Ventricular dilatation, scar thinning and activation of interstitial fibrosis characterize heart remodeling weeks and months after the acute event. Impaired cardiac output prompts the activation of neurohormonal systems that act to maintain the circulation [3]. Release of angiotensin II and aldosterone drive sodium and fluid retention, and adrenergic system activation sustains blood pressure through vasoconstriction [4]. These mechanisms are primarily compensatory but become maladaptive, causing fluid overload, myocardial hypertrophy and slow but ongoing cardiomyocyte death, which leads to additional deterioration of ventricular function [3]. Over the last 20 years, treatments aimed to inhibit the renin-angiotensin system, mineralocorticoid receptor, sympathetic nervous system and natriuretic system have delayed just partially the progression of heart failure. Even if current drugs diminish mortality, they fail to address the loss of cardiomyocytes and vasculature, remaining intrinsically non-curative.

Cardiomyocyte replacement to restore structural and functional integrity is the prerequisite of heart regeneration, which will could eventually solve the heart failure syndrome problem.

1.1.1 Evidences of heart regeneration in mammals

One of the first reports documenting heart regeneration in mammals was provided by Porrello et al. in 2011. At post-natal day 1 (P1), mice regenerated the myocardium after apical resection, but this capacity was lost by 7 days of age [5]. The regenerative process, monitored for 2 months after injury, was characterized by cardiomyocyte proliferation and minimal fibrotic response. Analogously, P1 mice heart is able to regenerate after acute myocardial infarction induced by permanent coronary artery ligation by activating an extensive cardiomyocyte proliferation driven by pre-exsisting cardiomyocytes and, consequently, resulting in full functional recovery within 21 days with minimal residual scarring [6]. These reports prompt one to conclude that there is a possibility for endogenous heart regeneration, without the need of implanting exogenous cells, albeit in a limited window during the first week after birth.

The irrefutable proof that neonatal heart regeneration occurs by pre-existing cardiomyocytes was given by genetic lineage tracing experiments in which MerCreMer^{+}/ZEG mice had been treated with tamoxifen to irreversibly label cardiomyocytes with green fluorescent protein (GFP) and with [^{15}N] thymidine to trace DNA synthesis in cardiomyocytes [7]. The results of this study revealed that pre-existing cardiomyocytes are the dominant source of cardiomyocyte replacement in mice during aging and after infarction. Cell cycle activation in cardiomyocytes in both conditions led to polyploidy and multinucleation but also to new diploid, mononucleated cardiomyocytes with a rate of 0.76% per year in young adult mice, which decreases decreased in aging animals [7]. However, in the infarct border zone of adult mice, only 3.2% of cardiomyocytes initiate DNA synthesis and are able to unambiguously undergo cell division [7].

More recently, a few intriguing case reports supported the concept of a temporally privileged period of regenerative repair also in humans. A newborn infant with a large anterior myocardial infarction displayed healing by regeneration with full functional recovery 7 weeks after ischemia [8]. Another case report of functional regeneration and lack of scarring after cardiac corrective surgery for congenital heart disease in children [9] indicated that, similar to neonatal rodents, newborn humans might have the intrinsic capacity to repair myocardial damage and completely recover cardiac function.

Up to now, there are no extensive studies describing cardiomyocyte proliferation after myocardial infarction in humans. However, histological analysis of the healthy human heart has identified positivity for phosphorylated histone H3 in healthy young and

adolescent hearts up to the age of 20 years [10], indicating that, as it occurs in mice, young human cardiomyocytes maintain a proliferative capacity limited to the first years of life. Proliferation rate in adult humans has been further studied using the worldwide pulse of C14 that occurred during the atmospheric testing of nuclear weapons in the cold war years [11]. Atmospheric C14 became incorporated into plants and entered the human food chain, labelling the DNA of dividing cells. After the treaty of 1963, which limited nuclear tests, the C14 atmospheric levels dropped rapidly. Work performed by C14 quantification of DNA extracted from cardiomyocytes of individuals of different age has indicated that cardiomyocyte renewal is age-dependent, with about 1% of cells being renewed per year at age 20, and 0.4% at age 75; this means that about 45% of cardiomyocytes are renewed over a normal lifespan, whereas 55% of cardiomyocytes persist since birth [11].

Taken together, these studies provide strong evidence for a limited regenerative potential of the human heart, however, the extent of endogenous proliferation is clearly poor to provide full cardiomyocyte replacement after myocardial infarction.

1.1.2 Strategies for therapeutic regeneration

Replacement of dead cardiomyocytes is the *sine qua non* condition to reestablish cardiac structural and functional integrity after myocardial infarction.

In the last years different research lines have aimed at restoring loss of cardiomyocytes by:

- Transplantation and/or activation of progenitor populations
- Exogenous cardiomyocyte replacement (autologous or allogenic)
- Reprogramming fibroblasts to cardiomyocytes
- Activating pre-existing cardiomyocyte proliferation.

Among the category of studies that aimed to transplant and/or activate progenitor populations, many efforts were made in order to replace cardiomyocyte loss with bone-marrow derived-progenitors, which have been reported to differentiate into cardiomyocytes [12]. Even though the differentiation of these cells to cardiomyocytes was later discredited [13], many clinical trial for the treatment of acute myocardial infarction have been performed in the subsequent years (Strauer et al. in 2002, Perin et al. in 2003, BOOST in 2004, ASTAMI in 2006, REPAIR-AMI and Jannsens et al. in 2006,

FOCUS-CCTRN in 2012, SWISS-AMI in 2013 and REGENERATE-AMI in 2016); for meta-analysis of these studies, cf. refs: [14] [15] [16] [17] [18] [19] [20] [21] [22]. The overall oucome of these clinical trials has indicated only modest improvement in left ventricle ejection fraction, which can be ascribed to the promotion of tissue survival and the neoangiogenetic effects of the implanted cells, exerted in a paracrine fashion.

Several types of resident cardiac progenitor (or stem) cells have been reported to reside in the adult heart, recognizable by the expression of surface markers, including c-Kit, Sca1 or PDGFRα, or by the ability to form cardiospheres in colture [23]. The more studied and debated cells are the so-called c-Kit$^+$ progenitors, which a highly disputed report in 2001 has shown to be able to regenerate up to 70% of the infarcted myocardium in mice [24]. Following that original report, a number of studies have followed, several of which have apparently reproduced, entirely or partially the originally described property of these putative c-Kit progenitors (the last relevant one being by G. Ellison and N. Bernard Ginard [25], while several others disputing the effect (cf., among several, the study by J. Mokentin and collaborators [26]). Currently, there is ample consensus that these cardiac c-Kit-positive cells are not cardiogenic [27] [28].

The possibility to perform a large-scale production of cardiomyocytes from induced pluripotent stem cells [29] or embryonic stem cells (ESC) has paved the way to restore cardiomyocyte loss after myocardial infarction by exogenous, autologous or allogenic, cell transplantation. After several reports demonstrating human ESC-derived cardiomyocyte survival, engraftment, maturation and proliferation in rodent hearts after infarction [30] [29] [31] ESC- and iPS-derived cardiomyocytes were tested in non-human primate hearts [32] [33]. The implanted cells were able to survive for at least 3 months after transplantation and induce a very significant re-muscularization of the infarcted heart. The transplanted cells were perfused by host vasculature and synchronized to the host electrocardiogram, thus indicating electromechanical coupling [32] [33]. However, beside the success obtained by this study, the use of ESC- and iPS-derived cardiomyocytes still has significant limitations. First, immunosuppression is required in the case of ESC-derived cardiomyocytes, which has a negative impact on patient morbidity and mortality. Second, ESC- and iPS-derived cardiomyocytes production requires still formidable time and cost. In fact, to replace the loss of cardiomyocytes of a myocardial infarction in humans, at least one billion cells would be needed, also considering that, at the time of injection, most of the cells die or are washed out. Finally, but most important, ventricular arrhythmias were recorded in

all animals so far treated, suggesting that significant hurdles with electrical integration remain before human trials could safely be undertaken [34].

The discovery, in 2010, that the delivery of three transcription factors GATA4, myocyte-specific enhancer factor 2C (MEF2C) and T-box protein 5 (TBX5) is able to drive direct reprogramming of fibroblasts to cardiomyocytes, without an intermediate cell stage [35], has opened the door to the direct reprogramming *in vivo*. Some years later several other factors have been reported to be able to induce reprogramming, including as miR-1, miR-133, miR-208 and miR-499 [36], or to enhance reprogramming driven by the three factors, as HAND2 [37]. Proofs of *in vivo* reprogramming has been demonstrated in mouse models, in which transdifferentiated cardiomyocytes express sarcomeric proteins, are able to form gap junctions and drive sustained improvement in ventricular function and reduce adverse ventricular remodeling following myocardial infarction [37]. Considerable challenges in the direct reprogramming approach remain, including achieving selectivity of targeting to the heart, reprogramming human cells that have stable epigenetic modifications and achieving maturation of structure and function in reprogrammed cells.

Among the approaches cited above, exogenous cardiomyocyte replacement (with autologous iPS-derived cardiomyocytes, or allogenic iPS- or ESC-derived cardiomyoctes) and fibroblast reprogramming might become new alterative and effective treatments to replace the loss of functional contractile cells. For the limitations mentioned, however, the possibility of their use in a clinical trial remains still quite remote.

An alternative, currently more appealing, possibility entailsthe reactivation of endogenous cardiomyocyte proliferation, which will be more extensively reviewed in the next paragraph.

1.1.3 Activation of cardiomyocyte proliferation

1.1.3.1 Cell cycle regulation by targeting cyclin-CDK system

The first effort to reactivate cardiomyocyte proliferation was made by targeting the cyclin-CDK pathway, which controls progression of the cell cycle. In particular, the overexpression of Cyclin A2 [38], B1 [39], and D2 [40] or the inhibition of the CDK inhibitors $p21^{Waf1}$, $p27^{Kip1}$ and $p57^{Kip2}$, effectively stimulate DNA replication *in vitro*. In addition, the overexpression of cyclin A2 and D2 also stimulates DNA synthesis *in vivo*.

Remarkably, the targeted expression of cyclin D2 in cardiomyocytes was shown to also boosts repair of the injured myocardium after infarction [40].

An alternative, interesting strategy to achieve cardiomyocytes replication is by modulating the levels MEIS1, a critical regulator of cardiomyocyte cell-cycle, required for transcriptional activation of the synergistic CDK inhibitors p15, p16 and p21 [41]. The deletion of this gene in mouse cardiomyocytes is sufficient to extend the postnatal proliferative window, and reactivate cardiomyocyte mitosis and cytokines in the adult heart with no apparent deleterious effects on cardiac function [41]. In contrast, the overexpression of MEIS1 limits neonatal heart regeneration after myocardial infarction [41].

1.1.3.2 Epicardial- and other growth-factor-induced cardiomyocyte proliferation

A few growth factors have been shown to be able to stimulate cardiomyocytes proliferation. By far the most effective of these factors appears to be neuregulin1 (NRG1), which, by binding its cognate ERBB tyrosine kinase receptors, was shown to induce mononuclate but not binucleated cardiomyocyte to divide [42]. It was suggested that soluble recombinant NRG1 injection in adult mice is sufficient to stimulate cell-cycle activity and promote myocardial regeneration after infarction [42], a finding that, however, has been later challenged [43]. Indeed, NRG1-mediated proliferation appears to be limited to embryonic/neonatal life up to postnatal day 7 and that this is promoted by its co-receptor ERBB2, the expression of which decreases after the first week of life [44]. Transient induction of ERBB2 after myocardial infarction triggers cardiomyocyte dedifferentiation and proliferation followed by re-differentiation and regeneration by ERK-, AKT- and GSK3/and GSK3i-mediated signaling [44]. Thus, NRG1 and ERBB2 are both necessary to reactivate postnatal proliferation and induce regeneration. An evidence of the therapeutic potential of this system came from a phase I trial of recombinant NRG1 β 3 administration in patients with chronic hear failure. This study demonstrated safety of treatment and improvement of left ventricular function at 90 days after delivery [45].

Similar to NRG1, fibroblast growth factor 1 (FGF1) delivery, plus simultaneous inhibition of p38 MAP kinase, increased cardiomyocyte mitosis in 8- to 10- weeks old rats after myocardial infarction [46]. While p38 MAP kinase inhibition alone failed to rescue heart

function despite increased cardiomyocyte mitosis, FGF1 improved angiogenesis, possibly contributing to the survival of the newly generated cardiomyocytes [46].

More recently, it became evident that the epicardium has a role in cardiac regeneration. Follistatin-like 1 (FSTL1), an epicardial cardiomyogenic factor, when delivered through epicardial patches as a recombinant protein, boosts cell-cycle reentry and division of pre-exsisting cardiomyocytes, improving cardiac function and survival in mouse and swine models of myocardial infarction [47]. Its loss leads to maladaptive response to injury, while its restoration represents an effective way to reverse cardiomyocyte death and heart remodeling after myocardial infarction [47].

1.1.3.3 Hippo pathway modulation

Hippo signaling is a conserved pathway that controls cellular proliferation and organ size through phosphorylation of final effectors, the transcriptional coactivators YAP and TAZ. In brief, in resting cardiomyocytes, YAP is maintained inactive in the cytoplasm by phosphorylation by a kinase cascade signaling. Mst1/2 (Hippo in Drosophila, in which the pathway was originally discovered by genetic screens [48] [49], in complex with Sav1, phosphorylates and activates LATS1/2, which associates with Mob1 and in turn phosphorylates and inactivates YAP. Genetic deletion of MST1, SAV1 and LATS determines cardiac hyperplasia [50], while overexpression of MST1 [51] or LATS2 [52] leads to post-natal dilated cardiomyopathy, supporting the essential role of this pathway in the regulation of cardiomyocyte proliferation during embryonic and fetal development. Consistent with this notion, transgenic mice overexpressing activated YAP or lacking functional Mst1 both repair myocardial injury through regeneration instead of fibrosis [53] [54].

Chromatin immunoprecipitation experiments have revealed that Hippo signaling negatively regulates a subset of Wnt target genes (such as *Snai2* and *Sox2*). In Sav KO mice, in which YAP is constitutively activated, β-catenin is increased 4-fold in the nucleus of cardiomyocytes. Chromatin immunoprecipitation analysis has revealed that YAP interacts with β-catenin, a positive regulator of cardiac growth, and colocalize on common regulatory sequences downstream the *Snai2* and *Sox2* genes. These experiments suggest the existence of a mechanism by which the opposite action of Hippo and Wnt pathways control cardiomyocyte proliferation and heart size [50].

In addition, it is known that YAP activates insulin-like growth factor (IGF) signaling pathway in cardiomyocytes, resulting in inactivation of glycogen synthase kinase 3β which led to increased abundance of β-catenin [55]. Therefore, YAP couples the IGF, Wnt and Hippo signaling pathways with the developmental program for heart growth.

More recent publications have disclosed a link between the Hippo pathway, the sarcomere and the extracellular matrix. In non-regenerative adult cardiomyocytes, phosphorylated YAP (the inactive form of YAP) is sequestered by destroglycan 1 (Dag1), a component of dystrophin-glycoprotein complex (DGC), a multiprotein transmembrane complex linking the actin cytoskeleton to extracellular matrix which is able of sensing mechanical and biomechanical inputs to inhibit YAP-mediated pro-proliferative and pro-regenerative gene transcription [56]. In addition, the extracellular matrix protein agrin, during neonatal life, binds Dag1 and decreases DGC complex stability, subsequently leading to myofiblil disassembly and activation of downstream signaling molecules including YAP and ERK [57]. When agrin is overexpressed in adult cultured cardiomyocytes, it induces dedifferentiation and sarcomere disassembly. While, *in vivo,* a single injection of recombinant agrin promotes cardiac regeneration in adult mice after myocardial infarction, although the modest degree of cardiomyocyte proliferation suggests that there might be additional therapeutic mechanisms [57].

1.2 MicroRNAs in cardiac regeneration

1.2.1 MicroRNA biology

MicroRNAs (miRNAs) are short (20-23 nucleotides), endogenous, double-stranded RNA molecules that regulate gene expression by binding specific mRNAs both in physiological and pathological processes, including development and cancer [58].

The first precursor of miRNA, the pri-miRNA, is transcribed by RNA polymerase II (pri-miRNAs are polyadenylated and capped) or by RNA polymerase III, which transcribes miRNAs from clusters [59]. The pri-miRNA is next cleaved by the nuclear microprocessor complex formed by the RNase III enzyme Drosha and the DGCR8 protein (also known as Pasha, Partner of Drosha) [60]. This allows the formation of pre-miRNAs, short stem loop structures of 65–75 nucleotides. However, the processing by Drosha/DGCR8 is not compulsory for every miRNA: they can derive from introns and can be released from

their host transcript after splicing [61]. The pre-miRNA is recognized thanks to the defined length of the double stranded RNA and the 3' overhangs by Exportin-5, which in complex with Ran-GTP mediates the export into the cytoplasm [62]. In the cytoplasm, a protein complex (RISC) guides the miRNA to its target mRNAs. The assembly of RISC is guided by the RNase Dicer, Ago 2, the core component, and other proteins such as TRBP and PACT. Once in the cytoplasm, the pre-miRNA is cleaved by Dicer, which removes the loop and generates a 22-nucleotide miRNA duplex with two nucleotides protruding as overhangs at each 3' end [63]. After this cleavage, the double strand duplex is separated by helicases (as p68, p72) into the functional guide strand, complementary to the target, and the passenger strand, which is degraded. Generally, the miRNA strand with the less stable base pair at its 5' end in the duplex is loaded in RISC and will target the mRNA [64] [65]. The mature miRNA binds the mRNA 3'-untranslated region (3'UTR) and silences the target mRNA through sequestration, translational repression or mRNA degradation.

MicroRNAs represent a relatively old and relevant regulatory pathway, as also testified by the fact that the sequences of many miRNAs are homologous among different organisms [64]. They act as key regulators of processes as diverse as early development, cell proliferation, differentiation and apoptosis, brain development, immune system control, angiogenesis, fat metabolism and myocardial function [66].

MicroRNAs are fundamental for the correct cardiac development and function: Dicer knock-out during early stages of life or selectively in adulthood (resulting in the ablation of all microRNAs) causes severe heart failure and death [67]. Additionally, many gain- and loss-of-function studies have emphasized the role of single microRNA or microRNA families as regulators of cardiac disease, fostering the possibility to use these microRNAs as either biomarkers or targets for novel therapies [68, 69]. In particular, numerous microRNAs have been described as regulators of specific processes in cardiac biology as cardiomyocyte contractility miR-208a [70], cardiac fibrosis miR-29 [71], miR-21 [72], cardiomyocyte hypertrophy miR-1 [73], miR-133 [74], miR-195 [75], miR-199b [76], miR-212/132 family [77], miR-378 [78], miR-23a [79], and cardiomyocyte proliferation miR-1 [80], miR-133a [81], miR-199a-3p and miR-590-3p [82].

A detailed description of the most relevant microRNAs in the context of the induction of cardiomyocyte proliferation is reported in the following sections.

1.2.2 Anti-proliferative micro-RNAs

1.2.2.1 MiR-1

MiR-1 is expressed in cardiac and skeletal muscle where it is transcriptionally regulated by the myogenic differentiation factors, MyoD, Mef2, and serum response factor (SRF) [83]. MiR-1 deletion results in 3-fold upregulation of cardiomyocyte proliferation at postnatal day 10; however, it is also associated with large ventricular septal defects during embryogenesis and cardiac electrophysiology defects, by targeting IRX5, which determines sudden death [80]. In contrast, overexpression of miR-1 in mouse cardiac progenitors, where it targets the transcription factor Hand2 - which determines myocyte expansion - exerts a negative effect on proliferation [83].

1.2.2.2 MiR-15 family

The miR-15 family was identified from a microarray analysis as one of the strongest upregulated microRNAs (6-fold induction) in P10 mouse ventricles compared to P1 [6]. One of the members of this family, miR-195, directly targets cell cycle genes, in particular Chekpoint kinase I (Check-1) [84]. The precocious overexpression of miR-195 in embrionic heart is associated with ventricular hypoplasia and ventricular septal defects [6]. Later on, the inhibition of the miR-15 family starting at an early postnatal age until adulthood increases myocyte proliferation and improves left ventricular systolic function after MI in adult mice [6]. This renders this miRNA an attractive therapeutic target to re-stimulate cardiomyocyte division for regenerative purposes.

1.2.3 Pro-proliferative micro-RNAs

1.2.3.1 MiR-133a

MiR-133a-1 and miR-133a-2, whose sequence is identical, are muscle-specific miRNAs regulated during muscle development [85]. Deletion of both miR-133-1 and miR-133-2 causes lethal ventricular-septal defects in approximately half of double-mutant embryos or neonates, while the other half, which survive to adulthood, succumb to dilated cardiomyopathy and heart failure [81]. The absence of miR-133a expression

leads to ectopic expression of smooth muscle genes in the heart and aberrant cardiomyocyte proliferation due to elevated expression of SRF and cyclin D2, which are targets for repression by miR-133a [81].

1.2.3.2 MiR-17/92 cluster

The miR-17/92 cluster was initially described as a human oncogene, richly expressed by a variety of human cancers [86, 87] and as a regulator of embryonic cell proliferation [87]. Chen et al. have demonstrated that transgenic overexpression of miR-17–92 in cardiomyocytes is sufficient to induce cardiomyocyte proliferation in embryonic, postnatal, and adult hearts [88]. In addition, overexpression of miR-17–92 in adult cardiomyocytes protects the heart from myocardial infarction-induced injury increasing cardiomyocyte proliferation by targeting phosphatase and tensin homolog (PTEN) [88].

1.2.3.3 MiR-302-367 cluster

The miRNA cluster miR-302-367 is expressed during early embryogenesis and is important for cardiomyocyte proliferation during development [89]. These microRNAs act by inhibiting upstream negative regulators (Mst1, Lats2, Mob1b) of the Hippo Pathway, which leads to the induction of embryonic cardiomyocyte proliferation by activating the insulin-like growth factor and Wnt signaling pathways [55]. Postnatal re-expression of miR-302-367 reactivates cell cycling in cardiomyocytes, resulting in reduced scar formation after myocardial infarction [89]. However, long-term expression of the cluster was shown to induce cardiomyocyte dedifferentation and dysfunction, suggesting that persistent reactivation of the cell cycle in postnatal cardiomyocyte is not desirable [89]. This limitation can be overcome by transient systemic application of miR-302-367 mimics, leading to increased cardiomyocyte proliferation, decreased fibrosis, and improved function after injury without maladaptive effects.

1.2.3.4 MiR-199a-3p and miR-590-3p

MiR-199a-3p and miR-590-3p have been identified by a high-content, fluorescence-microscopy-based, high-throughput screening for their pro-proliferative effect in neonatal rodent cardiomyocytes [82]. Their capacity of boosting cardiomyocyte

proliferation has further been confirmed in neonatal rodent hearts after intracardiac injection. Finally, Eulalio et al. in our laboratory has demonstrated that microRNA precursors for these two miRNAs, delivered through AAV vectors, in a model of myocardial infarction in adult mice were able to preserve cardiac function up to two months after infarction by significantly increasing cardiomyocyte proliferation in the infarct border zone [82].

1.3 miR-199a

There are two loci that encode the precursor of miR-199a-5p and -3p in the human genome; one is on chromosome 1 (miR-199a-2, miRBase Accession MI0000281) and the other on chromosome 19 (miR-199a-1, miRBase Accession MI0000242). The precursor of miR-199a used in this study to induce miR-199a-5p and -3p expression is miR-199a-1. MiR-199a-1 on chromosome 19 (Chr19) is embedded in the anti-sense strand of intron 15 of the dynamin 2 (DNM2) gene, whereas miR-199a-2 on chromosome 1 (Chr1) is embedded in the anti-sense strand of intron 14 of the dynamin 3 (DNM3) gene [90]. There is no evidence of functional correlation between the expression of the dynamin genes and the miR-199a precursors: this may be due to the fact that the expression of both miRNA precursors is controlled by their own promoters (UCSC genome browser).

Dnm3 antisense transcript contained in its intron, *Dnm3os,* is conserved in vertebrate lineages [91] and mature microRNAs miR-199a-3p and miR-199a-5p are conserved in mouse, rat, human and pig (miRBase 21).

1.3.1 Regulation of miR-199a expression

Currently, two main mechanisms have been described for the control of miR-199a expression. One is based on the regulation by transcription factors TWIST1 and EGR1 on Chr1 while the other one on the methylation status of miR-199a promoters on both Chr1 and Chr19 [90]. There is not a distinctly defined promoter region for miR-199a-1, therefore the region several hundreds base upstream miR-199a-1 is considered as its promoter region. McroRNA-199a-1 has a predicted CpG island upstream the mature

sequence between 130 and 540 bp [92], while miR-199a-2 has a moderately CpG-poor region in the promoter, which is 1349 bp long and starts 81 bp upstream the 5' end of the miRNA hairpin region [93]. Several in vitro studies have shown that promoter regions on Chr1 and Chr19 are hypermethylated in cancer cells, while they displaye hypomethylated status in normal fibroblasts. Accordingly, miR-199a expression is higher in normal fibroblasts than in cancer cells [92].

TWIST binds an E-box region on *Dnm3os* promoter and drives the expression of the DNM3OS transcript, which gives rise to miR-199a-2 and miR-214 [94]. *Dnm3os* regulation by TWIST depends on tissue and stage of development [95] albeit it does not seem to be the only factor regulating *Dnm3os*.

In certain types of cancer, in fact, EGR1 was demonstrated to occupy the miR-199a-2/miR-214 gene promoter [96]. Remarkably, a direct target of miR-199a-3p and miR-199-5p is BRM, which is part of the catalytic subunit of the chromatin remodeling complex SWI/SNF. BRM is, in turn, a negative regulator of EGR1; therefore, miR-199a together with BRM create, as a result, a double negative feedback loop through EGR1. There are types of cancer expressing high levels of BRM (e.g., non-small cell lung cancer, breast and cervical cancer, etc.) or cancers expressing low levels of BRM (adrenocortical cancer, gastric cancer, cervical cancer, etc). This findings may explain the variable, low or high, expression of miR-199a-5p and -3 in different types of malignancies [90].

In addition, in the context of mice hearts, miR-199a-5p is post-transcriptionally downregulated by AKT [97] during hypoxia and upregulated during cardiac hypertrophy via β-adrenergic receptor stimulation [98].

1.3.2 MiR-199a in tumorigenesis

Many efforts have been made to unravel the role and the expression pattern of miR-199a in different cancer types. This microRNA can act as tumor suppressor, thus being downregulated, or it can act as an oncogene and be upregulated in specific types of tumors. These main differences might be due to the above described complex transcriptional control mechanisms, and its involvement in different cellular phenotypes can be ascribed to the diverse nature of its downstream targets.

MicroRNA-199a downregulation has been mainly studied in liver cancer, where it inhibits cell proliferation by targeting HIF1α [99]. It has also been found to directly downregulate a pro-invasion factor, DDR1, in human hepatocellular carcinoma cell line (HCC) [100]. Aside from liver cancer, miR-199a also showed reduced expression in other malignancies, such as ovarian cancer where its downregulation correlates with poor prognosis [101]. Other examples of miR-199a downregulation can be find in renal [102], breast [103] and bladder cancer [104].

There are cases of tumors overexpressing miR-199a, as was for the group of cancers characterized by down-regulation of this microRNA. For example, in pediatric hepatoblastoma, as opposed to adult hepatocellular carcinoma, miR-199a is up-regulated [105]. In gastric cancer its up-regulation positively regulates cell proliferation, migration and invasion by targeting MAP3K11 [106].

1.3.3 Antiviral effects of miR-199a

In vitro studies have shown that miR-199a can inhibit HCV genome replication, suggesting its potential antiviral effect [107], which was further confirmed in the case of the hepatitis B virus [108]. Besides interacting with viral elements, miR-199a exerts its antiviral effects by down-regulating several transcripts along the pathways required and/or activated by the invading virus, including ERK/MAPK signaling, prostaglandin synthesis, oxidative stress signaling and PI3K/AKT signaling [109].

1.3.4 MicroRNA-199a in embryonic development

The antisense *Dnm3os* transcript contained in the *Dnm3* intron, which gives rise to miR-199a-2 and miR-214, is mostly expressed during embryonic development, while the *Dnm3* transcript is expressed at low levels in embryonic life and at high levels in adult, especially in testis and brain [95]. This led to the assumption that miR-199a is fundamental for embryonic development. In fact, *Dnm3os* knock-out pups die one month after birth, displaying several skeletal abnormalities including craniofacial hypoplasia, defects in dorsal neural arches and spinous processes of the vertebrae and osteopenia. Thus, the *Dnm3os*-encoding gene appears indispensable for normal skeletal development and body growth in mammals [110].

1.3.5 The role of miR-199a in the heart

The function of miR-199a in the heart has been investigated by several studies in reference to its effects on proliferation, metabolism, hypertrophy, autophagy and cell death protection. Cardiac microRNA profiling analysis has shown that expression of both miR-199a and miR-214 is increased in various models of heart failure [75, 76] in mice and humans. The transcription of *Dnm3os* Dynamin3 antisense transcript is stimulated by pressure overload and hypoxia induced by transient aortic constriction (TAC) in mice [111]. Hypoxic condition in particular, leads to HIF1 α activation, which, in turn, activates Twist1 [111]. As described above, TWIST1 recognizes an E-box region in the *Dnm3os* promoter and stimulates its transcription. Once transcribed and processed, both microRNAs target PPAR γ , the down-regulation of which induces a shift from fatty acid metabolism to glycolysis, typical of failing hearts [111].

MicroRNA-199a-5p overexpression was further associated with hypertrophy and cell size regulation in both rats [112] and mice [113]. If inhibited in rat cardiomyocytes, it brings to cell size reduction, even after induction of hypertrophy by phenylephrine (PE), and increased alpha myosin heavy chain expression [112]. Moreover, its overexpression in vitro suppresses the anti-hypertrophic effects of Qiliqiangxin, a traditional Chinese medicine, which has long been used to treat chronic heart failure in patients [113].

MicroRNA-199a was also linked to autophagy by its ability to target GSK3 β , which can, in turn, inhibit mTOR [114]. Its overexpression leads to a reduction in autophagy and, consequently, to hypertrophy [114], which can be reverted in vivo by injecting rapamycin, an autophagy activator.

Furthermore, miR-199a-5p can also exert negative paracrine effects on cardiac endothelial cells [115]. In STAT3 KO mice, which develop spontaneously heart failure, miR-199a-2 is up-regulated and targets ubiquitin-conjugating enzymes Ube2gi and Ube2i. This negative regulation causes disruption of the sarcomere structure driven by decreased levels of myosin heavy chain alpha and beta, troponin and tropomyosin, and promotes synthesis of asymmetric di-methylarginine [115], which inhibits eNOS. Reduced NO synthesis, in turn, causes endothelial dysfunction in mice lacking STAT3 [115].

Finally, miR-199a levels greatly decrease in cardiomyocytes cultured under low oxygen tension [116]. This negative regulation seems to be required to stabilize p53 and to activate, through HIF1 α , a miR-199a-5p direct target, the hypoxia pro-apoptotic genes.

[116]. However, if miR-199a-5p is restored, even under hypoxic conditions, this is sufficient to reduce apoptosis [98] [116].

Micro-199a-3p was also reported to exert positive effects in protecting cardiomyocytes from apoptosis [117]. Park and coworkers demonstrated that, in cultured primary cardiomyocytes, this miRNA down-regulates Ddit4, a pro-apoptotic protein, after ischemia/reperfusion injury. In addition, the upregulation of miR-199a-3p and miR-214 in cells treated with carvedilol, a β-adrenergic antagonist, promotes an anti-apoptotic effect through Akt activation [117].

1.4 Heart regeneration in pig models: bridge from bench to bedside

As stated by the Helsinki declaration (2013) [118], every new developing treatment aimed to reach human health must be supported by painstaking laboratory and animal experimentation. In vivo experiments in small animals such as rodents, provide the therapeutic potential for regenerative treatments. However, before applying any therapy to humans, large animal studies are a fundamental prerequisite to evaluate efficacy and safety profiles in animal models that are highly relevant to humans with respect to cardiac anatomy and function. Swine in particular, is the most recommended species for the similarities to humans in terms of cardiac and coronary anatomy and physiology. Like in humans, the pig left coronary artery is usually longer and larger in diameter than the right coronary artery. Forty-nine percent of the left ventricle is supplied by the left anterior descending coronary artery (LAD), which also feeds 58% of the intraventricular septum [119]. Another reason for using swine models is that the size of these animals allows morphological and functional assessments based on clinical standard diagnostic tools, such as echocardiography, magnetic resonance imaging (MRI), computed tomography, positron emission tomography (PET) and single-photon emission computed tomography [120].

*1.*4.1 Diagnostic imaging of myocardial infarction by cardiac magnetic resonance

After ischemia-reperfusion, myocardial damage and mechanical dysfunction are usually evaluated by echocardiography or cardiac magnetic resonance.

The former is frequently used in clinical settings, but displays several limitations. It has notoriously imperfect acoustic windows, scant visualization of the endocardial border which, together with other geometric assumptions resulting from the two-dimensional approach affect its accuracy and reproducibility [121].

Cardiac magnetic resonance (cMRI) is instead the golden standard technique to measure, with great accuracy, ejection fraction, infarct size, myocardial thickness, perfusion and viability and regional wall motion abnormalities. Left ventricle mass and volume can be measured with a standard error of 5%, making it the most reproducible and precise approach to measure cardiac function [122].

1.4.2 Tagging cMRI – quantifing regional wall motion

Cardiac magnetic resonance allows regional myocardial deformation measurement without the need to implant physical markers. In 1988, Zerhouni et al. [123] established a new noninvasive cMRI method, known as myocardial tissue tagging, to track regional myocardial motion. Cardiac regions are magnetically tattooed by a grid-like geometrical pattern (tags), which appear as dark lines in the acquired images. Tags in two orthogonal direction, combined, form a grid of tissue markers which allow motion tracking throughout the cardiac cycle [124]. cMRI tagging allows quantitative measurements of intramyocardial motion such as strain. Strain analysis permits a direct assessment of the degree of regional myocardial deformation and its timing during the cardiac cycle; it is expressed as the percentage of shortening or lengthening of a small element of myocardium in relation to its original length [124]. Strain is calculated as:

- Radial strain. The radial strain of cardiac wall is measured, along a radial direction, toward the center of the ventricle. Positive values mean that during systole myocardium is thickening, while negative values indicate dyskinesia or local wall thinning during systole.
- Circumferential strain. Circumferential strain quantifies the intramural circumferential shortening. Negative values correspond to myocardial contraction and therefore circumferential shortening, while positive values indicate systolic bulging.
- Longitudinal strain. Longitudinal strain quantifies myocardial shortening from base to apex (negative value)[124].

1.4.3 Late gadolinium enhancement for the quantification of myocardial infarction size

Late gadolinium enhancement is the gold standard technique for precise quantification of myocardial scar tissue extension. In healthy myocardium, extracellular contrast agents are rapidly washed out in a time window of around 10-15 minutes, while non-viable myocardium needs a longer time to eliminate them. After administration, gadolinium is rapidly removed from functional myocardium, but it is still present in the infarcted myocardium, thus localizes as a highlighted area by T1-weighted inversion recovery sequences [125]. Based on this principle, late gadolinium enhancement cMRI is able to detect small masses of necrotic or fibrotic myocardium.

1.4.4 Strategies aimed to induce cardiomyocyte proliferation in pigs

As described above, mammalian cardiomyocytes lose their proliferating ability soon after birth [5] impeding adult heart regeneration after myocardial infarction. One strategy to overcome negative remodeling and heart failure is to replace cardiomyocyte loss by inducing pre-existing myocytes to re-enter cell cycle and replenish dead cardiomyocytes, thus competing with the process of scar formation. Some of the therapeutic strategies having this specific aim have reached experimentation in large animals.

1.4.4.1 Gene therapy to stimulate heart regeneration in pigs

A possible approach is to force the re-expression of key cell cycle regulatory genes which are normally silenced soon after birth in the mammalian heart [126]. One of the best examples was given by Shapiro et al. [127]. These authors demonstrated how adenovirus carrying the Ccna2 gene (encoding for cyclin A2) injection one week after catheter-induced myocardial infarction was sufficient to increase ejection fraction from 35% before treatment to 42% six weeks after transgene delivery, as assessed by cMRI, echocardiography and LV angiography. The functional improvements reported in this study were correlated to a 3.5-fold increase in cardiomyocyte proliferation, as assessed by Ki-67 and phospho-histone3 immunofluorescence. Accordingly, fibrosis was higher in non treated animal infarct zones, while Ccna2-treated animal displayed a higher number of healthy cardiomyocytes and a reduced infarct size which was not

accompanied by an increased cardiomyocyte hypertrophy [127]. In any experimental approach, such the one presented by Shapiro et al., entailing the use of cell cycle regulators, precautions must be in place to prevent unwanted effects in extracardiac tissues, due to the potential for oncogenic transformation. These safety concerns would necessitate tissue-specific activation of cyclin A2, or the adoption of molecular strategies for its transient expression.

Quite surprisingly, gene therapy with two main angiogenic factors was also reported to increase cardiomyocyte proliferation in pigs [128]. In a study by Tao et al., the delivery of VEGF and Ang1 cDNAs through adeno-associated viral vectors (AAVs) immediately after LAD ligation was sufficient to improve cardiac function and myocardial perfusion assessed by single-photon emission computed tomography 2 and 8 weeks after infarction. Treated animals displayed a massive induction of angiogenesis, reduction of cell apoptosis and increased cardiomyocte proliferation through activation of Akt kinase and up-regulation of cyclin D2/cdk4 and cyclin A/cdk2 [128]. However, the contribution of the pro-proliferative effect was quite modest, and heart function amelioration was massively attributed to protection from cell death [128].

1.4.4.2 Recombinant protein delivery to stimulate heart regeneration in pigs

Aiming at boosting cardiomyocyte proliferation, Wei et al. identified an epicardial factor, follistatin-like-1 (Fslt1) [47], the expression of which is lost after damage in mammals, as a potent cardiogenic protein in mouse and pig models. Patches of recombinant Flst1 protein applied to pig epicardium one week after MI induction, stimulated recovery of cardiac function - ejection fraction, as measured by cMRI, increased from 30% to 40% two weeks post patch implantation by increasing cardiomyocyte proliferation and stimulating arteriogenesis [47].

Finally, the results of a study in which IGF-1 and HGF were delivered alone or in combination with a self-healing hydrogel one month after infarction, also appear worth mentioning. In this case, echocardiography measurements demonstrated significant improvement in ejection fraction and LV end-systolic volumes 4 weeks after delivery [129]. Functional parameter improvements and reduction in scar size were correlated with an almost 4-fold increase in cardiomyocyte proliferation and a 2-fold increase in the number of the endogenous c-Kit positive, CD45 negative cardiac stem/progenitor cells in the infarcted area [129].

1.4.4.3 microRNA-based strategies to restore cardiac function in pigs

Up to date, there are no reports about any microRNA exerting a pro-proliferative effect on cardiomyocytes in a swine model of acute myocardial infarction .

However, approaches modulating microRNAs have already been tested in an MI model in pigs to protect myocardium from ischemia-reperfusion injury or to promote angiogenesis.

Strategies aimed at the inhibition of miR-92 were used to protect from ischemia/reperfusion injury [130] and to induce new vessel formation [131]. An LNA antisense directed against miR-92a, applied regionally after MI induction by balloon occlusion, was able to reduce scar size one week after infarction from 55% to 35% (control versus treated animals) [130] and to significantly increase ejection fraction, evaluated by hemodynamic measurements. The mechanism by which the inhibition of miR-92 protects from ischemia/reperfusion injury is explained by halved cardiomyocyte death, increase in the number of capillaries and by significant reduction of ischemia/reperfusion-induced inflammation [130]. The delivery of miR-92a was additionally achieved exploiting poly-lactide-co-glycolide (PLGA) microspheres, which prolonged miRNA inhibition for at least 10 days [131]. The persistent miR-92a inhibition reduced regional-wall motion dysfunction one month after injury [131].

1.5. Adeno-associated viral vectors (AAVs)

Adeno-Associated Viral Vectors are non-enveloped, single stranded (ss) DNA viruses with a diameter of 18-25 nm which belong to the family of Parvoviridae and the genus Dependovirus. These viruses are not able to replicate autonomously; in fact, wild-type AAV infection depends on the super-infection with another virus [132]. The first factor identified as a successful helper in the generation of AAV particles was Adenovirus, hence the name [132]. Around one hundred of different wild-type AAV serotypes have been identified to date, each one displaying a specific tropism for different tissues, not necessarily related to the ability to bind specific cell surface primary receptors, since most serotypes make use of ubiquitous, cell surface proteins for docking to the cell surface and internalization through endocytosis. However, despite the high sero-

prevalence of AAV in the human population, the virus has never been linked to any human pathology.

1.5.1 Genome organization

AAV has a linear DNA genome of about 4.7 kb and contains two open reading frames, corresponding to the genes *rep* and *cap*, flanked by 145 nt-long inverted terminal repeats (ITRs), in which the first 125 nucleotides constitute a palindrome, which folds upon itself forming a T-shaped hairpin structure, identical at the two viral ends [133].The ITRs, due to their structure, provide a free 3' hydroxyl group that is essential for the initiation of viral DNA replication by a cellular DNA polymerase in a primase-independent manner [134]. Due to their importance in AAV biology, the ITRs are the only sequences maintained during the generation of recombinant AAV vectors.
The *rep* region codes for replication-related proteins, while the *cap* region codes for the three structural proteins, VP1, VP2, and VP3, which together form the viral capsid [135] Rep and Cap transcripts are produced from their respective promoters p5, p19 and p40. The four Rep protein isoforms, namely Rep78, 68, 52 and 40, have helicase and ATPase activity but only Rep78 and Rep68 have strand- and site-specific endonuclease and site-specific DNA binding activities. Rep78 and Rep68 in particular, bind specific sites within the ITRs, and are required for viral DNA replication and site-specific integration. On the contrary, Rep52 and Rep40 are involved in the generation of single-stranded viral genomes for packaging into AAV capsids [135]. The structural proteins VP1, VP2 and VP3 (transcribed from the *cap* gene from the p40 promoter) assemble together in the ratio of 1:1:18, generating a capsid shell with icosahedral symmetry and a diameter of 18-25 nm [136]. Each viral particle contains the viral genome in the form of a single stranded DNA molecule having either positive or negative polarity [136]. In addition, the VP1 protein also contains a phospholipase A2 (PLA2) motif, fundamental for AAV escape from the endosomes [137].

1.5.2 AAV infection

1.5.2.1 Docking onto the cell membrane

The first step in AAV infection consists in the binding of the virus to specific receptors,

which mediates its entry inside the cell. Heparan sulfate proteoglycan (HSPG) is the primary receptor for AAV2, AAV3 [138]; sialic acid for AAV1, AAV4, AAV5, AAV6; the 37/67 kDa laminin receptor for AAV8; and N-linked glycans with terminal galactosyl residues for AAV9. Additionally, the virus takes advantage of the binding to cellular co-receptors such as the growth factor receptors FGF, PDGF and HGF or the integrins a_Vb_5 and a_5b_1, important for the efficiency of infection and for determining cellular selectivity of the different serotypes. Finally, a recent study has described a transmembrane protein, AAVR, as a general key receptor for AAV, fundamental for binding and internalization [139].

1.5.2.2 Endocytosis

After receptor binding, internalization is the next step in the AAV viral entry pathway trough clathrin-coated vesicles. For a successful AAV infection to occur, the viral particles need to escape from these endocytic vesicles which is mainly mediated by the activity of the viral phospholipase A2 [137] motif (HDXXY), which is present at the N-terminal of VP1 [137]. The lowering of pH inside these compartments during their maturation from early to late endosomes, determine a conformational change in VP1, which mediates the exposure of the N-terminal ends of the protein, containing the vPLA2 domain as well as nuclear localization signals (NLS) [137] [140]. The VP1 PLA2 domain induces pore formation in the endocytic vesicles, thus allowing the virus to escape while the exposed NLS mediates translocation of the virion into the nucleus [140] [141].

1.5.2.3 Nuclear entry

The mechanisms underlying nuclear translocation of the virus across the nuclear membrane are still incompletely understood. A recent report has shown that nuclear entry of rAAV2 is mainly dependent on the canonical nuclear import pathway, involving an active importin-β mechanism [140]. The timing and dynamics of virion uncoating are also still debated. Sessiseberger et al. reported the presence of GFP-labeled AAV viral capsids into the nucleus, thus suggesting that viral uncoating occurs after nuclear entry [142] whilst, Lux et al. originally showed that viral uncoating occurs before and during nuclear entry [143]. A more recent study, however, has demonstrated that AAV2

virions enter the nucleus and accumulate in the nucleolus, thus confirming that viral uncoating occurs inside the nucleus [144].

1.5.2.4 Genome processing and new viral particles synthesis

After virion uncoating, the free AAV ssDNA genomes must be converted into dsDNA to be transcribed. In a few hours, every cell produces $5x10^5$-$1x10^6$ viral particles; the infected cells eventually are lysed and the virions released outside them. The molecular determinants governing cell permissivity to productive AAV replication are still largely unclear. A number of treatments increase the efficiency this process, including DNA-damaging agents (ultraviolet, gamma-irradiation, X-radiation, alkylating agents, radiomimetic drugs, etc.), agents that inhibit DNA synthesis (hydroxyurea), thereby suggesting that DNA damage repair (DDR) mechanisms may be involved in transduction [145]. Indeed, the AAV genome, similar to damaged cellular DNA, is single-stranded and bears imperfectly paired DNA sequences at the level of its terminal hairpins [146] [147]. These proteins block replication of the genome by impeding its conversion to a double-stranded form. Once a cell is treated with chemical or physical agents, its DDR proteins are diverted to other sites of DNA damage, thus permitting the AAV genome to complete its replication.

1.5.3 Recombinant AAV

The characteristics of AAV life cycle, including its defectiveness and ability to persist in infected cells as a latent viral genome, early suggested that this virus could be an excellent tool for in vivo gene transfer [148]. Between the ITRs, an expression cassette is cloned containing the therapeutic gene and its regulatory elements. Any kind of promoter is suitable for the expression of the insert, whose size is restricted to a maximum of 4 - 4.5 kb. The ITR sequences of the parental virus are the only required cis elements for viral genome replication and its packaging into viral particles. The *rep* gene is removed from the vector DNA genome, therefore allowing the persistence of AAV inside non-dividing cells mainly as extrachromosomal, concatameric DNA. To date, rAAV preparations are mostly based on a helper-free method, which entails the transfection of HEK293 cells with three plasmids: 1) an AAV2-ITR-containing plasmid carrying the gene of interest; 2) a plasmid carrying the Rep-Cap of the desired serotype;

a plasmid expressing the helper genes (E4, VA, E2A) from Adenovirus.

Recombinant AAV vectors of different serotypes have been shown to be very efficient in transducing post-mitotic tissues such as brain (AAV9), heart (AAV9 [149], rAAV6 [150]), retina (photoreceptors; rAAV5, rAAV8 [151]), skeletal muscle (myofibers; rAAV1, rAAV6 and rAAV7 [152] [153]), liver (rAAV8 and rAAV9 [154]) and pancreas (endocrine/exocrine pancreas; rAAV8, rAAV6 [155]).

1.6. Chemical modifications of miRNA-based therapeutics

In just two decades, since their discovery, the field of miRNA biology has expanded considerably. Accumulating insights into their roles in development and disease have turned miRNAs into attractive tools and targets for novel therapeutic approaches.

There are two ways to approach a miRNA-based therapeutic intervention: i) using strategies to upregulate a specific miRNA through miRNA mimics or ii) exploiting inhibitors of miRNAs (antimiRs) to obtain the reduction in the levels of an endogenous miRNA.

MiRNA mimics are synthetic, double-stranded small RNA molecules the sequence of which corresponds to the endogenous miRNA and consequently exerts its function. On the contrary, antimiRs are single stranded oligonucleotides designed to block and inhibit a target miRNA [156].

The main challenge for RNA-based therapeutic strategies (for both single- or double-stranded oligonucleotides) is the risk of oligonucleotide degradation by RNases in serum or in the endocytic compartment of cells, together with the possible recognition by the immune system [157]. Therefore, in the past years, many efforts have been made in in achieving increased oligonucleotide half-life *in vivo,* playing with different chemical modifications or, on the other hand, in developing delivery vehicles to encapsulate RNA for protection and allow endosomal escape.

While over the past years most of the studies have focused on miRNA inhibition, a few successful methods have also been devised to deliver miRNA mimics. As a matter of fact, miRNA mimicry approaches mainly use the same chemical modification of antimiRs to increase oligonucleotide half-life. To therapeutically transfect a miRNA mimic, it is convenient to deliver synthetic RNA duplexes that harbour chemical modifications to improve stability and cellular uptake [158]. In miRNA mimics, the strand identical to the miRNA of interest is the guide (“antisense” as referred to the target mRNAs, strand),

whereas the opposite ("sense" or "passenger") is less stable and can be associated to a molecule, such as cholesterol, to enhance cellular uptake. Furthermore, the passenger strand might contain chemical modifications to prevent its loading into the RISC or it can even be unmodified to ensure rapid degradation [159]. One example was given by the work of Montgomery and colleagues, who described the development of a functional miR-29 mimic to target pulmonary fibrosis [160]. The sense, passenger strand (identical to the target mRNAs) contained a 2'-OMe modification to prevent loading into RISC, while the antisense, active strand (complementary to the target miRNA) contained a uracil-uracil overhang at the 3' end to increase stability, and was phosphorylated at 5' end [160].

The modification that antisense strand can undergo are limited because of the need, for the RNA molecule, to be recognized by RISC. The 2'-fluoro (2'-F) modification renders the guide strand more stable because of its function in protecting against exonucleases, without interfering with RISC loading [161]. The most commonly used sugar modifications are 2'-*O*-methyl ribose-modified RNA (2'-OMe), 2'-*O*-methoxyethyl (2'-MOE) RNA and locked nucleic acid (LNA) which improve the resistance to nuclease and increase the melting temperature, leading to a thermodynamically strong duplex formation with complementary RNA [162]. Among the cited sugar modifications, LNAs exhibits the highest affinity toward complementary RNA with an increased $T_{melting}$ of +2-8°C per introduced LNA modification [163], while 2'-MOE modifications have superior binding affinity, efficacy and nuclease resistance compared to 2'-OMe [164].

In addition, increased nuclease resistance can be achieved by substituting the phosphodiester backbone linkages with phosphorothioate linkages [165]. Apart from nuclease resistance, phosphorothioate modifications also enhance binding to plasma proteins, leading to reduced clearance by glomerular filtration and urinary secretion. Therefore, phosphorothioate-modified oligonucleotides display noticeably improved pharmacokinetic properties, facilitating their delivery into many peripheral tissues *in vivo* [166].

2. MATERIAL AND METHODS

All the laboratory reagents, used in this study are listed in Table1 and were purchased from standard suppliers. All the solutions were prepared with MilliQ (Millipore) water and, if required, solutions were sterile filtered (0.22 μ m pores) before use.

2.1. Cell biology protocols

2.1.1 Isolation and culture of primary neonatal rat/mouse ventricular cardiomyocytes

Wistar rats and CD1 mice were purchased from Charles River Laboratories Italia Srl. Animal care and treatments were conducted in conformity with institutional guidelines in compliance with national and international laws and policies (EEC Council Directive 86/609, OJL 358, December 12, 1987).

After neonatal rats/mice sacrifice by cervical dislocation and organ harvesting, ventricles were separated from the atria, cut into smaller pieces and digested at room temperature using 1.75mg/ml trypsin (BDmDifco) and 10 μ g/ml DNaseI (SIGMA) in CBFHH buffer (calcium and bicarbonate-free Hanks with HEPES). The collected supernatant was centrifuged to separate the cells, which were subsequently re-suspended in DMEM, high glucose supplemented with vitamin B12 (Sigma), 5% of fetal bovine serum (FBS, Life Technologies) and with 100U/ml of penicillin and 100 μ g/ml of streptomycin (Pen-Strep, Sigma). The collected cells were passed through a cell strainer (40 μ m, BD Falcon) and seeded on uncoated 100 mm dishes (DB Falcon) for 2 hours at 37°C in 5% CO_2. After this passage, cardiomyocytes were mainly present in the supernatant. Cardiomyocytes were counted and plated at the desired density in DMEM, high glucose supplemented with vitamin B12 (Sigma), 5% of fetal bovine serum (FBS, Life Technologies) and with 100 U/ml of penicillin and 100 μ g/ml of streptomycin (Pen-Strep, Sigma) in primary or collagen coated plates.

2.1.2 Isolation and culture of human fetal ventricular CMs cardiomyocytes

Upon Burlo Garofalo Children Hospital Ethical Commettee approval, 17-22 week

gestation human abortive foetus hearts were excised at Burlo Garofalo Hospital, Trieste, and immediately transported in Krebs-Ringer solution (10 mM Hepes; 129 mM NaCl; 4.7 mM KCl; 1.2 mM KH_2PO_4; 1.2 mM $MgSO_4$ x $2H_2O$; 5 mM $NaHCO_3$; 5,5 mM glucose; 2 mg/ml BSA; 20 mM taurine; 2 mM carnitine; 5 mM creatine; 30 mM butanedione monoxime buffered at pH 7.4) at 4°C to the International Center for Genetic Engineering and Biotechbology (ICGEB), Trieste. The myocardium was cut into small pieces after careful removal of pericardial traces. The digestion solution was prepared immediately before the experiment with 1.75 mg/ml trypsin (BDmDifco) and 10 μg/ml DNaseI (SIGMA) in CBFHH buffer (calcium and bicarbonate-free Hanks with HEPES) and added to heart fragments, which underwent a total of 8 digestions step at 37°C. The supernatants of each step were collected and centrifuged to separate the cells, which were subsequently re-suspended in DMEM high glucose supplemented with vitamin B12 (Sigma), 5% fetal bovine serum (FBS, Life Technologies) and 100 U/ml of penicillin plus 100 μg/ml of streptomycin (Pen-Strep, Sigma). The collected cells were passed through a cell strainer (40 μm, BD Falcon) to eliminate undigested fragments of tissue. Human fetal cardiomyocytes did not require any pre-plating, therefore we immediatly plated them, after counting, at the desired density in DMEM high glucose supplemented with vitamin B12 (Sigma), 5% of fetal bovine serum (FBS, Life Technologies) and with 100 U/ml of penicillin and 100 μg/ml of streptomycin (Pen-Strep, Sigma) on primary or collagen coated plates.

2.1.3 Transfection of neonatal rat and human fetal CMs with microRNA mimics

The microRNA mimics were transfected into neonatal rat and human fetal CMs using a standard transfection protocol, at a final microRNA concentration of 25 nM. The following procedure and volumes refer to a well of a 96 multiwell plate.

The transfection reagent (Lipofectamine RNAiMAX, LifeTechnologies) was diluted in OPTI-MEM (Life Technologies) and incubated for 5 minutes. The transfection mixture was added to 1.5 ml Eppendorf Tubes containing each microRNA mimic (500 nM concentrated) and incubated for 30 minutes. The mixture was than transferred into each well, where $1.0*10^4$ cells had been seeded 24 hours before (final volume 150 μl/well) in DMEM high glucose supplemented with vitamin B12 (Sigma), 5% of fetal bovine serum (FBS, Life Technologies) and without antibiotics.

MicroRNA mimic transfection protocol for 96 well plates format, volumes per well:

– 7.5 μl of microRNA mimic at the concentration of 500nM

– 24.8 μl of OPTI-MEM

– 0.2 μl of RNAiMAX

Protocol:

1. Incubate RNAiMAX and Opti-MEM medium (Gibco) for 5 minutes at RT

2. Dispense 25 μl/well of transfection mix into 1.5ml eppendorf tube containing 7.5 μl /well of microRNA (500nM);

3. Incubate for 30 minutes at RT

4. Dispense 32.5 μl of mix/well on top of previously seeded rat CMs 1.0 *10^4 cells/well (150 μl final volume) in medium described above, without antibiotics

5. 24 hours after transfection change the medium with fresh DMEM, high glucose supplemented with vitamin B12 (Sigma), 5% of fetal bovine serum (FBS, Life Technologies) and with 100 U/ml of penicillin and 100 μg/ml of streptomycin (Pen-Strep, Sigma)

6. Incubate for 72 hours

7. Wash the cells 2 times in PBS (100 μl/well)

8. Fix the cells in 4% PFA (50 μl/well)

2.1.4 Transfection of mouse cardiomyocytes with microRNA mimics

MicroRNA mimic transfection of mouse CMs requires the same protocol for rat CMs described above. However, the final concentration of microRNA mimics was optimized at 50 nM for mouse CMs instead of 25 nM for rat CMs.

2.1.5 Cardiomyocyte transduction

The day after plating, cell colture medium was replaced with fresh complete one (DMEM, high glucose supplemented with vitamin B12, 5% of fetal bovine serum and with 100 U/ml of penicillin and 100 μg/ml of streptomycin) and cells has been transduced with AAV6 considering $1*10^4$ viral particles per cell, following this formula:

$$\frac{(number\ of\ seeded\ cells) * (1\text{x}10^4\ viral\ particles\ per\ cell)}{(viral\ titer)}$$

2.2. Molecular biology protocols

2.2.1.Total DNA isolation from organs

After sacrifice, the different organs were removed by gross dissection from treated pigs, washed in PBS and snap frozen in liquid nitrogen. DNA was isolated using DNeasy Blood & Tissue Kit following manufacturer's instruction. This kit provides a fast and easy silica-based DNA purification method on convenient to use spin-columns. Samples can be directly lysed with proteinase K, eliminating the need for mechanical disruption and reducing hands-on time.

2.2.2.Total RNA isolation from organs and cultured CMs

Total RNA was extracted from organ or organ fragments prepared and stored at -80°C as described in the previous paragraph. For RNA extraction, 1 ml of TRIzol reagent (Invitrogen, Carlsbad, CA, USA) was added to each samples (maximum weight 50 mg) and the tissue was efficiently disrupted using the MagNA Lyser Beads in the dedicated Instrument (Roche).

Total RNA was also exttracted from cultured rat or mouse CMs. In this case, cells were washed in PBS and directly lysed using TRIzol reagent (1ml for ≅250 thousands CMs) (Invitrogen, Carlsbad, CA, USA).

After either tissue homogenization or cell lysis, TRIzol was recovered and RNA extracted using the miRneasy mini kit (Qiagen), according to the manufacturer's instructions.

2.2.3 Quantification of nucleic acids by real-time PCR

Total DNA was used as a template for realtime PCR to detect the presence of the sequence of the AAV vector in fragments of heart tissue as well as of other different organs. To this end, we used primers together with a TaqMan® probe (Applied Biosystems, Foster City, CA, USA) to specifically detect the CMV promoter contained in

our vectors. The exact number of molecules of the vector per microgram of total DNA was quantified by the simultaneous amplification of a standard curve of known quantity of a plasmid containing the target sequence. In parallel, vector genomes were also quantified using the housekeeping 18S rRNA gene as a normalizer (Thermofisher Scientific).

Total RNA extracted from our sample tissues was quantified at Nanodrop and reverse-transcribed using hexameric random primers (Invitrogen), starting from 1 μg of RNA. The cDNA was used as a template for realtime PCR amplification to detect the expression levels of selected genes. The housekeeping gene GAPDH was used to normalize the results. Quantification of gene expression was performed by quantitative real-time PCR, using the TaqMan® assays (Applied Biosystems) reported in Table 2.

The protocol reported here below has been tested to ensure a reaction efficiency of 2:

• Each reaction was composed in 20 μl:

i) 10 μl 2X PCR Master Mix (Biorad)*;*

ii) 1 μl 20X primers and probe fluorofore FAM

iii) 1 μl cDNA

iv) H_2O to final volume.

• The quantitative RT-PCR entailed these passages:

i) 95°C 5 minutes

ii) 44 cycles:

1. 95°C 10 seconds

2. 60°C 30 seconds

3. Read.

Then the relative quantitation has been normalized to the reference gene using the $2^{-\Delta\Delta CT}$ (Livak) method.

2.2.4 Quantification of miRNA by Mircury LNA universal RT microRNA PCR

MiR-199a-3p and 5p were quantified by real time PCR using miRCURY LNA Universal RT microRNA PCR system (Exilent Syber Green Master Mix, Exiqon) with cDNA previously retro-transcribed by Universal cDNA Synthesis kit (Exiqon) according to the

manufacturer's protocol. The primers used were hsa-miR-199a-3p LNA PCR primer set UniRT and hsa-miR-199a-5p LNA PCR primer set UniRT (Exiqon), which recognize both endogenous pig/mouse/rat/human microRNA and AAV-driven microRNA expression since the sequence in 100% conserved in pig, human, mouse and rat. The housekeeping gene used for normalization was 5S (Exiqon). MicroRNAs were quantified according to the following procedure:

• Each reaction was composed in 10 μl:

i) 5 μl PCR Master mix (Exiqon)

ii) 1 μl PCR primer set (Exiqon)

iii) 4 μl diluted cDNA template

• The quantitative RT-PCR entailed these passages:

i) 95˚C 10 min

ii) 45 cycles:

1) 95˚C 10 s

2) 60˚C 1 min

3) ramp-rate 1.6˚C/s

4) Optical read

• Melting curve analysis

Then the relative quantitation has been normalized to the reference gene: The $2^{-\Delta\Delta}$ CT (Livak) Method has been used.

2.2.5 Immunofluorescence on culture rat and mouse cardiomyocytes (96 multiwell) and ATP level measurement

Cells were fixed with 40 μl of 4% paraformaldehyde (PFA) for 15 min, permeabilized with 40 μl of 0.5% Triton X-100 in phosphate buffered saline (PBS) solution for 10 min, followed by 1 hour blocking in 40 μl of 1% bovine serum albumin (BSA, Roche). Cells were then stained overnight at 4°C in blocking solution (BSA 1% in PBS) plus mouse monoclonal antibody against sarcomeric α-actinin 1:400 (Abcam). Cells were washed with 100 μl PBS and incubated for 2 hours, at room temperature, with the selected secondary antibody labelled with Alexa Fluor-488 (green) or Alexa Fluor-594 (red). Cell

nuclei were further stained with 100 μ l of Hoechst 33342 (Life Technologies) diluted 1:5000 in PBS. Alternatively, for cell viability assay, cells were processed 72 hours after transfection using the ATPlite™ Luminescence Assay (PerkinElmer) according to the manufacturer's protocol. Luminescence was measured by a Wallac EnVisionTM 2104 MultiLabel Reader (PerkinElmer).

2.2.6 EdU Staining in 96 multiwell

When indicated, cells were further processed using the Click-IT EdU 594 Imaging kit to reveal EdU incorporation, according to the manufacturer's instructions. Cell nuclei were further stained with 100 μ l of Hoechst 33342 (Life Technologies) diluted 1:5000 in PBS.

2.2.7 Production and purification of recombinant AAV vectors

Recombinant AAV vectors used in this research project were prepared by the AAV Vector Unit of the International Centre for Genetic Engineering and Biotechnology, in Trieste (http://www.icgeb.org/avu-core-facility.html), as described previously [82] with a few modifications. Shortly, recombinant replication defective AAV particles were generated in HEK293T cell cultures in roller bottles by a cross-packaging approach whereby the vector genome was packaged into capsid serotype-6. Consequently, viral stocks were purified by PEG precipitation from clarified cell lysates and cell culture supernatant followed by two consecutive CsCl2 gradient centrifugations. Full viral particles obtained by the gradient were extensively dialyzed in PBS and stored in aliquots at -80°C until use.

Recombinant AAVs titer was determined by quantifying vector genomes (vg) packaged into viral particles by real-time PCR against a standard curve of a plasmid containing the vector genome. Viral titers obtained for this study were around $1x10^{13}$ vg per milliliter.

2.3. Histology

At the end of the studies, animals were weighted and sacrificed by injection of 10% KCl, to stop the heart at diastole. Heart, lungs, liver, spleen and kidneys were explanted and weighted immediately after sacrifice. The whole organs were rinsed in PBS and fixed in 10% formalin at room temperature. Fixed heart was sectioned as described in Results

sections, Figure 6 F. Organ chuncks were embedded in paraffin and further processed for histology.

2.3.1 Masson's trichrome stain

Masson's trichrome characteristically stains keratin and muscle fibers in red, collagen and bone in blue, cytoplasm in pink, and cell nuclei in dark brown to black. This colour pattern is achieved by the combination of four different stains: Weigert's iron hematoxylin for nuclei, picric acid for erythrocytes, a mixture of acid dyes (acid fuchsin, "ponceau de xylidine") for cytoplasm and aniline blue for connective tissue. Tissue paraffin sections were deparaffinised (65°C for 12 hours and xylene or bioclear for 2 hours at room temperature), rehydrated (5'-100% EtOh; 5'-95% EtOh, 5'-75% EtOh, 5'-50% EtOh, H_2O) and processed using a commercially available kit for Masson's trichrome stain (BioOptica), according to the manufacturer's instructions. Later, slides were dehydrated (5'-50% EtOh; 5'-75% EtOh, 5'-95% EtOh, 5'-100% EtOh, H_20) and mounted in Eukitt mounting medium by Sigma. Fibrosis content was measured on 4x magnification images using ImageJ. Briefly, ImageJ treshold was used to measure blue area (represents fibrosis) which was expressed as percentage of the whole section area.

2.3.2 Periodic acid-Shiff (PAS) stain

The Periodic acid-Shiff (PAS) stain detects glycogen, glycoproteins, glycolipids and mucins in tissues. Periodic acid stain works by oxidising glycols to aldehydes. Aldehydes then react with the Schiff reagent and releases a pararosaniline adduct, which stains the glycol-containing cellular elements in purple. Paraffin slides were deparaffinised (65°C for 12 hours and xylene or bioclear for 2 hours at room temperature), rehydrated (5 min -100% EtOh; 5 min - 95% EtOh, 5'-75% EtOh,5'-50% EtOh, H_2O) and processed using the PAS staining kit (SigmaAldrich) to detect fibre border, according to the manufacturer's instructions. Slides were then dehydrated (5'-50% EtOh; 5'-75% EtOh, 5'-95% EtOh, 5'-100% EtOh, H_2O) and mounted in Eukitt mounting medium by Sigma.

2.3.3. Immunohiystochemistry

Tissue paraffin sections were deparaffinised at 65°C for 12 hours and immersed in xylene or bioclear for 2 hours at room temperature and rehydrated (5 min -100% EtOh; 5 min -95% EtOh, 5 min -75% EtOh, 5 min -50% EtOh, H_2O). Antigen retrival was performed by boiling sections in sodium citratre 0.1 M pH 6.0, 0.05% Tween 20 for 20 minutes and letting them cool down at room temperature for 2 hours. They were subsequently rinsed twice in water and twice in TBS (5 minutes each at room temperature). Permeabilization was performed by soaking slides in TBS-triton 0.1% for 10 minutes, followed by two washes TBS-triton 0.025% of 1 minute each. Sections were further blocked in 10% horse serum, 1% BSA in TBS one hour at room temperature and incubated with primary antibodies 1:100 or 1:150, depending on the antibody, at 4°C overnight in TBS-BSA 1%, anti-GATA4 (Abcam), anti-desmin (Roche), anti-Myogenin (Cell Marque), anti-Endothelin receptor 1 (Abcam), anti-WT1 (Cell Marque), anti-CD34 (Roche), anti-CD45 (Roche) and anti-Ki-67 (Roche). The following day, after three washes in TBS-triton 0.025% at room temperature, tissue endogenous peroxidase was inactivated by incubation for 20 minutes at room temperature with 3% H_2O_2. Hydrogen peroxidase was washed three times with TBS-triton 0.025% and sections incubated with appropriate biotin-conjugate secondary antibody (Abcam) 1:400 in TBS-BSA 1% for 1 hour at room temperature. Following three washings with 0.025% TBS-triton, the signal was amplified incubating the section with Avidin–Biotin-Complex-HRP (ABC KIT Elite-PK-6100, Standard, VECTASTAIN) solution for 30 minutes. After three washes with 0.025% TBS-triton, the immunohistochemical-complex was visualized by exposure to (3, 3 -diaminobenzidine) DAB solutions (ImmPACT DAB, SK-4105, VECTOR) for 3 to 10 minutes. The sections were rinsed with distilled water (dH_2O), stained with 10 drops of hematoxylin for 2 minutes and then washed in water for 2 minutes. Following one quick wash in alchol/acid solution, sections were washed 30 seconds in water, and then soaked 2 minutes in Scott-blue-solution that provided rapid and precise blueing of nuclear chromatin and nuclear membranes. After 30 seconds of washing in water, the sections were quickly dehydrated in ascending concentrations of alcohol (5 min -50% EtOh; 5 min -75% EtOh, 5 min -95% EtOh, 5 min -100% EtOh,) and xylene, before being cover-slipped with Eukitt mounting medium.

2.3.4 Analysis of BrdU incorporation and immunofluorescence

To assess cardiomyocyte proliferation, infarcted pigs received BrdU (Sigma; 10 mg/kg)

intramuscular injections, every day for 10 days. After euthanasia, pig hearts were excised, cut in pieces as described in Results section (Figure 6 F) and briefly washed in PBS, fixed in 10% formalin at room temperature and embedded in paraffin. Samples were cut into 4 μ m tissue sections, de-waxed in xylene for 2 hours and rehydrated with alcohols at decreasing concentration (100, 90, 70, 50%) at room temperature. Antigen retrival was performed by boiling sections in sodium citratre 0.1 M pH 6.0, 0.05% Tween 20 for 20 minutes and letting them cool down at room temperature for 2 hours. Sections were rinsed three times in water and permeabilized 30 minutes in 1% Triton X100 in PBS. DNA denaturation was performed by incubating 10 minutes in 1M HCl on ice and 20 minutes in 2M HCl at 37°C. Cells were incubated with 0.1 M sodium-borate buffer pH 8.4 for 12 minutes at room temperature, then washed three times with PBS and then blocked for 1 h in 10% horse serum PBS. Tissue sections were stained overnight at 4°C in 1:100 anti- α -actinin antibody (Abcam) in 5% horse serum PBS and in 1:100 anti-BrdU (Abcam), washed 3 times 10 min in PBS at room temperature and incubated 1 hour in 1:200 appropriate secondary antibody conjugated to Alexa Fluor-488 and Alexa Fluor-594 (Life Technologies). Sections were further washed three times in PBS and stained with Hoechst 33342 (Life Technologies). Antibodies for histone H3 phosphorylation at serine 10 and and ki-67 were from Millipore and Abcam respectively; assays were performed as described above. To measure cardiomyocyte cross sectional area, lectin Wheat Germ Agglutinin (WGA; Vector Labs) 1:100 was added together with the secondary antibody and incubated as described above.

2.3.5 TUNEL assay

For analysis of TUNEL *in vivo*, heart fragments were fixed overnight in PFA 4%. Cryosections were obtained after 24h incubation in sucrose 20%, rinsed in PBS, permeabilized 15 min in 0.5% Triton X100 PBS, and then blocked for 1 h in 1% BSA in PBS. Tissue sections were stained overnight at 4°C in 1:100 anti- α -actinin monoclonal mouse antibody (Abcam) in 1% BSA in PBS, washed 3 times in PBS at room temperature and incubated 1 h in 1:500 secondary antibody conjugated to Alexa Fluor-488 (Life Technologies). TUNEL assay (Roche) was performed, according to the manufacturer's instructions. Nuclei were further stained with Hoechst 33342 (Life Technologies).

2.4. Surgical instrumentation in pigs

Pig experiments described in the following section were performed at the Istituto di Fisiologia Clinica of the Italian CNR, Pisa, Italy by Doctor Kathia Gabisonia, under the supervision of Professor Fabio Recchia.

Animal care and treatment were conducted in conformity with institutional guidelines in compliance with national and international laws and policies (European and Economic Council Directive 86/609, OJL 358, December 12,1987) after having obtained specific consensus from the Italian Ministry of Health.

2.4.1 Pig Experimental Protocol

Three- to four-month-old healthy farm pigs underwent ischemia-reperfusion and AAV injection as described in the following section. Cardiac magnetic resonance imaging (cMRI) was performed at 2 days and 1, 4 and 8 weeks after myocardial infarction.

Ten additional infarcted pigs, 5 receiving AAV6-miR-199a and 5 AAV6-Control, were injected intramuscularly every day for 10 days, starting from two days after surgery, with the thymidine analogue 5-bromo-2'-deoxyuridine (BrdU, Sigma; 10 mg/kg) re-suspended in 50% PBS and 50% DMSO. At day 12 after infarction, animals were sacrificed and organs were harvested as described above. Additionally, ten infarcted pigs (5 receiving AAV6-miR-199a and 5 AAV6-Control) were injected intramuscularly every day for 10 days with BrdU from day 20 after surgery, to the day of sacrifice, day 30.

After completion of the protocol, animals were sacrificed by arresting hearts in diastole with a i.v. injection of 10 ml of a saturated KCl solution (in bolus) and the chest was opened. Heart was sectioned as described in the Results section, Figure 6 F.

2.4.2 Myocardial infarction in pigs

Three to four month old male farm pigs, of 32-35 kg body weight, were fasted for 12 hours before surgery and received antibiotics and analgesics. Animals were sedated with an intramuscular injection of zoletil 8 mg/kg and ear vein and artery were cannulated for drug infusion and pressure monitoring, respectively. General anesthesia was subsequently induced with propofol (2–4 mg/kg). Immediately after, pigs were intubated by using an endotracheal tube and ventilated. Inhalatory anaesthesia was

kept by 2% isoflurane. Electrocardiogram, heart rate and arterial pressure were continuously monitored during the whole procedure. Thirty minutes before coronary occlusion, pigs received of amiodarone to prevent arrhythmias. Thoracotomy was performed by cutting the left forth intercostal space, and the pericardial sac was opened to expose the heart. The LAD was isolated from surrounding tissue distal to the first diagonal branch and closed by a suture. The two ends of the suture were threaded through a plastic tube and were cross-clamped after tightening to achieve coronary artery occlusion. LAD occlusion occurence was confirmed by the presence of ST elevation in the electrocardiogram and ventricular arrhythmias. In the case of ventricular fibrillation (VF), direct cardiac massage was performed with a frequency of 100/min and continued during the period of arrhythmia until the pigs were able to maintain the systolic pressure in normal ranges. Open-chest epicardial defibrillations were frequently necessary, and amiodarone and adrenaline were administered between the electrical discharge at 3-5 min intervals. After 90 minutes, coronary occlusion was removed to start the reperfusion phase. Subsequently, after 10 minutes of reperfusion, the animals were randomized in 2 groups receiving $2x10^{13}$ AAV6-Control (AAV6 carring an empty polylinker) or $2x10^{13}$ AAV6-miR-199a. Viral particles were suspended in a final volume of 2 ml in PBS and delivered as 20 direct injections in myocardium (100 μl per injection site), equally distributed along the border zone, identified as the margin of ischemic myocardium, pale compared to normally perfused myocardium. Three of the injection sites were marked with epicardial stitches which served as reference points for tissue sampling and histological analyses 12 days, 4 or 8 weeks after the open chest surgery. After injections, the chest was closed in layers, and the pneumothorax was reduced. In addition, a group of sham operated animals served as normal controls. The artificial ventilation was gradually suspended and antibiotics and analgesics were given after surgery.

2.4.3. Testing different AAV serotypes in pigs

In order to identify the AAV serotype able to transduce most efficiently pig hearts, 3 pigs were operated as described in the former section and $1x10^{12}$ viral particles of AAV6, AAV8, 9 carrying the EGFP gene were injected intramyocardially into the anterior wall of the left ventricle, in different sites marked with epicedial stitches. One month after injection, animals were euthanized, cardiac tissue was harvested from the injection sites

and each sample was snap frozen for DNA vector and transgene RNA expression quantification.

2.4.4 CMRI measurements in pigs

Swine were sedated with tiletamine hydrochloride and zolazepam hydrochloride and anesthesia was maintained by continuous infusion of propofol on spontaneous respiration. Animals were layed in a right lateral position with the heart at the isocenter on MRI unit. ECG leads were placed on the chest for vectorial gating image acquisition. Cine-MRI images were acquired with a 1.5 T scanner (Signa Excite HD; GE Medical Systems, Waukesha, WI, USA), using a non-breath-hold ECG gated, multi-NEX steady-state free precession pulse. LV functional parameters and infarct scar size were assessed following as described previously [167]. The heart was scanned along two long axis views (vertical and horizontal) and with a set of short axis views from atrioventricular valve plane to the apex as shown in Figure 6 G. Tagging-CMR images were acquired with an electrocardiography-gated, segmented K-space, fast gradient recalled echo pulse sequence with spatial modulation of magnetization to generate a grid tag pattern.

To assess the presence of the scar and quantify the extension of post infarction fibrosis, delayed enhanced images were acquired in two-dimensional T1 weighted segmented inversion recovery-prepared gradient echo-sequence 10 min after administration Gd-DTPA (0.2 mmol/kg iv) in short- and long-axis views correspondent to those of Cine-CMR.

2.5 CMRI data analyses

2.5.1 LV global and regional function

Global LV functional parameters, end-diastolic volume and end-systolic volume, ejection fraction, cardiac output, and left ventricular regional wall thickening (LVWT) were measured as previously described [167].

The end-diastolic and end-systolic volumes, together with other measurements (cardiac mass, EF, CO, LVWT) were automatically calculated by the commercially available research software package (Mass Analysis, Leyden, The Netherlands) upon manual trace

of LV endocardial and epicardial borders on all short-axis cine images at the end-diastolic and end-systolic frames.

Regional contractility was assessed by three indexes:

- end-systolic radial wall thickening (WT%).
- LV circumferential strain in short-axis slices (basal, middle, and apical).
- LV radial strain in short-axis slices (basal, middle, and apical).

The area of interest for the three measurements was the middle slice, which is orthogonal to LV long axis at 30% of its length starting from the apex. It was divided into 8 equal circumferential segments and the connection of the right ventricle to the left ventricle was defined as reference point for the segmentation. The 8 regions of the myocardium were: anterior (A), anterolateral (AL), lateral (L), inferolateral (IL), inferior (I), inferoseptal (IS), septal (S), anteroseptal (AS), and the region were acute ischemia and AAV injection was performed is the anterior as Figure 9 A and B shows.

LV contours drawn in the short-axis frames (Mass Analysis, Leiden, The Netherlands) were needed to calculate end-systolic and end-diastolic wall thicknesses. The percentage of WT (wall thickening) is calculated as follows:

WT = (EST-EDT) /EDT x 100

where EST was end-systolic thickness and EDT was end-diastolic thickness. EST, EDT and WT walues for each of the 8 segments were plotted to generate the curve and the area under curve (AUC) which was further used for statistical analyses.

Strain was calculated as the percent change of length in a specific direction where L0 is the original fiber length before deformation and L is current length (Lagrangian formula):

Strain (EL)=(L- L0)/ L0 (%)

Tagged cardiac images were analyzed using a custom software based on the method by Bogaert et al. [168].

All the data were blinded analyzed under the supervision of of a III-level EACVI (European association of cardiovascular imaging) cardiac MRI accreditated cardiologist.

2.5.2 Myocardial fibrosis

To determine the size of the fibrosis after infarction, gadolinium delayed contrast-

enhanced (Gd-DE) images in short axis view were acquired 10 min after intravenous administration of the contrast agent. The T1-weighted, short axis images were obtained in mid systole to decrease artefacts of premature ventricular complexes. The infarct zone was defined as area with SI > 5 SD above the mean SI of remote region.

All the data were blinded analyzed under the supervision of of a III-level EACVI (European association of cardiovascular imaging) cardiac MRI accreditated cardiologist.

2.5.3 Infarct core and peri-infarct area

The images acquired by Gd-DE were analyzed using custom-designed software to differentiate the dense infarct core from the heterogeneous peri- infarct area, or gray zone. The infarct core and peri-infarct area were quantified as a percentage of total myocardium endocardial upon manual trace of epicardial borders on the delayed-enhancement short-axis slices. The infarct core was defined as area with SI (signal density) >5 SD (standard deviation) above the mean SI of contralateral remote region of the myocardium, while gray zone was considered to have SI between 3 and 5 SD above normal myocardium.

Finally, the infarction core and the gray zone were quantified as a percentage of the total myocardium and as a percentage of the total infarct size [169].

All the data were blinded analyzed under the supervision of of a III-level EACVI (European association of cardiovascular imaging) cardiac MRI accreditated cardiologist.

2.5.4 Myocardial edema, area at risk and myocardial salvage

Infarct-related edema was considered present when the signal intensity on T2-weighted images was 2 times more of the mean SI of normal myocardium. Edema was manually traced on T2-weighted, short-axis images. Tissue weight in grams was calculated as the the product of myocardial volume and density (1.05 g/cm^3). Percentage of area at risk and myocardial salvage index were calculated as follow:

AAR (%) = Myocardial Edema (%) (at day 2) - Final Scar Size (%) (at 4 weeks)

Myocardial Salvage Index (%) = (AAR % / Myocardial Edema %) X 100

All the data were blinded analyzed under the supervision of of a III-level EACVI (European association of cardiovascular imaging) cardiac MRI accreditated cardiologist.

2.6 Surgical instrumentation in mice

The following section describes experiment made in the Bioexperimental facility at ICGEB, Trieste.

Animal care and treatment were conducted in conformity with institutional guidelines in compliance with national and international lawsand policies (European and Economic Council Directive 86/609, OJL 358, December 12,1987).

2.6.1 Intra-cardiac miRNA injection and MI

Intracardiac microRNA mimic injection and myocardial infarction induction have been extensively described in Lesizza et al. [170]. Briefly, CD1 mice were anesthetized by intraperithoneal injection of ketamine-xylazine (40 mg/kg-100 mg/kg, Imalgene 1000 and Sigma respectively), at a dosage of 1.2-1.3 μl/g and and intubated. Torax was incised, the 5th intercostal space was cut and enlarged to expose heart anterior wall. Twenty microliters of a mix of miRNA and lipids (ratio 1:1 in volume) was injected into the left ventricle. After injection torax was sutured mice were extubated to re-establish normal breathing. Lipid-mediated intracardiac miRNA delivery efficiency, animals received 200 pMoles of microRNA mimics (all from Dharmacon) mixed with 10 μl lipids, according to the manufacturers' specific protocols, in a total volume of 20 μl. In order to evaluate efficacy of miRNA transfection after MI, in a set of animals (n=13-20 per group) the anterior wall left anterior descending coronary artery was ligated 1 mm below the left atrium auricula. After myocardial infarction induction, intracardiac injection was performed after ligation as described above.

2.6.2 Echocardiography analysis

Heart function function was evaluated by echocardiography analysis as extensively described in Lesizza et al. [170]. Echocardiography was performed in anaesthetized mice 1, 2, 4 and 8 weeks after MI, using a Vevo 2100 Ultrasound (Visual Sonics) equipped with a MS550D 22–50 MHz linear array solid-state transducer.

2.7 Statistical analysis

Data are presented as mean ± standard error of the mean (SEM). Statistical analysis was performed by using a commercially available software package (GraphPad Prism). Differences among groups were compared by one- and two-way ANOVA followed by the Bonferroni post-hoc test. In particular, one-way ANOVA with Bonferroni post-hoc test has been used to compare means of two or more samples in order to determine whether there is statistical evidence that the associated population means are significantly different (e.g. Figure 5 E), while two-way ANOVA has been used to compare the effect of different treatments with multiple observations at different timepoint (e.g. Figure 25 A-C).

For survival analysis, Kaplan-Meier survival curve was generated and log-rank statistics test was rendered. For regional wall motion data, the area under the curve (AUC) was acquired by trapezoidal rule and analyses performed by one- and two-way ANOVA.

For all the statistical analyses, significance was accepted at $P<0.05$.

3. RESULTS

PART 1 – EFFICACY OF PRO-PROLIFERATIVE miRNAs IN HUMAN CARDIOMYOCYTES

The overall goal of this PhD project was to provide proof-of-principle evidence that a miRNA mimic therapy aimed at stimulating cardiomyocyte proliferation might be effective at inducing cardiac regeneration in a large animal model after MI, thus paving the way to possible clinical translation in humans. This work followed a previous study that identified, through a high throughput screening approach entailing the analysis of over 950 human miRNAs, those mimics that were active in stimulating proliferation of both mouse and rat primary neonatal cardiomyocytes [82].

3.1 Identification of the most effective microRNAs at inducing human cardiomyocyte proliferation

A first, fundamental step was to identify, among the miRNAs that were effective in rodent cells, those that were also active in human cardiomyocytes. In particular, for this analysis we concentrated our attention on 8 human microRNAs (hsa-miR-18a, hsa-miR-30e, hsa-miR-33b, hsa-miR-199a, hsa-miR-302d, hsa-miR-590, hsa-miR-1248 and hsa-miR-1825). Two of these miRNAs (miR-199a-3p and miR-30e-3p) are conserved among mouse, rat, human and pig, while others are not fully conserved or have been identified only in humans so far, according to miRbase release 21 (http://www.mirbase.org; **Figure 4**).

To obtain primary human cardiomyocytes, we set up a protocol to mechanically and enzymatically isolate human cardiomyocytes from 17-22-week-old-gestation abortive foetuses, which were obtained from the Children Hospital in Trieste upon ethical approval and consent. In brief, the developed protocol entailed heart explant and transportation to the laboratory, followed by isolation of ventricles, digestion of myocardial tissue with trypsin while pipetting for mechanical disaggregation of the tissue, followed by recovery of supernatants containing cardiomyocytes and plating (**Figure 5 A**).

As shown in **Figure 5 B** human fetal cardiomyocytes, displayed a rod shape structure during isolation, while they became flat after 4 days of culture. First we wanted to assess

permissivity of these cells to transduction using different AAV serotypes. AAV vector preparations expressing EGFP and corresponding to AAV6, AAV8 and AAV9 were used to transduce primary human fetal cardiomyocytes ($1x10^4$ v.g. per cell; data not shown). AAV6 was found to be the most effective (**Figure 5 B**) and was therefore used for all the subsequent experiments.

We tested the 8 selected microRNAs either as transgenes encoded by AAV6 or as transfected synthetic miRNA mimics (**Figure 5 D-G**) in isolated cardiomyocytes, identified by a marker of skeletal and cardiac muscle, sarcomeric- α -actinin. Cardiomyocyte proliferation was assessed by evaluating the percentage of cells that incorporated the nucleotide analogue EdU over 48 hours (**Figure 5 D-G**). Analysis of cells transfected with miRNA mimics using a lipofectamine-based carrier indicated that miR-33b*, miR-302d, miR-199a-3p and miR-1825 were able to significantly increase cardiomyocyte proliferation compared to untreated cells, or control cells treated with carrier alone or *C. elegans* miR-67 ($P<0.01$ for miR-33b*, miR-302d, with an increased of over 10-fold; $P<0.05$ for miR-199a-3p and miR-1825; **Figure 5 D and E**). In contrast, the extent of proliferation was markedly lower (maximum 1.5 fold over controls) in cells transduced with the corresponding AAV6 vectors. In this case, the effective miRNAs were miR-30e, miR-33b, miR-1248, miR-1825 ($P<0.01$) and miR-199a-3p ($P<0.05$; **Figure 5 F and G**). Of notice, miR-590, the most effective miRNA in driving mouse cardiomyocyte proliferation in our original screening [82] was ineffective as a mimic and even detrimental when its pre-miRNA DNA was delivered using the AAV6 vector. This result can be rationalized considering that, when expressed from AAV, both the 5p and 3p are produced, at ratio that might be different in each cell type and with ultimate cumulative effects that are unpredictable and possibly variable in different species.

PART 2 – EFFECT OF AAV-miR-199A DELIVERY AFTER MYOCARDIAL INFARCTION IN PIGS

3.2.1 AAV6 efficiently transduces porcine myocardium

AAV vectors of serotypes 6, 8 and 9 have been reported to transduce efficiently post-mitotic muscle fibres and cardiomyocytes, however with efficiency that varies among species, delivery route and in vivo vs. ex vivo application (reviewed in ref. [171]. We thus compared efficiency of AAV6, AAV8 and AAV9 carrying the reporter gene EGFP to select

the serotype with the highest transduction efficiency in the porcine myocardium. Vectors were injected into the left ventricular (LV) wall of 3 pigs ($1x10^{12}$ v.g. per injection per animal) and, one month later, viral DNA and EGFP mRNA were quantified in tissue samples. AAV6 displayed the highest transduction efficiency (**Figure 6 A and B**) and was thus selected for the rest of this study.

3.2.2 Persistent expression of miR-199a after AAV6-mediated delivery in infarcted pigs

Myocardial infarction (MI) was induced in 19 male farm pigs (3-4 months old) by occluding the left anterior descending coronary artery below the second diagonal branch during open-chest surgery. The occlusion was released 90 minutes later and, at 10 minutes of reperfusion, the animals were randomly divided into 2 groups receiving $2x10^{13}$ empty AAV6 (AAV6-Control, n=9) or $2x10^{13}$ AAV6-hsa-miR-199a (AAV6-miR-199a, n=10). An additional group of sham operated animals served as normal controls (n=6). AAVs were administered by a blinded operator who performed 20 injections directly in myocardium through the epicardium (100 µl of viral suspension per injection site). Injections were equally distributed along the infarct border zone of LV, which was identified by the operator as the margin of pale, ischemic myocardium (**Figure 6 C-E**). Some of the injection sites were tagged with epicardial stitches, hence myocardial samples in the corresponding territories could be easily detected and sampled post-mortem for histological analysis (as shown in **Figure 6 F**).

Animals from both groups that were sacrificed at 28 (AAV6-Control, n=4; AAV6-miR-199a, n=5) and additional infarcted animals sacrificed at 12 days, with or without infarction (n=3) were analysed for levels of transduction and transgene expression. The levels of hsa-miR-199a-3p in the injected areas were increased >18 and >27 folds at 12 and 28 days, respectively, compared to endogenous levels ($P<0.01$ in both cases; **Figure 6 G and H**), consistent with persistence of functional AAV transduction in the myocardium [171]. The levels of viral DNA in the myocardium of the injected animals were >18 times than those in the liver and >40 times than in other organs (liver, spleen, kidney and lung; **Figure 6 L**). The levels of hsa-miR-199a-3p RNA were not significantly increased in any other analysed organ, except the heart (**Figure 6 M**). No overt signs of pathology, including hyper-proliferation (as assessed by Ki-67 staining) were observed

(data not shown). Thus, AAV6 transduction and transgene expression remain relatively localized at the sites of intracardiac injection.

3.2.3 AAV6-miR-199a reduces post-infarct scar size

Cardiac morpho-functional assessment was performed using cardiac magnetic resonance imaging (CMRI). Nineteen infarcted pigs were scanned at 4 weeks post-MI, while half of them, randomly selected from both the AAV6-miR-199a and AAV6-Control groups (n=5 and n=4 respectively), were also scanned at 2 days post-MI to quantify ischemic myocardial edema, measures as enhanced T2-weighted signals in CMRI (**Figure 7 A**). No significant differences were detected between the two groups (30±4.7% vs 35±32.5% in AAV6-miR-199a and AAV6-Control groups respectively; **Figure 7 B**). Although myocardial infarct-related edema is not universally accepted as fully equivalent to the area at risk (i.e. the entire myocardial perfusion bed distal to the occluded coronary artery), still it was a surrogate marker to indicate similar extension of the infarct areas in the two groups.

The mass of damaged myocardium was identified and quantified by CMRI based on gadolinium delayed contrast-enhanced images (late gadolinium enhancement, LGE). At 2 days post-MI, the gadolinium-retaining region, defined as either infarct mass or size, was not significantly different between the two groups, indicating similar extent of initial myocardial damage (**Figure 7 C**), also in agreement with the measurements of edema. At 4 weeks post-MI, scar mass and size in the AAV-Control group were both unchanged compared to gadolinium retaining-myocardium quantified at day 2; in contrast, in the AAV6-miR-199a group there was over 50% reduction in both measurements (LGE mass 7±2 vs 15±2.5 at 28 days, % LGE size 13±3.2% vs 23±4% at 28 days; $P<0.01$; **Figure 7 C)**.

Representative LGE-CMRI images showing 5 cross-sectional planes (a-e, **Figure 7 G**) of hearts from 2 pigs in the AAV-Control and 2 pigs in the AAV-miR-199a groups at days 2 and 28 after MI are shown in **Figure 7 F**. A marked reduction in scar size at day 28 compared to the damaged area at day 2 is appreciable in the animals which received AAV-miR-199a-a. For two representative animals, gross anatomy of cardiac slices with corresponding LGE-MRI images in AAV6-Control and AAV6-miR-199a at day 28 after MI are shown in **Figure 7 D** and **E** respectively.

The infarct region included a "core" fibrotic area and a surrounding "gray zone", comprising a mixture of viable myocardium and fibrotic areas (**Figure 7 H**). At 28 days post-MI, the core was significantly smaller in the AAV6-miR-199a group, while the gray zone was not significantly different between the two groups, consistent with a lower core/gray zone ratio in the group that benefited from miR-199a expression (infarct core mass 5±1 vs 12±2.5; core/gray zone ratio 5±1 vs 3±0.7; $P<0.01$; **Figure 7 I**). The reduced scar size and the increased proportion of mixed tissue compared to fully fibrous tissue were suggestive of a process of regeneration in previously damaged regions after delivery of miR-199a.

3.2.4 Recovery of global and regional cardiac function in miR-199a-treated animals at one month after MI

Multiple functional parameters were analysed by CMRI in animals treated with AAV6-Control and AAV6-miR-199a which displayed not significantly different heart rates. LV ejection fraction was significantly depressed at day 2 after MI in both groups, however selectively recovered at 28 days in animals injected with AAV6-miR-199a while it further deteriorated in the controls (66±3% vs 54±4% in AAV6-miR-199a and AAV6-Control groups, 28 days after treatment respectively, $P<0.05$ **Figure 8 A**). Similarly, there was a statistically significant difference between the two groups in LV stroke volume, also indicative of improvement in global contractile function (50±3.7% vs 40±1.5% at 28 days, $P<0.05$; **Figure 8 B**). Both LV end-systolic and end-diastolic volumes tended to deteriorate in the infarcted animals, indicating remodelling with cardiac dilatation, however there was a statistically significant preservation of end-systolic volume in the AAV6-miR-199a group (LVESV 30±2.7% vs 42±3.5% at 28 days; LVEDV 69±8% vs 87±11% at 28 days; $P<0.05$; **Figure 8 C** and **D** respectively).

In addition to global cardiac function, CMRI was also used to assess regional/segmental contractility, which appeared of particular importance since AAVs were injected selectively along the border zone of MI, with the potential to underestimate their local effect using global contractility indexes exclusively. Regional function was assessed by MRI-tagging **(Figure 9 A**) to measure circumferential strain (E_{CC}) and radial strain (E_{RR}). These two indexes were evaluated along short-axis LV slices (basal, middle, and apical) divided into 8 equal circumferential segments, starting from the line of attachment of the right ventricle to the LV, which served as the reference point (**Figure 9 B**). The

values for E_{RR} and E_{CC}, obtained for each segment, were plotted to generate curves (**Figure 9 C** and **D** respectively) and, subsequently, the area under the curve (AUC) was calculated to integrate all the values along the LV circumference (scheme in **Figure 9 E** and values in **Figure 9 F** and **G** respectively). The segmental analysis indicated that, at 30 days after MI, both E_{CC} and E_{RR}, were significantly lower in the AAV6-Control MI group, compared to sham operated pigs, however they were almost completely recovered in the AAV6-miR-199a group, especially the E_{CC} (E_{RR} 540±60 vs 180±50; E_{CC} - 250±30 vs 160±27 ; P<0.01; **Figure 9 F** and **G** respectively). Percent of systolic LV wall thickening (LVWT) was also assessed, with no need for tagging, using the same approach, obtaining very similar results (LVWT 550±70 vs 200±90; P<0.01; **Figure 9 H and I**).

Finally, the 'first-pass' method based on image acquisitions immediately after bolus injection of gadolinium was employed to semi-quantitatively assess myocardial perfusion. No significant difference was detected between the two groups of infarcted pigs in any LV region and at any time point (data not shown).

Taken together, these findings indicate that the detected morphological improvements were paralleled by significant recovery of global and regional contractile function.

3.2.5 AAV6-miR-199a induces CMs proliferation

We wanted to understand the molecular correlates of reduced infarct size and improved cardiac function of the AAV6-miR-199a-treated pigs. Our previous work showed that delivery of the same vector, using the AAV9 capsid, to infarcted hearts in mice induced in vivo cardiomyocyte proliferation and cardiac regeneration [82]. To test the pro-proliferative effect in pig, we injected AAV6-Control and AAV6-miR-199a in an additional set of animals (n=3 per group), subjected to ischemia reperfusion using the same protocol as above. These animals received 10 intramuscular injection of BrdU every day from day 2 to day 12 after MI and then sacrificed (**Figure 10 A**). In the infarct border zone of the animals treated with AAV6-miR-199a we observed the presence of large cells with cardiomyocyte morphology clearly positive for the proliferation marker Ki-67 (7.6±0.5% of cardiomyocyte in the injected area compared to 1.9±0.2% in control animals; P<0.05 (**Figure 11 A and B**). This was consistent with increase in cardiomyocytes with BrdU-positive nuclei (an S-phase marker; 8.9±1.1% vs. 2.2±0.3%;

P<0.05 (**Figure 10 B and C**), staining for phosphorylated histone H3 (pH3, a marker of passage through G2/M; 0.75±0.05% vs. 0.19±0.02%; *P*<0.05 (**Figure 11 E and F**) and, occasionally in only the miR-199a group, Aurora B kinase localization in mid-bodies, marking cells undergoing karyokinesis (**Figure 11 M**).

Another set of animals was submitted to the same infarction protocol as above and treated with AAV6-Control and AAV6-miR-199a (n=3 per group), however these animals were injected with BrdU from day 20 to day 30 to assess proliferation at 1 month (**Figure 10 D**). At this time point, analysis of Ki-67 and pH3 revealed that proliferation was almost extinguished (**Figure 11 C, D** and **G and H** respectively); a few cardiomyocytes in the AAV-miR-199a group were still positive for BrdU (8.8±0.9% vs. 3.5±0.5%; *P*<0.05), most likely indicative of still ongoing duplication in the 10 days prior to sacrifice (**Figure 10 E and F**). **Figure 11 I** and **L** show the percentages of Ki67- and pH3-positive cardiomyocytes, respectively, at 12 and 30 days after infarction. Both measurements provide an indication of the current proliferation activity at the time of analysis and are concordant in showing quenching of proliferation at one month after treatment.

These findings collectively indicate that expression of miR-199a after MI markedly boosts endogenous CM proliferation.

3.2.6 Histological and molecular analysis of infarcted hearts treated with AAV6-miR-199a

We wanted to assess the histological and molecular correlates of increased CM proliferation in the animals treated with AAV6-miR-199a. Concordant with the CMRI data, we observed that, at 28 days after MI and vector injection, there was a significant reduction of the fibrotic area in the infarcted region (representative images from three different animals at various magnifications and quantification in **Figure 12 A and B**). In the infarct border zone, in which the vectors had been injected, increased proliferation in the AAV6-miR-199a animals was paralleled by the presence of a vast number of cells with CM morphology expressing GATA4, a transcription factor essential for cardiac development and known to be expressed de novo during zebrafish heart regeneration [172]. GATA4 normally localizes in the nucleus where it promotes transcription of cardiac specific genes; however, cytoplasmic expression is also known to occur during embryonic development, at day 9.5 in the mouse [173]. In the animals treated with

AAV6-miR-199a, a relatively large number of CMs showed GATA4 cytoplasmic localization at both 12 and 30 days after MI and vector injection (2.5±0.5% of cytoplasmic GATA4 CMs vs. 0.5±0.5% in treated and control animals at day 12, respectively; 1.9±0.4% of cytoplasmic GATA4 CMs vs. 0.4±0.3% in treated and control animals at day 30, respectively; $P<0.05$; **Figure 13 A-D**).

There were no significant differences in the levels of other markers of muscle and vascular pathology in the miR-199a-treated animals compared to infarcted controls, including desmin (which is essential for maintaining structural and functional integrity of myocytes [174] and was expressed at normally high levels, **Figure 13 E**), myogenin (which coordinates skeletal myogenesis and repair [175] and was not expressed **Figure 13 F**), endothelin-B receptor (which selectively stained arterioles' smooth muscle cells [176], **Figure 13 G**) and Wilms' tumor protein 1 [177] (Wt1, which was expressed at low levels in the vascular endothelium but not in myocytes **Figure 13 H**).

Vessel density was assessed by staining endothelial cells with fluorescinated lectin and arterioles with an anti-α-SMA antibody. No significant difference was detected in vessel morphology and capillary density compared to cardiomyocytes at either 12 or 30 days after treatment between the two infarcted and treated groups (data not shown).

Finally, we analysed the hypertrophic response after MI. In infarcted pigs treated with AAV6-Control both atrial natriuretic peptide (ANP) and bone natriuretic peptide (BNP) were increased at both 12 days and 1 month after infarction, while this response was blunted in the animals treated with AAV6-miR-199a (**Figure 15 E**, **F and C and D** respectively). Consistent with preservation of cardiac function, the ratio between transcripts for the adult α- and the fetal β-myosin heavy chains was preserved in the AAV6-miR-199a treated animals at both time points (**Figure 15 A and B**). Preservation from maladaptive hypertrophy by miR-199a was also observed at 1 month after treatment both macroscopically post-mortem (representative animal shown in (**Figure 14 C**) and at the histological levels, by quantifying CM area after staining heart histological section with lectin WGA (wheat germ agglutinin) or periodic-acid-Schiff (PAS). This measurement revealed reduction of the hypertrophic response in the AAV6-miR-199a-treated animals compared to controls (**Figure 14 A and B**).

When analysed collectively, these findings are concordant in showing that increased cardiac regeneration in the miR-199a animals was paralleled by the expression of the

developmental marker GATA4 in the absence of overt markers of cardiac or vascular pathology.

3.2.7 Sudden death and pathological findings in the longer term in pigs treated with AAV6-miR-199a despite morphological and functional recovery

A subset of infarcted animals treated with AAV6-Control (n=6) and AAV6-miR-199a (n=7) was followed up for a longer time period. In one of the pigs analysed at 8 weeks, CMRI continued to show persistent beneficial effects on cardiac morphology and function, with progressive reduction of cardiac scar (LGE-CMRI images showing 4 cross-sectional planes at 1, 4 and 8 weeks in this animal and in a representative AAV6-Control animal shown in **Figure 16 A**). However, despite these persistent beneficial effects on post-MI scar extension and ventricular function, 6 out of 7 pigs in the of AAV6-miR-199a group died from sudden death in the absence of preceding clinical signs during weeks 7-8. Their mortality was significantly higher compared to AAV6-Control, in which only one death was recorded in the first 8 weeks (**Figure 16 B**). In one of the pigs treated with AAV6-miR-199a, it was possible to record, thanks to a subcutaneously implanted recorder (Reveal, Medtronic), that its sudden death was due a tachyarrhythmia evolving into ventricular fibrillation (**Figure 17**).

Cardiac tissue from the pig which survived at 8 weeks and from the other pigs which died at 7-8 weeks was retrieved for histological analysis (**Figure 16 C**). Careful examination of haematoxylin-eosin-stained tissue sections revealed, in three of the pigs injected with miR-199a, the occasional presence of small clusters of cells infiltrating the myocardium. These cells were negative for the leukocyte common antigen CD45 (excluding their myeloid or lymphoid derivation as inflammatory cells) and CD34 (blast cells of hematopoietic origin or activated endothelium) and were highly proliferating, as concluded from virtually complete positivity for Ki-67 expression. Cells were also negative for markers of muscle differentiation, including desmin (identifying myogenic cells of cardiac, smooth and striated muscle), sarcomeric α-actinin (which labels Z lines in the cardiac and skeletal muscle sarcomere) and HHF35 (a monoclonal antibody recognizing muscle-specific α- and γ-actin); cells were also negative for Wt1 (marking several malignancies). The infiltrating cells, however, were positive for a few antigens known to be expressed during early myogenic development, including two main myogenic transcription factors (GATA4, which is critical for proper mammalian cardiac

development), and myogenin (the reactivation of which characterizes rhabdomyosarcoma cells) as well as the calmodulin-binding protein caldesmon (which regulates smooth muscle contraction and is expressed at high levels in leiomyoma and leiomyosarcoma) and the endothelin-B receptor, which is expressed in smooth muscle cells. Collectively, therefore, these cells appear to show markers of early muscular differentiation.

Even if these few clusters of cells found in AAV6-miR-199a hearts were highly proliferating and appeared to have an infiltrating phenotype, no other pathological cell expansion was found in other organs, nor abnormal cell growth or tumours were found during necropsy in any of the treated animals.

PART 3 – DELIVERY OF microRNA MIMICS IN MOUSE HEARTS

AAV vectors are excellent tools for myocardial gene transfer in terms of capacity to delivery their genes to post-mitotic cells selectively, including cardiomyocytes. However, these vectors persist, in the form of episomal, concatamerized, nucler DNA, for indefinite periods of time in the transduced cells, virtually coinciding with the life of the animals. This characteristics is obviously desirable for gene therapy of inherited disorders, however becomes problematic for the delivery of a pro-proliferative factors, as the long-term results observed in pigs also highlighted.

As an alternative to the use of viral vectors, we wanted to evaluate the efficacy of synthetic miRNA mimics at inducing myocardial repair after single intracardiac injection using synthetic lipid formulations as delivery tool.

3.3.1 Commercial lipid formulations to vehicle miR-199a to the heart

The clinical translation of microRNA treatment for cardiac regeneration will necessarily entail the development of an administration protocol that combines the best efficacy with the highest standards of safety. With this ultimate goal in mind, we designed a set of experiments to test and compare the performance of different commercial lipid transfecting agents to vehicle microRNA mimics to the heart. We selected 5 different commercial lipid formulations: Oligofectamine, Lipofectamine 2000, Xtreme Gene and INTERFERin, and assayed their efficacy to transfect an siRNA targeting the *Ubc* gene in the ubiquitination cascade in primary neonatal rat cardiomyocytes. This gene is

essential for cell viability [178], including that of cardiomyocytes [82]. We comparatively evaluated transfection efficiency, measured as the percentage of sarcomeric alpha actinin-positive cells dying upon treatment (**Figure 18 A**) or by measuring ATP production as surrogate for survival (**Figure 18 B**); the latter measurement was also informative for all the cell types present in the primary culture, including, besides cardiomyocytes also fibroblasts and endothelial cells, and also took into account the overall toxicity of the vehicle alone. We found that lipofectamine RNAiMax had the highest transfection efficiency in neonatal rat cardiomyocytes, evaluated with both techniques (around 80% of transfected cells), among the tested reagents.

Next we tested the three lipid formulations that were most effective in vitro, plus one additional lipid reported to work in vivo in other tissues (Invivofectamine), for their ability to deliver the miR-199a-3p mimic in vivo in the heart of 2-month old CD31 female mice (n=6 per group). Two days after intracardiac injections of the different RNA-lipid complexes, we evaluated the levels of miR-199a-3p expression in the anterior wall of left ventricles as well as the expression of genes that are known be targeted directly by miR-199a, *Homer1* and *Clic5*, which were used to assess microRNA function. With all lipid formulations, but most remarkably with Lipofectamine 2000 and Lipofectamine RNAiMax, we observed a consistent and significant increase in the amount of miR-199a-3p, which was over 250 folds the endogenous one (**Figure 18 C**), paralleled by a decrease in the mRNAs of *Homer1* and *Clic5* ((*P*<0.05; **Figure 18 D**). This indicated effective transfection in vivo using the developed protocol.

Finally, we assessed the microRNA extracardiac dissemination in mice injected with Lipofectamine RNAiMax/miR-199a-3p. Over several organs examined, only liver and kidney displayed a significant upregulation of miR-199a-3p, 4.7-fold and 8.3 fold over the endogenous levels respectively (*P*<0.05 in both cases; **Figure 18 E**).

Together, these results indicated that miR-199a-3p in vivo transfection can be achieved by a single intracardiac injection exploiting cationic lipid formulations.

Lipofectamine RNAiMax was chosen for all the subsequent in vivo studies described below.

3.3.2 MicroRNA persistence after intracardiac injection

To assess the potential of microRNA mimic in pro-regenerative therapy, next we evaluated microRNA persistence after intracardiac injection, in mice, of complexes of

Lipofectamine RNAiMax/miR-199a-3p or Lipofectamine RNAiMax/cel-miR-67 (*Caenorhabditis elegans* miR-67, a nontargeting mimic used as a control; n=6 per group). Levels of the microRNA mimics, as quantified by qRT-PCR from the left ventricle free wall, were very high, 296.0±21.9-fold over control, at 2 days after intracardiac injection (**Figure 19 B**) and progressively decreased over time (37.0±4.0-fold at 4 days, 7.6±1.1-fold at 8 days and 2.2±0.2-fold at 12 days), until disappearing at 20 days from treatment (P<0.05 at all time points; **Figure 19 B**).

At 2 and 4 days after injection (**Figures 19 C and D** respectively), persistence of the mimic was associated with the downregulation of the microRNA targets mRNA *Homer1* and *Clic5,* thus indicating that the injected miRNA was biologically active. However, Homer1 and Clic5 mRNA levels were no more significantly downregulated at 12 (**Figure 19 E**) and 20 days (**Figure 19 F**) after mimic intracardiac injection.
Collectively, these results indicate that, after direct intramyocardial injection, mi-199a mimic exert a functional effect lasting several days.

3.3.3 MiR-199a-3p mimic single intracardiac injection improves cardiac function after MI

The experiments described above demonstrated that it was possible to achieve efficient in vivo microRNA mimic transfection, which lasted for several days. Thus we wanted to evaluate the efficacy of mimic injection after MI.

After permanent ligation of the left anterior descending coronary artery, 2 month-old CD1 female mice received 2.7 μg miR-199a-3p (n=20) or cel-miR-67 (n=13) complexed with Lipofectamine RNAiMax injected into the surviving peri-infarcted myocardium. Five and 3 animals died in cel-miR-67 and miR-199a-3p groups, respectively, within the first 20 days (**Figure 20 A**).

Echocardiography measurements monitored cardiac function of the surviving animals, displaying comparable heart rate, up to 8 weeks from treatment. Cel-miR-67 injected animals displayed a progressive impairment of LVEF from week 1 to week 8, (24±8.1% at week 8) (**Figure 20 B**). In contrast, while LVEF of miR-199a-3p-injected animals was comparable to that of controls during the first 2 weeks, from this time point it remained constant up to 8 weeks (LVEF at week 8 was 37.5±4.5%; P<0.05 vs. control) (**Figure 20 B**).

In a consistent manner, analysis of other cardiac function parameters obtained by echocardiography, including LV fractional shortening (**Figure 20 C**) and LV anterior wall (**Figure 21 A and B**) and septum thickness showed a similar trend (**Figure 21 C**). Left ventricle systolic internal diameter was not increased by miR-199a-3p treatment at all the time-points analysed (**Figure 20 D**) indicating that there was no further cardiac dilatation upon mimic injection. In addition, animals in the miR-199a-3p group displayed no further hypertrophic response of cardiomyocytes after MI compared to control animals (**Figure 22 A and B**).

At the moment of sacrifice, 8 weeks after MI, infarct size measured by Masson's tricrome staining was significantly reduced in miR-199a-3p treated animal (28±4.8% of the LV in control animals versus 18±3.0% in the miR-199a-3p-treated group ($P<0.05$; **Figure 23 A and B**).

Some animals were injected with ethynyl-29-deoxy-uridine (EdU), a thymidine analogue (n=6 per treatment), every second day from day 1 to day 12 after MI and miRNA mimic treatment to assess cell passage through the S phase. Animals treated with miR-199a-3p showed a 2.5-fold increase in the number of cardiomyocytes that had incorporated EdU (**Figure 23 C and D**). Likewise, immunofluorescence for the phosphorylation of histone 3 on serine 10, a marker of late G2/M, showed increase positivity at day 4 after MI and miR-199a-3p treatment (**Figure 23 E and F**), as was the number of cardiomyocytes positive for Aurora B, which showed nuclear but also midbody localization, indicating passage through mitosis (**Figure 23 G and H**).

Finally, miR-199a-3p treatment had no effect on cardiomyocyte protection from cell death as analyzed by terminal de-oxynucleotidyl transferase dUTP nick end labeling staining two days after MI and mimic injection (**Figure 23 I and L**).

Collectively, these results demonstrate that transfection of miR-199a-3p mimic leads to cardiac repair by stimulating cardiomyocyte proliferation and therefore preserves cardiac function after MI.

PART 4 – CHEMICAL MODIFICATIONS OF miR-199a-3p TO INCREASE STABILITY AND EFFICACY

3.4 miR-199a-3p mimic chemical modification to increase its stability

Once injected in vivo, microRNAs are subject to degradation by abundant ribonucleases present in the blood and extracellular matrix. We therefore tested five chemical modifications of miR-199a-3p to assess whether they increased their stability while preserving efficacy. In addition to the original mimic formulation purchased from Dharmacon, which was used for all the other experiments described in this thesis so far (**Figure 24 A**), the following modified mimics were obtained:

- E1: LNA and phosphorothioate stabilization at 5′ and 3′;
- E2: LNA plus a phosphorothioate stabilization at 5′ and 3 and a 2′-O-Me modification on the passenger strand;
- E3: 2-F mimic plus a phosphorothioate stabilization and a 2′-O-Me modification on the passenger strand (design A);
- E4. 2-F mimic plus phosphorothioate stabilization and 2′-O-Me modification on the passenger (design B);
- I: 2′-O-Me modification on the driver strand, in order for the passenger to become inactivated and not enter RISC;

Mimics E1, E2, E3 and E4 were provided by Exiqon according to a proprietary design; differences among design A and B of sequences E3 and E4 are not disclosed by the vendor. Mimic I was provided to us by Integrated DNA Technologies (IDT) (**Figure 24 A**).

These mimics were first tested in neonatal rat cardiomyocytes by assessing the stimulation of proliferation rate by EdU incorporation at 72 hour after transfection. All mimics were able to increase cardiomyocyte proliferation at least as efficiently as the standard formulation from Dharmacon (**Figure 24 B and C**). Accordingly, all mimics also decreased the mRNAs of the target genes *Homer* and *Clic5* (**Figure 24 D and E**). The top scoring molecule in this comparison was mimic E3 from Exiqon.

We further evaluated stability and persistence of mimics E3 (Exiqon), I (IDT) and the Dharmacon mimic after direct intracardiac injection in adult mice by quantifying their relative levels at days 2, 8 and 21 after injection (n=6 for each group; cel-miR-67 injected mice served as control; **Figure 24 A-C**). At day 2, mimic E3 was upregulated 800 folds over control, while I and Dharmacon mimic levels were approximately 200 folds over control (**Figure 25 A**). At day 21, however, the levels of mimic I were significantly (approximately 6 fold) higher than those of the other two mimics (**Figure 25 C**). The levels of two miR-199a-3p direct gene mRNAs, *Homer* and *Clic5*, were downregulated at 2 and 8 days but not at 21 days after injection (**Figure 25 D-I**).

Mimic I, the levels of which were the highest among the mimics tested at 21 days, were further assessed in mice subject to MI by the permanent ligation of the left anterior descending coronary artery. After MI induction and mimic intracardiac injection (cel-miR-67 served as control, n=6 per group), functional parameters were followed by echocardiography up to 8 weeks. While cel-miR-67-injected mice displayed a progressive impairment in heart function, as expected, LVEF in the two miR-199a-3p groups remained stable up to 8 weeks after MI (at 8 weeks: miR-199a-3p Dharmacon LVEF 29±4.5%; miR-199a-3p I LVEF 28±5.3%) (**Figure 26 A**). Left ventricle ejection fraction and LV telediastolic volume did not show any significant difference between miR-199a-3p Dharmacon and miR-199a-3p I groups at all the time points analysed (**Figure 26 A and C**). However, LV anterior wall was increased, even if not significantly, in miR-199a-3p I injected mice (**Figure 26 B**).

Together, these results indicate that miR-199a-3p I is the more stable than miR-199a-3p Dharmacon when injected in vivo. Nevertheless, miR-199a-3p I injection after MI exerts the same beneficial effect on heart function as that obtained using miR-199a-3p from Dharmacon.

4. DISCUSSION

Achieving functional regeneration of damaged hearts represents a long sought goal of clinical and experimental research. Following the general disappointment of approaches based on the implantation of stem cells of various derivation, which were shown to essential act through paracrine secretion of beneficial factors rather than generation of contractile myocardium (see Introduction), the identification of a normal turnover of cardiac myocytes during the adult life has opened the perspective of achieving cardiac regeneration through the stimulation of already existing cardiomyocytes to enter the cell cycle. Studies based on the incorporation of atmospheric C14 in humans [11] or imaging mass spectrometry in mice [7] are concordant in showing that approximately 1% cardiomyocytes are generated every year, a percentage that increases 2-3 times after MI. These observations not only show that the heart is not a completely post-mitotic organ, but also offer a rationale for innovative therapies aimed at stimulating this small, but existing replicative potential.

Previous work from the Molecular Medicine Laboratory at the ICGEB in Trieste has shown that a series of microRNAs are capable to stimulate neonatal cardiac myocytes from rats and mice to proliferate and that AAV vectors expressing two of these miRNAs (miR-590 and miR-199a) are effective at stimulating cardiac repair after MI in vivo [82]. The use of miRNAs as genetic tools to stimulate cardiac proliferation is of particular interest, in light of the capacity of these molecules to regulate expression of multiple genes simultaneously. In contrast to the overexpression of individual cDNAs or the downregulation of individual genes by RNAi or knock-out technologies, the use of miRNAs offers the advantage that these molecules are pleiotropic in their action, a property appearing desirable in light of awakening a complex process such as that of cardiomyocyte proliferation. For example, work carried out in the laboratory over the last years has shown that transduction of a single gene, such as the powerful inducer of cardiomyocyte proliferation during the embryonic life Notch1, is indeed capable to stimulate proliferation of cardiomyocytes at birth, but is inactive in doing so in adult cells [179]. MicroRNAs, in contrast, by targeting multiple transcripts simultaneously, are more likely to modulate biological pathways or functions and thus, in principle, more likely to be effective than single genes. This property, however, has the drawback that the effect of miRNAs is more pleiotropic than that of individual genes, a concept that

well applies to the long term, deleterious effect of miR-199a expression observed in pigs, which will be described later.

Based on the previous results that had led to the identification of miRNAs promoting proliferation of rodent cardiomyocytes, the overall objective of this Thesis has been to explore the potential for clinical translation of a miRNA-based approach to achieve cardiac repair after myocardial infarction. The proof of safety and efficacy of a new drug or therapeutic treatment in large animal models is a fundamental step toward the approval of its use in a clinical experimentation. This has been the specific subject of this study.

4.1. microRNA candidate selection to induce human cardiomyocyte proliferation

To identify the microRNA candidates potentially able to induce adult human cardiomyocyte proliferation, eight human microRNAs selected from the original high-throughput screening performed in neonatal rodent cells [82], were tested in cardiomyocytes derived from human ES- and iPS-cells for their capability in boosting cell-cycle reentry (data not shown). However, the procedures for differentiating cardiomyocytes from ES- and iPS-cells generate cardiomyocytes that are rather immature and resemble early embryonic cardiomyocytes. In the experiments performed with these cardiomyocytes, for example, the most effective miRNAs were those belonging to the miR-302/miR-367 cluster, known to be overexpressed in ES cells and be required to maintain their undifferentiated phenotype [180] – data not shown. This does not necessarily reflect the capacity of these miRNAs to act on more differentiated cardiomyocytes.

For this reason, we decided to test the cherry-picked eight microRNAs in primary cardiomyocytes cultures established from 17-22-week-old-gestation human abortive fetuses. These cells, although still not fully differentiated, appear to represent a more reliable and robust model for human cardiomyocytes. Our experiments revealed that several of the selected microRNAs were able to induce DNA synthesis and G2/M phase transition measured as EdU incorporation (Figure 4) and phospho-histone 3 positive immunofluorescence (data not shown) respectively. Of note, the effect was much stronger when the microRNAs were delivered as synthetic mimics, rather then as transgenes expressed by AAV vectors, even after efficient viral transduction (Figure 4C).

Some of the microRNAs tested had very modest effect on cardiomyocyte proliferation, such as miR-18a*, or miR-30e* and miR-590-3p; of note, miR-590, when delivered as precursor using an AAV vector, was even detrimental to cell proliferation, suggesting that the 5p strand has opposite effects and might compete with the 3p for RISC incorporation and target mRNA inhibition. This is a testable hypothesis for future investigational work.

MicroRNA-33b* and miR-302d were able to induce 12- and 10- fold cardiomyocyte proliferation increase over control (cel-miR-67) respectively when delivered as synthetic mimics. However, miR-33b* has a controversial role in cancer expansion [181, 182], while miR-302d long-term expression is already known to induce cardiomyocyte dedifferentiation and dysfunction [89], thus limiting their potential use for human therapeutic applications. MicroRNA-199a-3p, miR-1248-3p, and miR-1825-3p mimics boosted cardiomyocyte proliferation approximately 5-folds compared to control. However, the last two miRNAs are absent in mouse, rat and pig, thus making their characterization and definition of the mechanism of action difficult to study. On the contrary, the miR-199a sequence is fully conserved in human, mouse, rat and pig, and the role of this miRNA in many different biological processes, including proliferation, metabolism, hypertrophy, autophagy and cell death, has been extensively studied and elucidated (see Introduction). In light of these considerations, miR-199a-3p was selected for further safety and efficacy studies in a large animal model.

4.2. AAV6-miR-199a intra-cardiac injection after myocardial infarction in pigs improves cardiac morphology and function

The study we conducted to prove efficacy of miR-199a in pigs entailed the induction of myocardial infarction by a 90-minute occlusion of the second branch of left anterior descending coronary artery (LAD) in 3 to 4-month-old farm pigs, and the subsequent delivery of an AAV6 vector carrying the miR-199a precursor DNA by 20 direct injections into the infarct border zone. Animal cardiac function and infarct size were followed by late gadolinium-enhancement cardiac magnetic resonance 2 and 30 days after surgery.

Imaging analysis performed at day 2 after infarction by cMRI showed no difference in the extension of the myocardial damage between controls (AAV6-Control) and AAV6-miR-199a-treated animals. On the contrary, cMRI at one week after surgery already

highlighted a beneficial effect of the microRNA treatment (data not shown), which turned to a significant reduction of the infarct core region after one month.

Analysis of the individual animals over time by cMRI was consistent with the conclusion that AAV6-miR-199a stimulated a regenerative process progressively healing the damaged myocardium. Consistent with this morphological conclusion, cMRI performed at one month after MI and vector delivery showed significant improvement of ejection fraction and other functional parameters in the AAV6-miR-199a-treated animals, indicating better global cardiac function. Both global and regional contractility resulted significantly improved at one month after treatment, the latter measured by assessing circumferential and radial strain by tagging MRI. Of note, cMRI currently represents the gold standard for the objective, unbiased evaluation of cardiac function.

Could myocardial tissue recovery and improved cardiac function be ascribed to an effect of AAV6-miR-199a on cardiomyocyte survival after MI? Several considerations appear to be against this possibility. First, our previous work has explored whether the most effective pro-proliferative miRNAs that our screening identified, including miR-199a-3p, exert an anti-apoptotic effect, but failed to identify such activity [82]. In the infarcted pigs sacrificed at 12 days for the BrdU incorporation studies in this work we extensively searched for TUNEL-positive cardiomyocytes, without finding any evidence of protection from apoptosis in the AAV6-miR-199a-injected animals. Consistent with this result, protection from cardiomyocyte death was neither detected in mice injected with miR-199a-3p mimics, even when the analysis was performed at the more informative time point of 2 days after infarction detected [170].

Second, analysis of the extent of edema and measurement of infarct mass and size at 2 days after MI are concordant in showing similar extent of myocardial damage. Should AAV6-miR-199a be effective in preventing cardiomyocyte loss immediately after infarction, its effect would be likely of having been observed also at this early time point. In this respect, it is worth mentioning that, in normal tissue, AAV vectors are well known to take several days to reach maximum transgene expression [183]. However, in damaged tissues, such as the infarcted heart or skeletal muscle, expression initiates few hours after cell infection and raises rapidly [184].

Third, the increase in cardiac mass observed by cMRI in the AAV6-miR-199a animals was paralleled by the appearance of a large number of BrdU-positive and Ki-67-positive cells in the infarct border zone, the same regions where the vectors were injected. These cells

not only entered the cell cycle (Ki-67) and synthesized new DNA (BrdU), but also traveled through G2/M (positivity for phosphorylated H3) and, more occasionally, showed localization of the Aurora B kinase in midbodies, a marker of cell division. Based on these considerations, it appears plausible to conclude that the reduced infarct size and improved myocardial function observed in the AAV6-miR-199a animals might be ascribed to a true regenerative process.

When analyzing cardiomyocyte proliferation in the miR-199a animals, we observed that the proliferative activity of cardiomyocytes was relatively high at 12 days after MI and vector administration, while it was significantly quenched at one month. At this latter time point, there was still a significantly increased number of BrdU cells, however this most likely reflected incorporation of this analogue in the 10 days prior to sacrifice, when the animals were administered with the drug, since analysis of Ki-67 by immunohistochemistry and phospho-H3 by immunofluorescence revealed no differences in the AAV6-miR-199a group compared to the control one. This result is of potential biological interest, since it might indicate that the stimulus exerted by miR-199a expression might be essential but not sufficient to drive cardiomyocyte proliferation, which would instead also require a proper permissive environment, for example generated by the secretion of still unidentified growth factors from the damaged myocardium (which would occur immediately after damage but not one month later). This conclusion also appears consistent with our observation that the injection of AAV vectors expressing miR-199a in un-infarcted, normal both mouse and in pig heart exerts no apparent effect (data not shown).

In our study, we decided to express miR-199a from its precursor DNA for practical reasons and taking advantage of the high efficiency of AAV vectors in the myocardium. In this experimental setting, both microRNA strands are expressed at high levels (data not shown) and, consequently, we could expect the induction of additional effects specific for miR-199a-5p. In particular, this miRNA was shown to induce a hypertrophic response in rodents [113, 114] [112]. In our study, however, we were unable to detect obvious cardiomyocyte hypertrophy induced by the miRNA, especially since all pigs were infarcted and thus subject to hypertrophy compensatory to loss of cardiac function. Certainly no additive hypertrophic effects of the miRNA were observed, since, on the contrary, preservation of cardiac function instead reduced hypertrophy in the miR-199a-treated animals, as concluded from the analysis of cardiomyocyte cross-

sectional area. It is also possible that the target genes related to hypertrophic response of the 5p strand might not be conserved in pigs.

In accordance with the favourable tissue remodelling promoted by miR-199a, the ANP and BNP peptides measured in patients' sera as diagnostic and prognostic markers of heart failure [185], were down-regulated in the treated animals at all the time points analysed. Pathological cardiac hypertrophy and heart failure are also characterized by a reduction in the expression of Myh6 (alpha), the myosin isoform that hydrolyses ATP three times faster than Myh7 (beta) [186]. Consistently, in our experimental settings we observed that AAV6-Control animals had a reduced Myh6/ Myh7 ratio compared to sham-treated animals, while AAV6-miR-199a injected pigs showed increased levels Myh6, consistent with improved contractility and reduced myocardial damage.

In our previous work, we demonstrated that miR-199a directly targets the *Homer1*, *Hopx* and *Clic5* mRNAs in mice [82] and that the simultaneous silencing of these genes increases neonatal mouse cardiomyocyte proliferation as strong as the microRNA itself (data not shown). Unfortunately, the microRNA target site is not conserved in the 3-UTRs of these genes' mRNAs in pigs, suggesting that miR-199a may exert its function by targeting other proteins in the same pathways, or different proteins that have the same function, or the same genes but through target sites in mRNA regions other than the 3'UTR.

In a parallel study, we also identified *Cofilin2*, *Taok1* and β*-trc* as additional miR-199a direct targets in rodents. The downregulation of these proteins activates YAP, the final effector of the Hippo pathway, which, once in the nucleus, promotes the transcription of genes necessary cell proliferation [187]. In these cases, the microRNA target sites are conserved in the pig mRNA 3-UTRs for all the three genes and, we consistently could measure downregulation of Taok1 and β-trc (but not Cofilin2), mRNAs in AAV6-miR-199a treated pigs (data not shown).

A most remarkable finding at both 12 and 30 days after AAV6-miR-199a administration to infarcted pig, was the appearance, in the infarct border zone, of a remarkable number of GATA4-positive cells, suggestive of cardiomyocyte de-differentiation. This transcription factor regulates the expression of genes involved in embryogenesis and myocardial differentiation. In adult and neonatal cardiomyocytes the factor is present and active in the nucleus; however, during embryonic life, it can also be found in the cytoplasm [173]. Surprisingly, after MI in pig myocardium, a significant number of

cardiomyocytes showed marked cytoplasmic localization of GATA4. This observation is consistent with the possibility that the expression of miR-199a, along with proliferation, might also induce de-differentiation of cardiomyocytes, a process known to accompany cardiac regeneration in zebrafish [172].

To the best of our knowledge, this is the first proof of cardiac regeneration and consequent improvement in cardiac function obtained by the stimulation of the endogenous capacity of cardiomyocyte to proliferate after damage.

4.3. Safety issues related to prolonged miR-199a expression using AAV vectors

To evaluate the long-term effect of miR-199a constitutive expression, we include in our protocol a number of animals which were left alive after the 1 month time point. Despite the progressively smaller scar size and the improved heart function observed by cMRI in one of the animals analysed at 60 days after MI and treatment, 6 out of 7 animals treated with AAV6-miR-199a died between days 45 and 55 of sudden cardiac death. Three of these animals had implanted ECG mini-recorders and, in one of them, we were able to record the episode of ventricular fibrillation that caused its death.

The real reason for the ventricular fibrillation, but more in general, for sudden cardiac death in our treated animals is still unknown and it will be the object of further investigation. In particular, a priority for investigation will be the role of the potential downregulation of Ryr2, a predicted target of miR-199a-3p, as well as that of other ion channel proteins, especially those involved in ion channel genetic dysfunction characterized by ventricular fibrillation and sudden death. In addition, we will also explore the presence of a dysfunction of Purkinje fibers, which allow fast propagation of action potential and might be the substrate for arrhythmogenic events. The pro-proliferative effect of miR-199a on Purkinje fibers has been excluded (data not shown), but it is not known yet whether miR-199a could interfere on Purkinje fiber function and action potential propagation. Of potential interest, however, death in the analysed animals was almost synchronized and required over 1.5 months to occur, an observation that is more consistent with the expansion of a pathological cell population, eventually reaching a critical threshold and exerting an arrhythmogenic effect, rather than with the direct effect of the miRNA on cardiac conduction, which would have been expected to occur at earlier time points.

Histological examination of pig heart tissues indicated that, in two animals which died of sudden death and the one which sacrificed at 60 days, there were small clusters of cells infiltrating the cardiac tissue. These cells were negative for CD45 and CD34, thus excluding their lymphoid and myeloid origin as well as their identity as hematopoietic blast or activated endothelial cells. The high positivity in immunohistochemistry for Ki-67, revealed that these cells had a high proliferation rate. These cell clusters were negative for differentiated markers of muscle cells, including desmin and HHF35, while expressed markers of undifferentiated cells of muscle origin, among which myogenin, caldesmon and GATA4. Thus, these cells appear to possess the phenotypic identity of myoblastic cells at the early stages of differentiation. Are these highly proliferating cells arising from the prolonged and unregulated miR-199a expression? Most likely yes, however not necessarily as a direct product of cardiomyocyte transduction, unless it will be formally demonstrated that these cells harbour integrated AAV vectors – integration would appear to be a necessary event to explain maintenance of the virus along successive cell divisions. Alternatively, these cells might arise as the effect of alterations in the microenvironment by cytokines and growth factors produced by cardiomyocytes primarily transduced with AAV9-miR-199a.

Can the infiltrating cells be considered as cancer cells? This is a difficult question to answer, since, to the best of our knowledge, no human cardiac tumors bears a phenotype resembling the cell clusters we have observed in these animals, neither we have attempted to culture these cells ex vivo and prove their tumorigenic potential. Whatever their origin and derivation, the expansion of infiltrating cell clusters in the heart of animals treated with AAV9-miR-199a might well explain the onset of the fatal arrhythmias that caused the deaths of these animals.

In short, our study overall shows that AAV6-miR-199a delivery improves functional parameters and reduces scar size in juvenile pigs by stimulating cardiomyocyte de-differentiation and cell cycle re-entry. Conversely, its long-term expression causes sudden cardiac death. It remains to be understood how the two events are linked. At least two possibilities can be envisaged. First, proliferation and de-differentiation are the results of the same mechanism of action. Similar to zebrafish [188], cardiomyocytes re-entering the cell cycle re-express markers of embryonic development. In this view, pathology becomes evidence once expression of the de-differentiating and pro-proliferating agent (miR-199a in our case) becomes excessive or too prolonged. An alternative possibility is that the beneficial effect of AAV6-miR-199a in the short term is

due to the prevalent action of miR-199-3p, which has beneficial, pro-proliferative effects in rodents and human cells. At longer time points, however, the effects of miR-199-5p might instead prevail. This miRNA, indeed, has been shown to exert deleterious activity on cardiac function (see Introduction).

Whichever is the mechanism involved, it appears clear that a therapy based on the constitutive expression of miR-199a after AAV-mediated gene delivery is not feasible for human translation. However, whichever the mechanisms involved, it also appears clear that problems in either cases could be overcome by the use of synthetic miR-199a-3p mimics, which would provide strand specificity as well as ensure shorter time effects.

4.4 Single injection of miR-199a-3p mimics with various chemical modifications improves cardiac recovery after myocardial infarction in mice

MicroRNA mimics are small (miR-199a mimic is around 13 590 Daltons), but highly charged molecules (44 negative charges in the case of miR-199a mimic) unable to spontaneously pass cell membranes. Therefore, the development of a therapy using miRNA mimics requires conjugation of these molecules with a delivery carrier, the most effective of which, in the case of negatively charged nucleic acids, are cationic lipids. In addition to actively mediating tissue transfection, these agents also can effectively shield nucleic acids from endonucleases present in the extracellular environment, thereby enhancing their persistence. Thus, in this work we tested different commercially available cationic lipid preparations for their ability of delivering microRNA mimics in the heart, with or without myocardial infarction.

Four different cationic lipids were tested in vivo, upon direct intracardiac injection; among these, the best results were obtained using those originally designed for *in vitro* experimentation, such as Lipofectamine 2000 and Lipofectamine RNAiMax, whilst Invivofectamine, proposed by the manufacturers' for *in vivo* delivery, showed significantly lower efficiency. When a complex between miR-199a-3p and Lipofectamine RNAiMax was tested in vivo, we found that a single intracardiac injection immediately after MI was sufficient to improve cardiac function, assessed by echocardiography up to two months, and to reduce scar size. Additionally, we also observed that the injected miR-199a-3p mimic levels in the LV anterior wall were detectable by qRT-PCR up to 12 days after injection.

In evaluating these findings, it appears important to observe that, different from AAV6 (pigs) or AAV9 (mice) vectors, which both display selective transduction of cardiomyocytes, cationic-lipid-mediated mimic delivery affect all cell types in the heart (in particular, cardiac fibroblasts and endothelial cells in addition to cardiomyocytes). Thus, we can not formally exclude that the beneficial effects of miR-199a-3p mimic we observed might also depend, at least in part, on the effect exerted in other cell types. Despite cardiomyocytes represent less than 40% in the heart, however, their volume occupies over 90% of the organ. In addition, invaginations of the cardiomyocyte sarcolemma to form T-tubules further extends the membrane surface that is available to uptake exogenously administered lipoplexes. Thus, it would not appear unreasonable to assert that most of the transfected mimics is taken up by cardiomyocytes. Further experiments can be designed to address the issue of differential transfection of the various cardiac cell types specifically.

A limitation in the use of lipid-based delivery systems is the potential unwanted immune response caused by cell membrane disruption that occurs because of the many positive charges of the exogenous lipids [189]. Other delivery agents are available that might overcome this limitation, such as dendrimers, polymers (polyethylenimine or polylactide-co-glycolide), or polysaccharides as chitosan, which are now under extensive investigation. Despite the above-mentioned limitations, however, to date lipofectamine-based reagents remain the most efficient and the most used delivery system, both in vitro and vivo.

Our experiments with miR-199a-3p show that, once delivered to the heart, this mimic is maintained in an active form up to 12 days after injection and that this time is sufficient, for the miRNA, to exert a beneficial effect. Can effectiveness be increased by modifying the chemical structure of the miRNA in order to extend its half life? We tested 4 different chemical modifications of the synthetic mimic provided by two commercial vendors. Two of these mimics increased neonatal rat cardiomyocyte proliferation in vitro compared to the original mimic used in all other experiements. One of newly modified mimics, in particular, once injected into the LV anterior wall in infarcted mice was still present as long as 21 days after surgery. Of interest, however, efficacy of this modified mimic in healing the infarcted myocardium did not appear superior to that of the original molecule. This finding might indicate that the effect of miRNA therapy is exerted in the first few days after infarction, and that prolonged expression is not effective. This conclusion is in line with the observation that, in pigs, no further

cardiomyocyte proliferation was observed at 1 month after miR-199a delivery, even if expression of this miRNA from AAV vectors continued to be robust at this time point. Elucidation of the molecular mechanisms determining response of cardiomyocytes to the effect of miR-199a-3p will help explaining the reasons why cell response to this miRNA becomes exhausted over time.

Figure 1

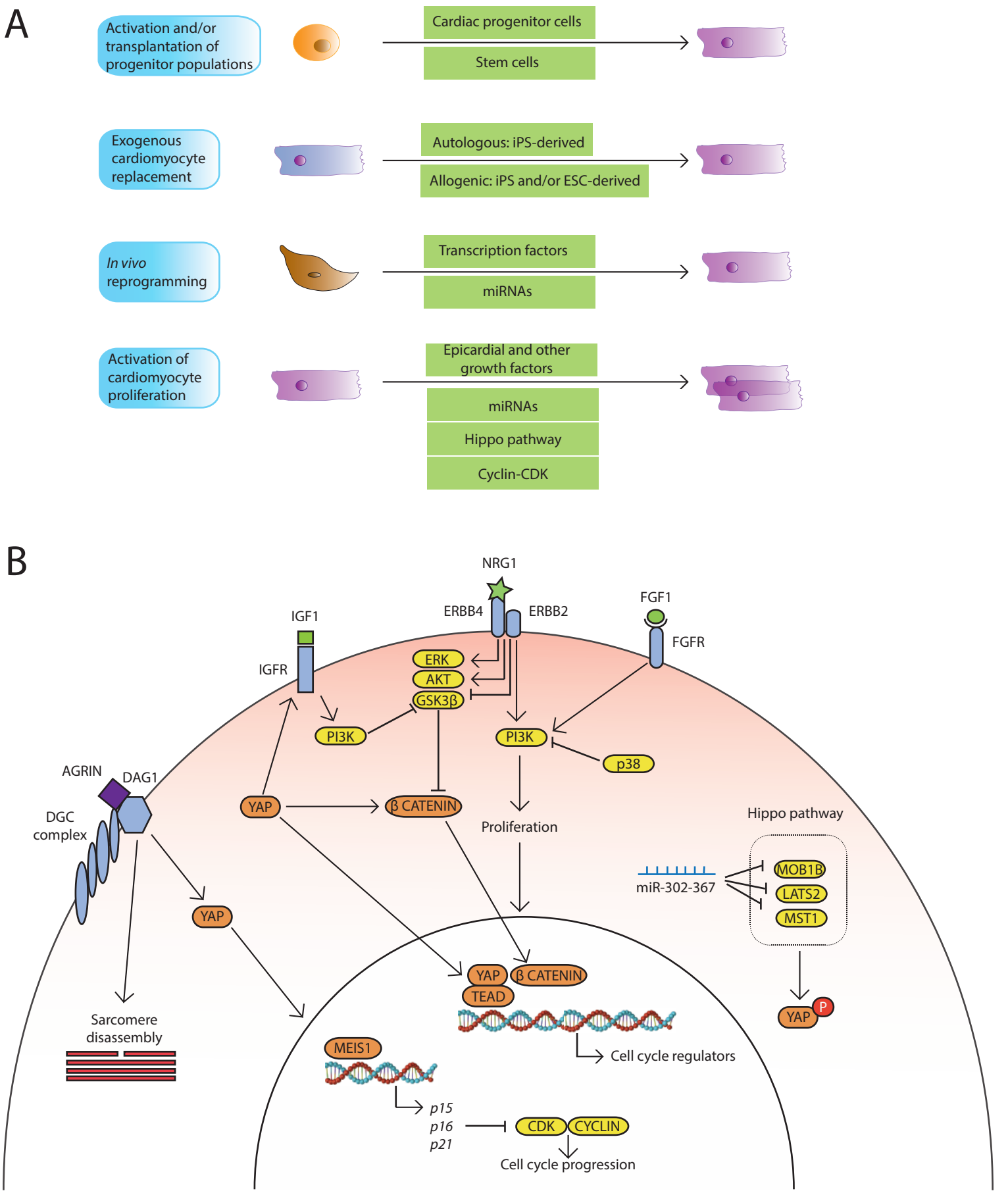
A
Activation and/or transplantation of progenitor populations
Cardiac progenitor cells
Stem cells
Exogenous cardiomyocyte replacement
Autologous: iPS-derived
Allogenic: iPS and/or ESC-derived
In vivo reprogramming
Transcription factors
miRNAs
Activation of cardiomyocyte proliferation
Epicardial and other growth factors
miRNAs
Hippo pathway
Cyclin-CDK
B
NRG1
ERBB4
ERBB2
FGF1
FGFR
IGF1
IGFR
ERK
AKT
GSK3β
PI3K
PI3K
p38
AGRIN
DAG1
DGC complex
YAP
β CATENIN
Proliferation
Hippo pathway
miR-302-367
MOB1B
LATS2
MST1
YAP
P
YAP
β CATENIN
TEAD
Cell cycle regulators
Sarcomere disassembly
MEIS1
p15
p16
p21
CDK
CYCLIN
Cell cycle progression

Figure 2

A

Human miR-199a-1 precursor

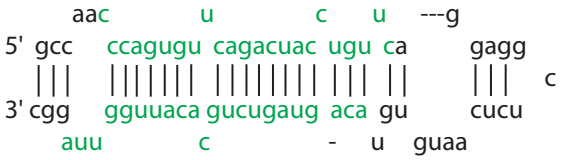

Human miR-199a-2 precursor

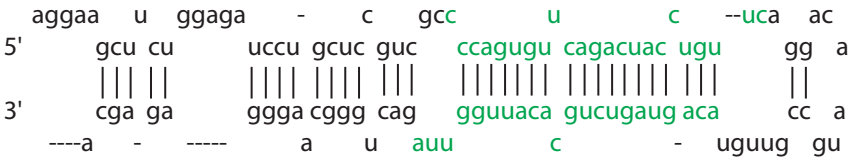

B

	miR-199a-5p	**miR-199a-3p**
Homo sapiens	cccaguguucagacuaccuguuc	acaguagucugcacauugguua
Mus musculus	cccaguguucagacuaccuguuc	acaguagucugcacauugguua
Rattus norvegicus	cccaguguucagacuaccuguuc	acaguagucugcacauugguua
Sus scrofa	cccaguguucagacuaccuguuc	acaguagucugcacauugguua

C

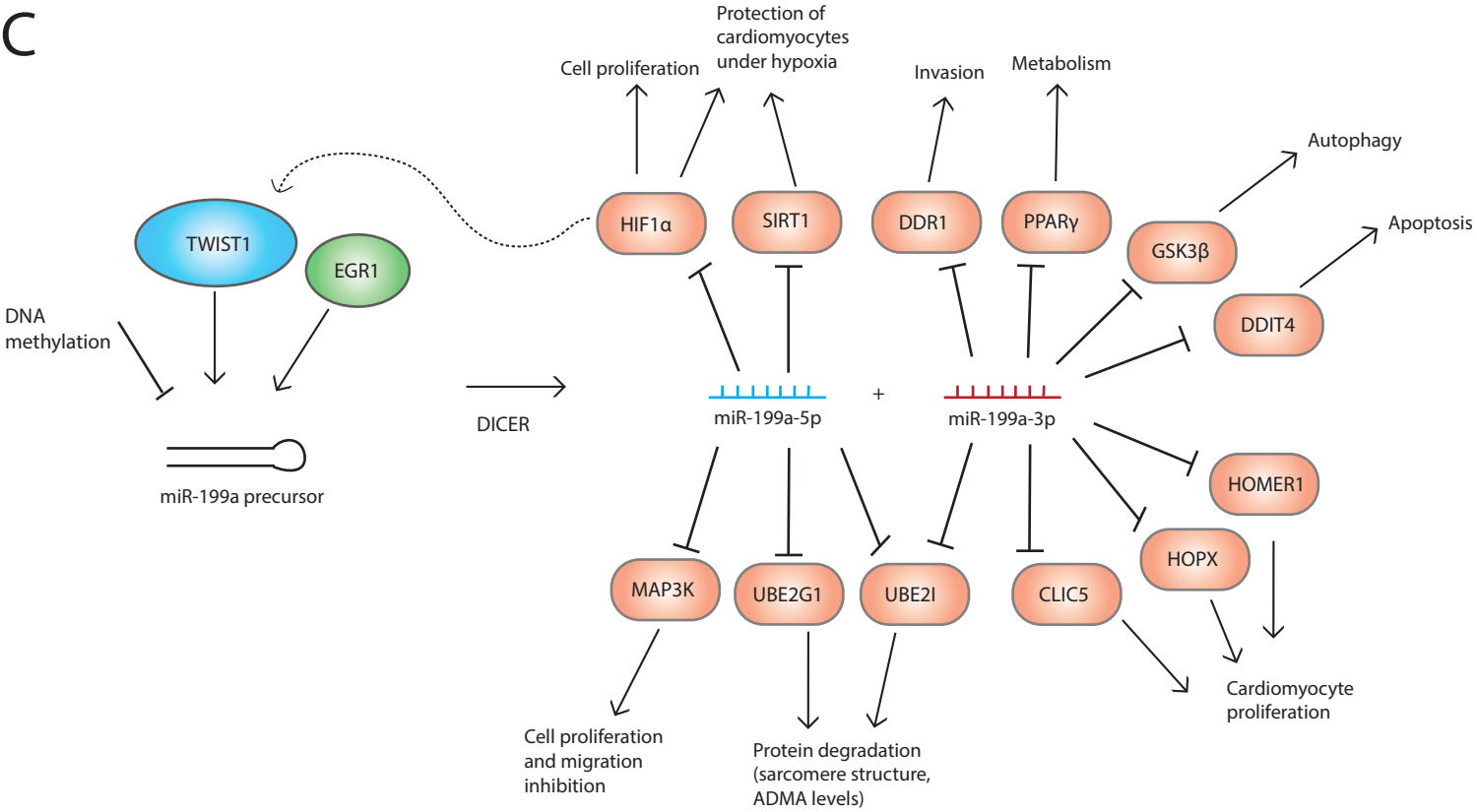

Figure 3

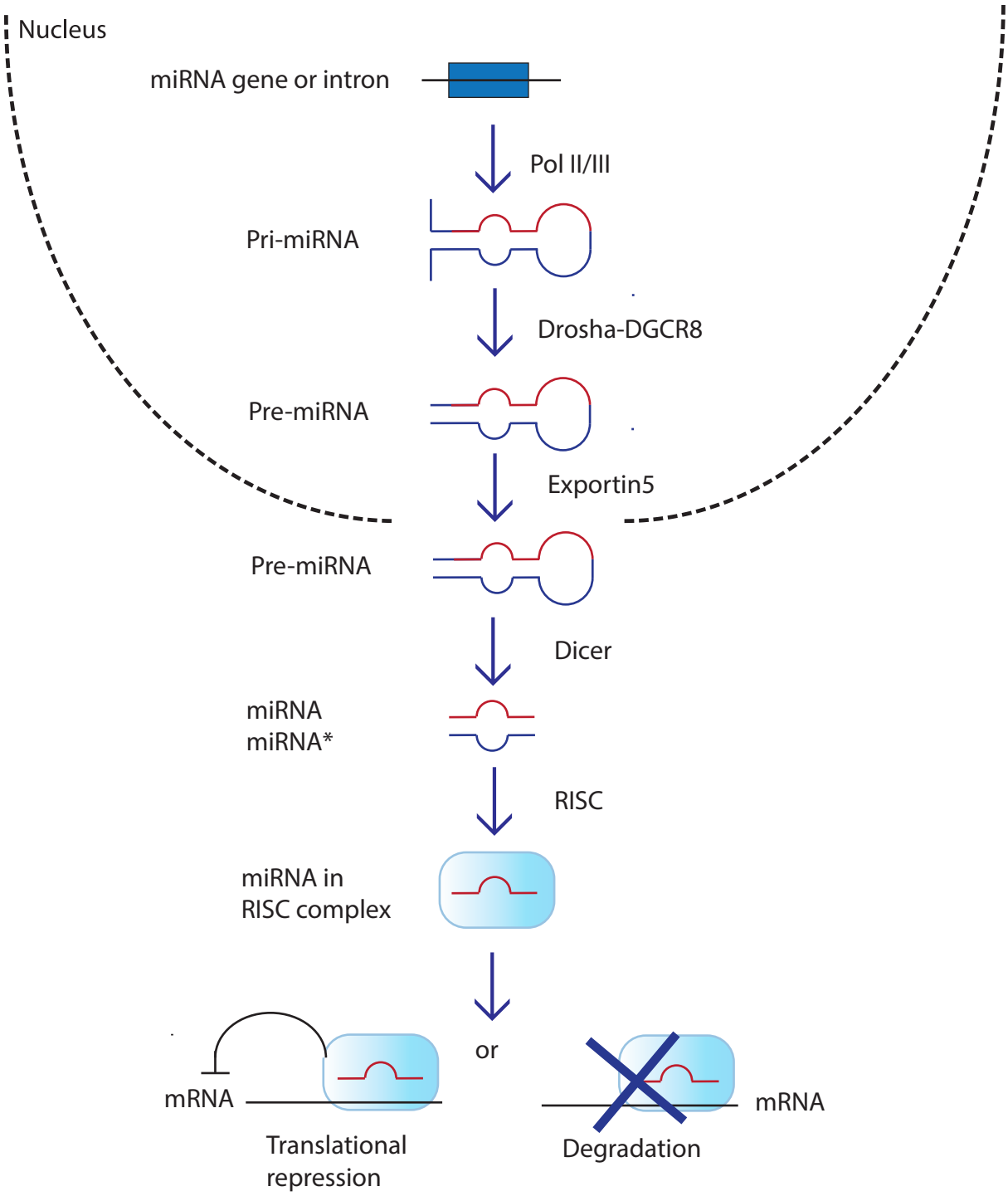
Nucleus
miRNA gene or intron
Pol II/III
Pri-miRNA
Drosha-DGCR8
Pre-miRNA
Exportin5
Pre-miRNA
Dicer
miRNA
miRNA*
RISC
miRNA in
RISC complex
or
mRNA
Translational
repression
Degradation
mRNA

Figure 4

miR-18a-3p

Homo sapiens	ACUGCCCUAAGUGCUCCUUCUGG	hsa-miR-18a-3p MIMAT0002891
Mus musculus	ACUGCCCUAAGUGCUCCUUCUG	mmu-miR-18a-3p MIMAT0004626
Rattus norvegicus	ACUGCCCUAAGUGCUCCUUCU	rno-miR-18a-3p MIMAT0017095
Sus scrofa	UAAGGUGCAUCUAGUGCAGAUA	

miR-30e-3p

Homo sapiens	CUUUCAGUCGGAUGUUUACAGC	hsa-miR-30e-3p MIMAT0000693
Mus musculus	CUUUCAGUCGGAUGUUUACAGC	mmu-miR-30e-3p MIMAT0000249
Rattus norvegicus	CUUUCAGUCGGAUGUUUACAGC	rno-miR-30e-3p MIMAT0004720
Sus scrofa	CUUUCAGUCGGAUGUUUACAGC	ssc-miR-30e-3p MIMAT0013873

miR-33b-3p

Homo sapiens	CAGUGCCUCGGCAGUGCAGCCC	hsa-miR-33b-3p MIMAT0004811
Mus musculus	CAAUGUUUCCACAGUGCAUCAC	mmu-miR-33-3p MIMAT0004666
Rattus norvegicus	CAAUGUUUCCACAGUGCAUCA	rno-miR-33-3p MIMAT0017104
Sus scrofa	absent	

miR-302d-3p

Homo sapiens	UAAGUGCUUCCAUGUUUGAGUGU	hsa-miR-302d-3p MIMAT0000718
Mus musculus	UAAGUGCUUCCAUGUUUGAGUGU	
Rattus norvegicus	absent	
Sus scrofa	absent	

miR-199a-3p

Homo sapiens	ACAGUAGUCUGCACAUUGGUUA	hsa-miR-199a-3p MIMAT0000232
Mus musculus	ACAGUAGUCUGCACAUUGGUUA	mmu-miR-199a-3p MIMAT0000230
Rattus norvegicus	ACAGUAGUCUGCACAUUGGUUA	rno-miR-199a-3p MIMAT0004738
Sus scrofa	ACAGUAGUCUGCACAUUGGUUA	ssc-miR-199a-3p MIMAT0013875

miR-590-3p

Homo sapiens	UAAUUUUAUGUAUAAGCUAGU	hsa-miR-590-3p MIMAT0004801
Mus musculus	UAAUUUUAUGUAUAAGCUAGU	mmu-miR-590-3p MIMAT0004896
Rattus norvegicus	absent	
Sus scrofa	absent	

miR-1248

Homo sapiens	ACCUUCUUGUAUAAGCACUGUGCUAAA	hsa-miR-1248 MIMAT0005900
Mus musculus	absent	
Rattus norvegicus	absent	
Sus scrofa	absent	

miR-1825

Homo sapiens	UCCAGUGCCCUCCUCUCC	hsa-miR-1825 MIMAT0006765
Mus musculus	absent	
Rattus norvegicus	absent	
Sus scrofa	absent	

Figure 5

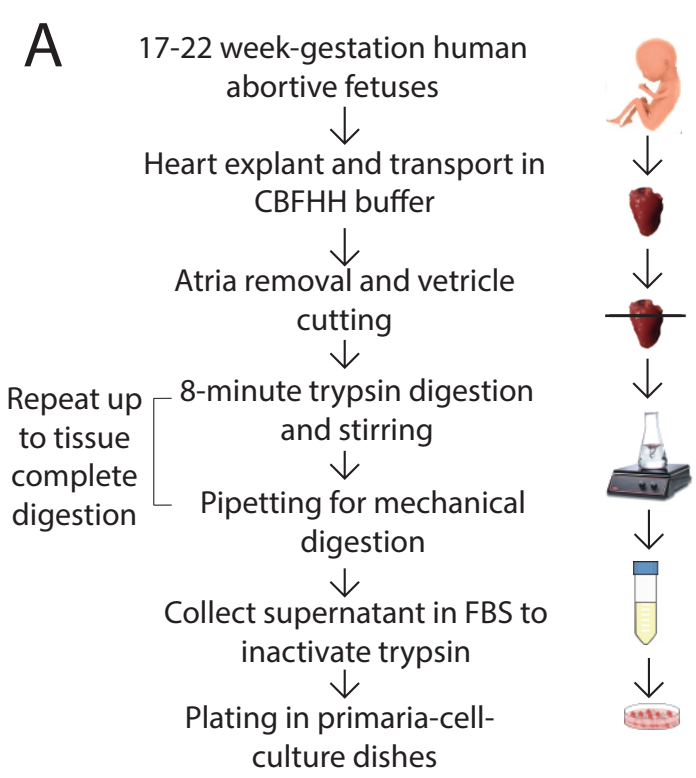
A
17-22 week-gestation human abortive fetuses
Heart explant and transport in CBFHH buffer
Atria removal and vetricle cutting
Repeat up to tissue complete digestion
8-minute trypsin digestion and stirring
Pipetting for mechanical digestion
Collect supernatant in FBS to inactivate trypsin
Plating in primaria-cell-culture dishes

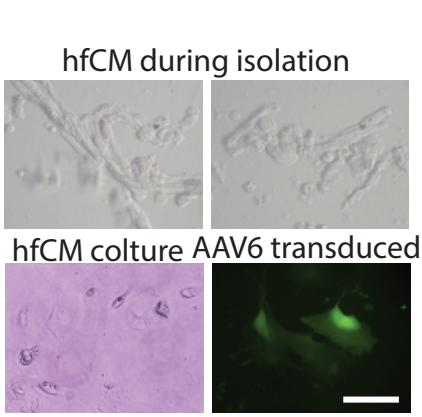
B
hfCM during isolation
hfCM colture
AAV6 transduced

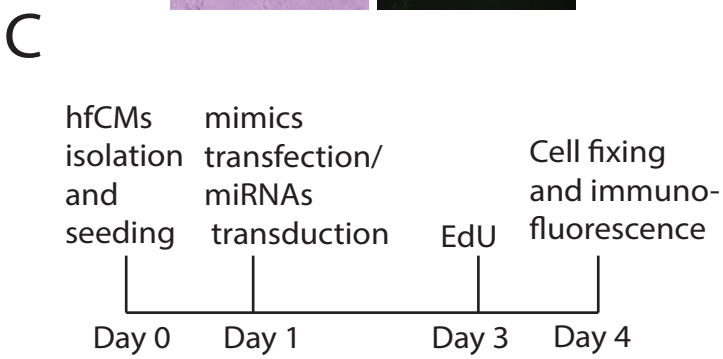
C
hfCMs isolation and seeding
mimics transfection/ miRNAs transduction
EdU
Cell fixing and immuno-fluorescence
Day 0
Day 1
Day 3
Day 4

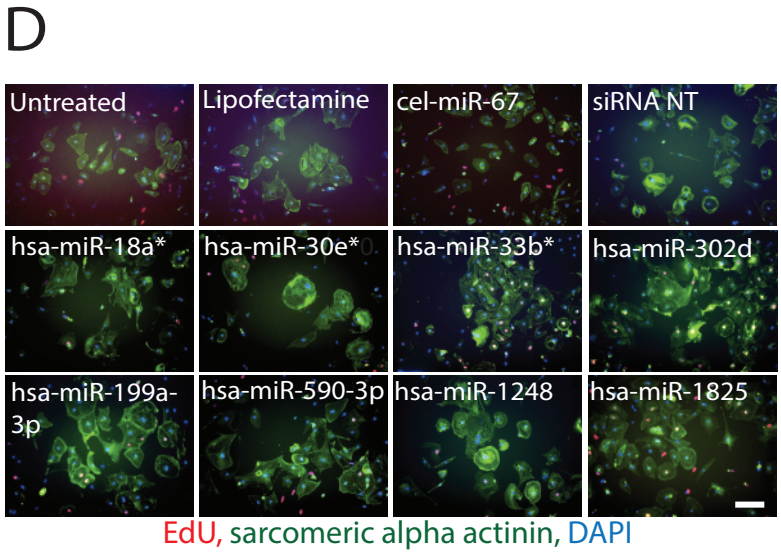
D
Untreated
Lipofectamine
cel-miR-67
siRNA NT
hsa-miR-18a*
hsa-miR-30e*
hsa-miR-33b*
hsa-miR-302d
hsa-miR-199a-3p
hsa-miR-590-3p
hsa-miR-1248
hsa-miR-1825
EdU, sarcomeric alpha actinin, DAPI

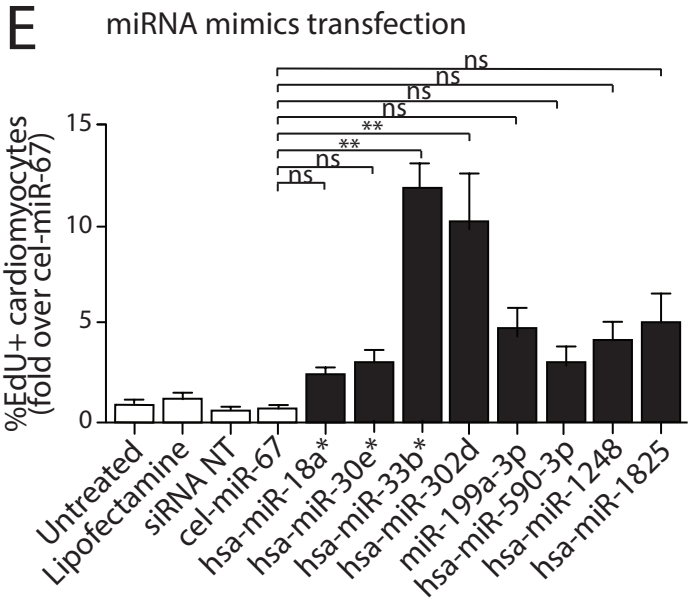
E
miRNA mimics transfection
%EdU+ cardiomyocytes (fold over cel-miR-67)
0
5
10
15
ns
**
Untreated
Lipofectamine
siRNA NT
cel-miR-67
hsa-miR-18a*
hsa-miR-30e*
hsa-miR-33b*
hsa-miR-302d
miR-199a-3p
hsa-miR-590-3p
hsa-miR-1248
hsa-miR-1825

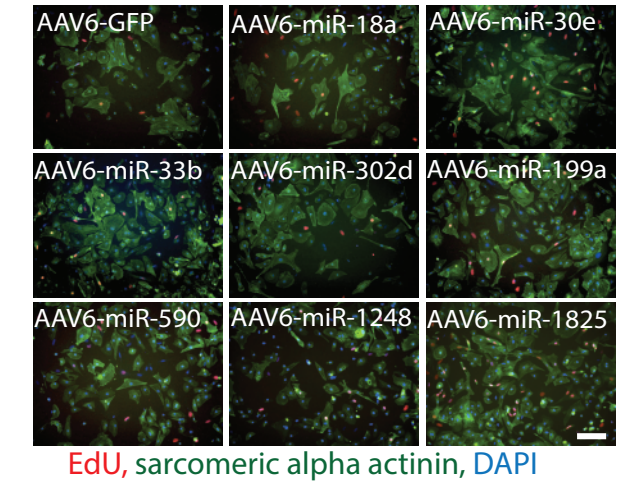
F
AAV6-GFP
AAV6-miR-18a
AAV6-miR-30e
AAV6-miR-33b
AAV6-miR-302d
AAV6-miR-199a
AAV6-miR-590
AAV6-miR-1248
AAV6-miR-1825
EdU, sarcomeric alpha actinin, DAPI

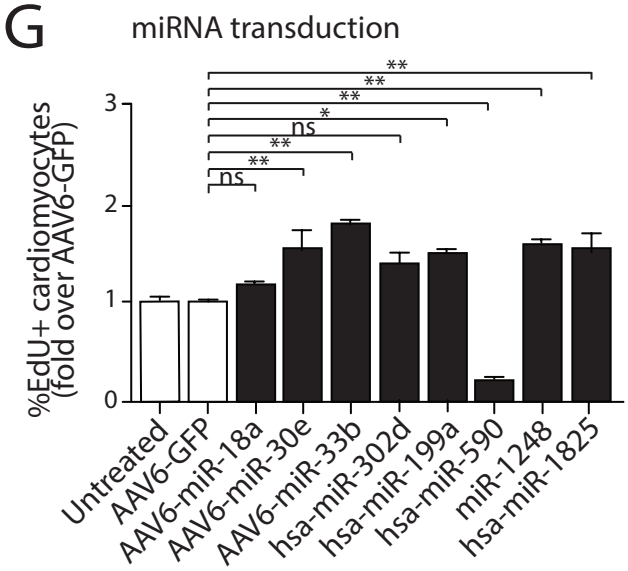
G
miRNA transduction
%EdU+ cardiomyocytes (fold over AAV6-GFP)
0
1
2
3
**
*
ns
Untreated
AAV6-GFP
AAV6-miR-18a
AAV6-miR-30e
AAV6-miR-33b
AAV6-miR-302d
hsa-miR-199a
hsa-miR-590
miR-1248
hsa-miR-1825

Figure 6

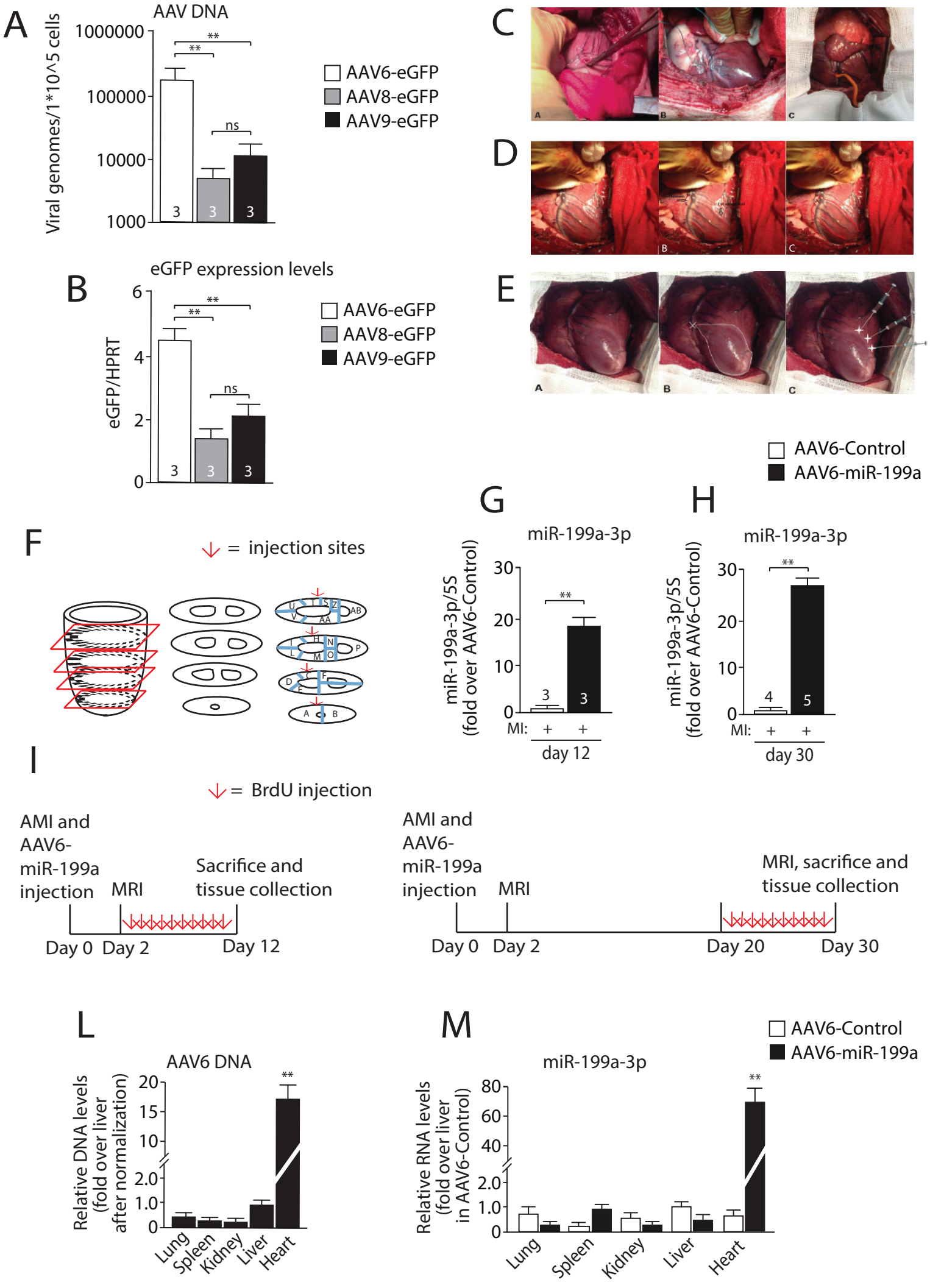
A
AAV DNA
Viral genomes/1*10^5 cells
1000000
100000
10000
1000
**
**
ns
3
3
3
AAV6-eGFP
AAV8-eGFP
AAV9-eGFP
B
eGFP expression levels
eGFP/HPRT
6
4
2
0
**
**
ns
3
3
3
AAV6-eGFP
AAV8-eGFP
AAV9-eGFP
C
D
E
A
B
C
AAV6-Control
AAV6-miR-199a
F
= injection sites
G
miR-199a-3p
miR-199a-3p/5S
(fold over AAV6-Control)
30
20
10
0
**
3
3
MI: + +
day 12
H
miR-199a-3p
miR-199a-3p/5S
(fold over AAV6-Control)
30
20
10
0
**
4
5
MI: + +
day 30
I
= BrdU injection
AMI and
AAV6-
miR-199a
injection
MRI
Sacrifice and
tissue collection
Day 0
Day 2
Day 12
AMI and
AAV6-
miR-199a
injection
MRI
MRI, sacrifice and
tissue collection
Day 0
Day 2
Day 20
Day 30
L
AAV6 DNA
Relative DNA levels
(fold over liver
after normalization)
20
15
10
2.0
1.0
0
**
Lung
Spleen
Kidney
Liver
Heart
M
AAV6-Control
AAV6-miR-199a
miR-199a-3p
Relative RNA levels
(fold over liver
in AAV6-Control)
80
60
40
2.0
1.0
0
**
Lung
Spleen
Kidney
Liver
Heart

Figure 7

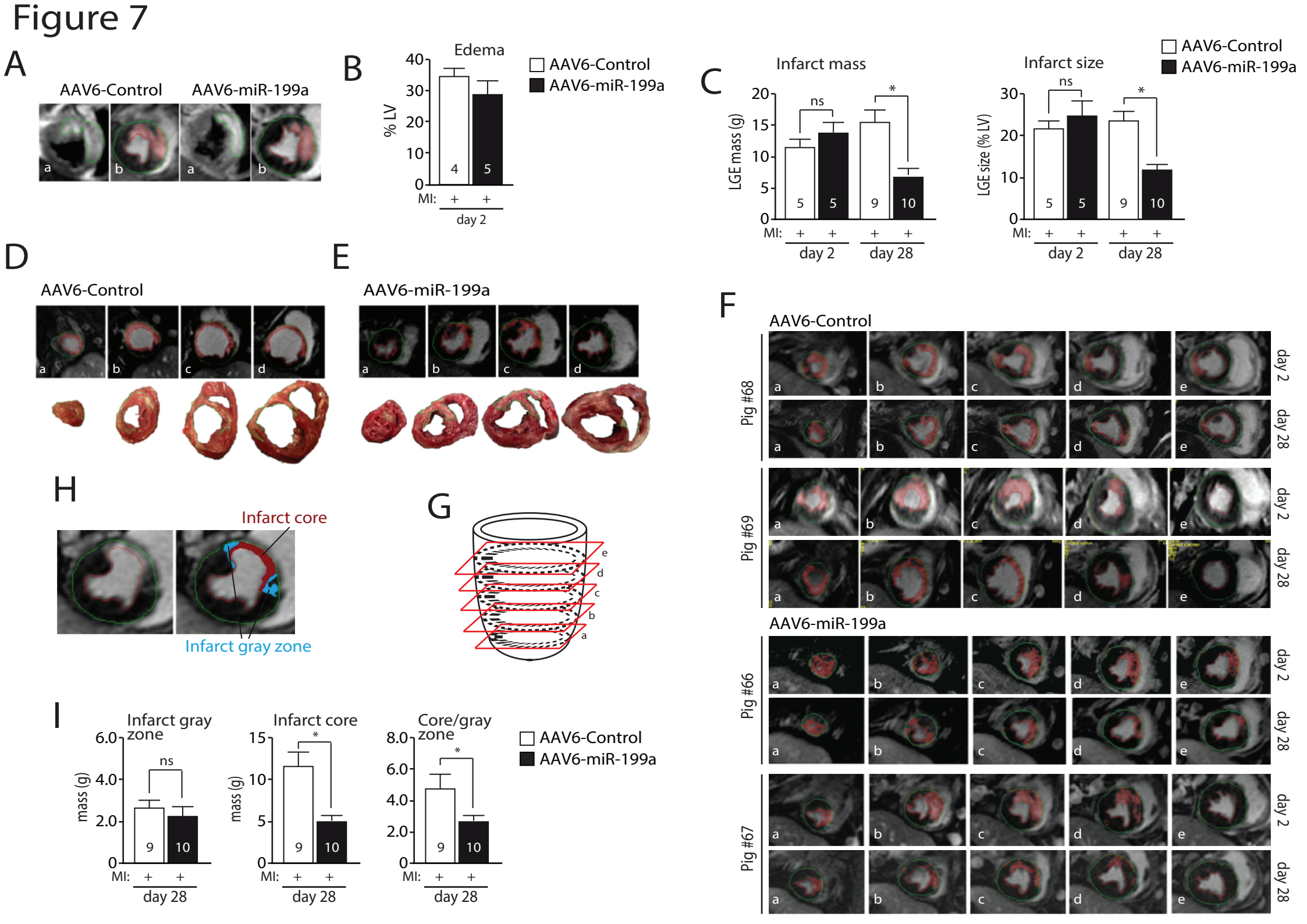
A
AAV6-Control
AAV6-miR-199a
a
b
a
b
B
Edema
% LV
40
30
20
10
0
4
5
MI: + +
day 2
AAV6-Control
AAV6-miR-199a
C
Infarct mass
LGE mass (g)
20
15
10
5
0
ns
*
5
5
9
10
MI: + + + +
day 2
day 28
Infarct size
LGE size (% LV)
30
20
10
0
ns
*
5
5
9
10
MI: + + + +
day 2
day 28
AAV6-Control
AAV6-miR-199a
D
AAV6-Control
a
b
c
d
E
AAV6-miR-199a
a
b
c
d
F
AAV6-Control
Pig #68
Pig #69
AAV6-miR-199a
Pig #66
Pig #67
a
b
c
d
e
day 2
day 28
H
Infarct core
Infarct gray zone
G
e
d
c
b
a
I
Infarct gray zone
mass (g)
6.0
4.0
2.0
0
ns
9
10
MI: + +
day 28
Infarct core
mass (g)
15
10
5
0
*
9
10
MI: + +
day 28
Core/gray zone
8.0
6.0
4.0
2.0
0
*
9
10
MI: + +
day 28
AAV6-Control
AAV6-miR-199a

Figure 8

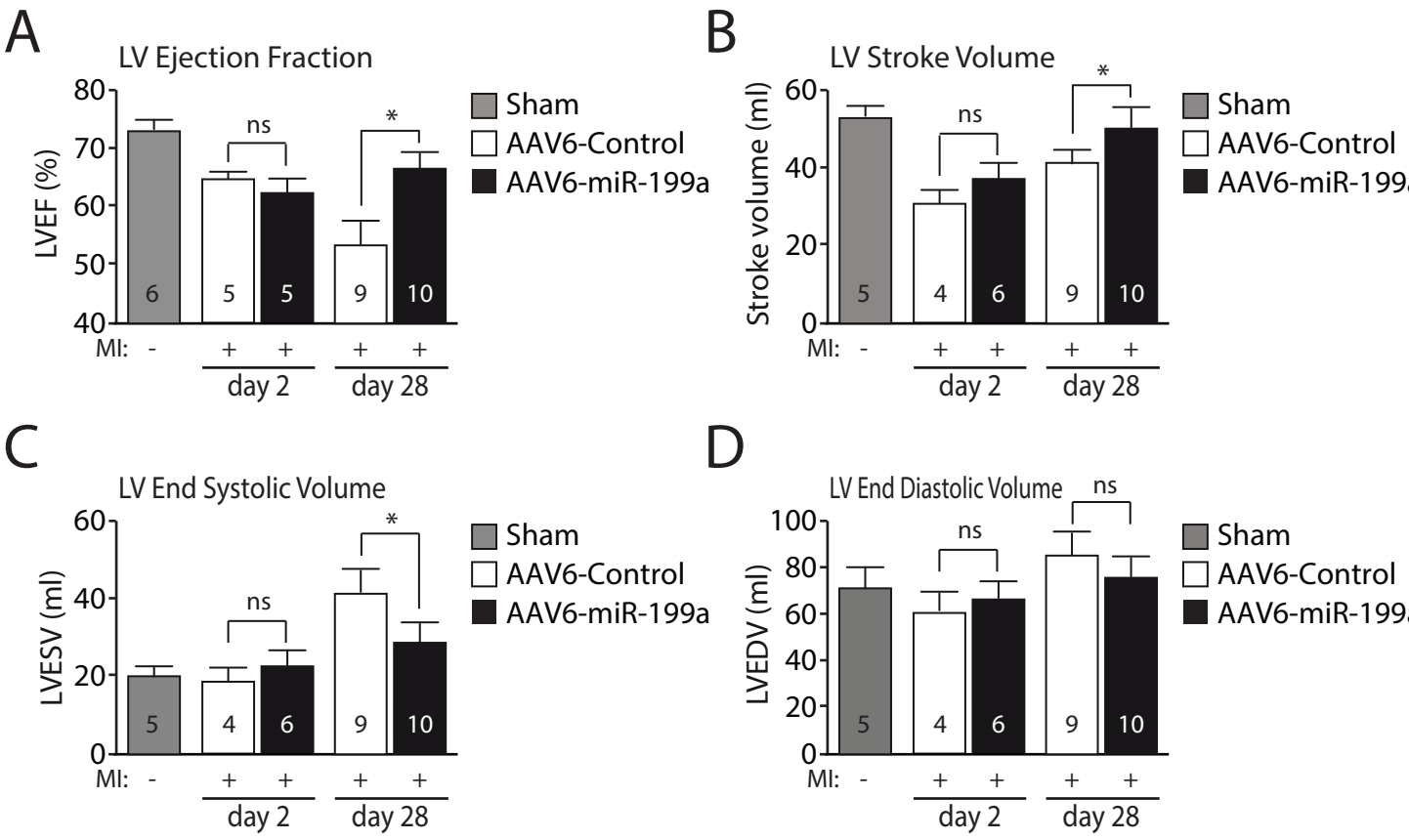
A
LV Ejection Fraction
LVEF (%)
80
70
60
50
40
ns
*
6
5
5
9
10
MI: - + + + +
day 2
day 28
Sham
AAV6-Control
AAV6-miR-199a
B
LV Stroke Volume
Stroke volume (ml)
60
40
20
0
ns
*
5
4
6
9
10
MI: - + + + +
day 2
day 28
Sham
AAV6-Control
AAV6-miR-199a
C
LV End Systolic Volume
LVESV (ml)
60
40
20
0
ns
*
5
4
6
9
10
MI: - + + + +
day 2
day 28
Sham
AAV6-Control
AAV6-miR-199a
D
LV End Diastolic Volume
LVEDV (ml)
100
80
60
40
20
0
ns
ns
5
4
6
9
10
MI: - + + + +
day 2
day 28
Sham
AAV6-Control
AAV6-miR-199a

Figure 9

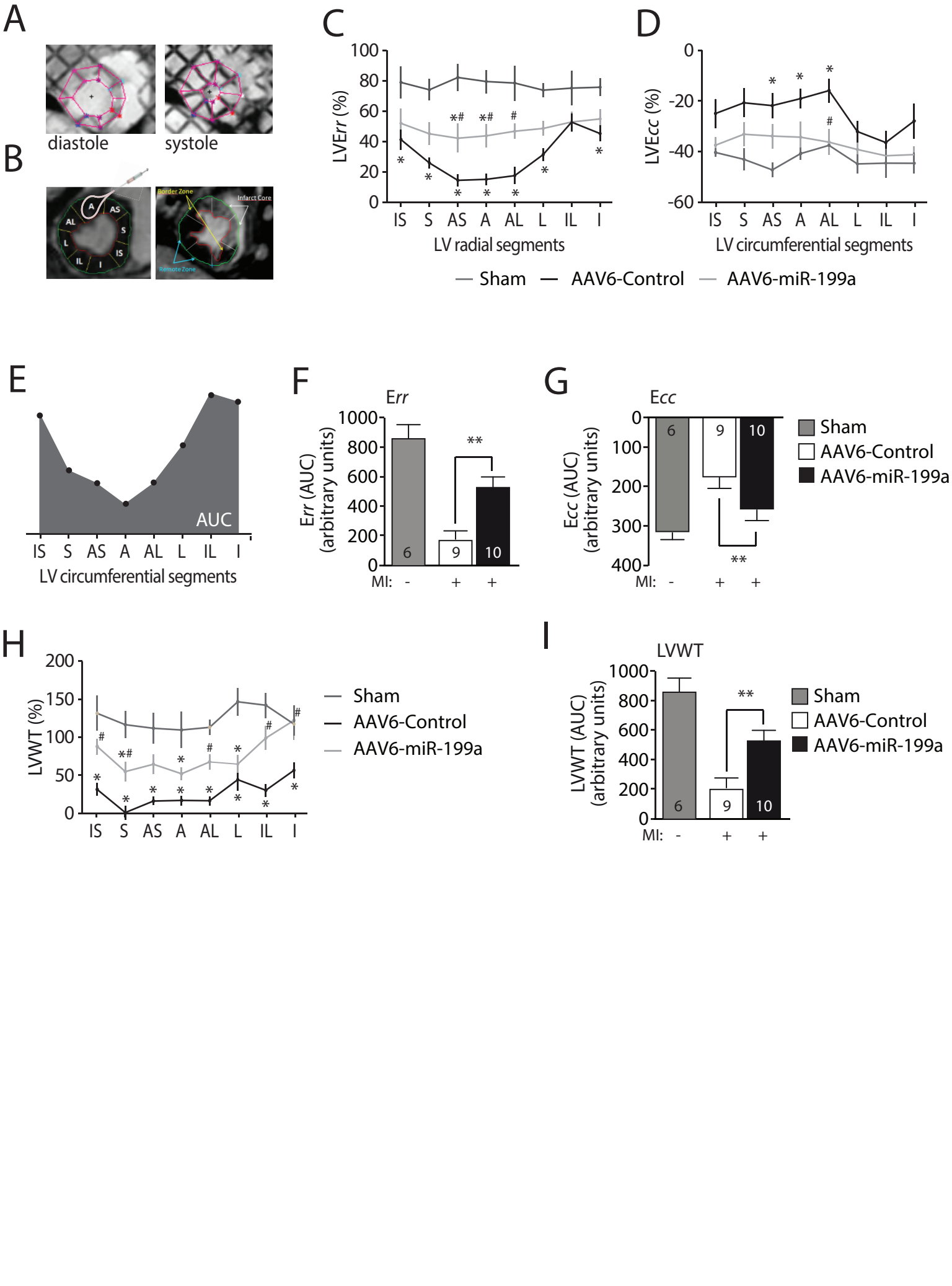
A
diastole
systole
B
Border Zone
Infarct Core
Remote Zone
A
AS
S
IS
I
IL
L
AL
C
LVErr (%)
100
80
60
40
20
0
IS S AS A AL L IL I
LV radial segments
D
LVEcc (%)
0
-20
-40
-60
IS S AS A AL L IL I
LV circumferential segments
Sham
AAV6-Control
AAV6-miR-199a
E
AUC
IS S AS A AL L IL I
LV circumferential segments
F
Err
Err (AUC) (arbitrary units)
1000
800
600
400
200
0
**
6
9
10
MI: - + +
G
Ecc
Ecc (AUC) (arbitrary units)
0
100
200
300
400
6
9
10
**
MI: - + +
Sham
AAV6-Control
AAV6-miR-199a
H
LVWT (%)
200
150
100
50
0
IS S AS A AL L IL I
Sham
AAV6-Control
AAV6-miR-199a
I
LVWT
LVWT (AUC) (arbitrary units)
1000
800
600
400
200
0
**
6
9
10
MI: - + +
Sham
AAV6-Control
AAV6-miR-199a

Figure 10

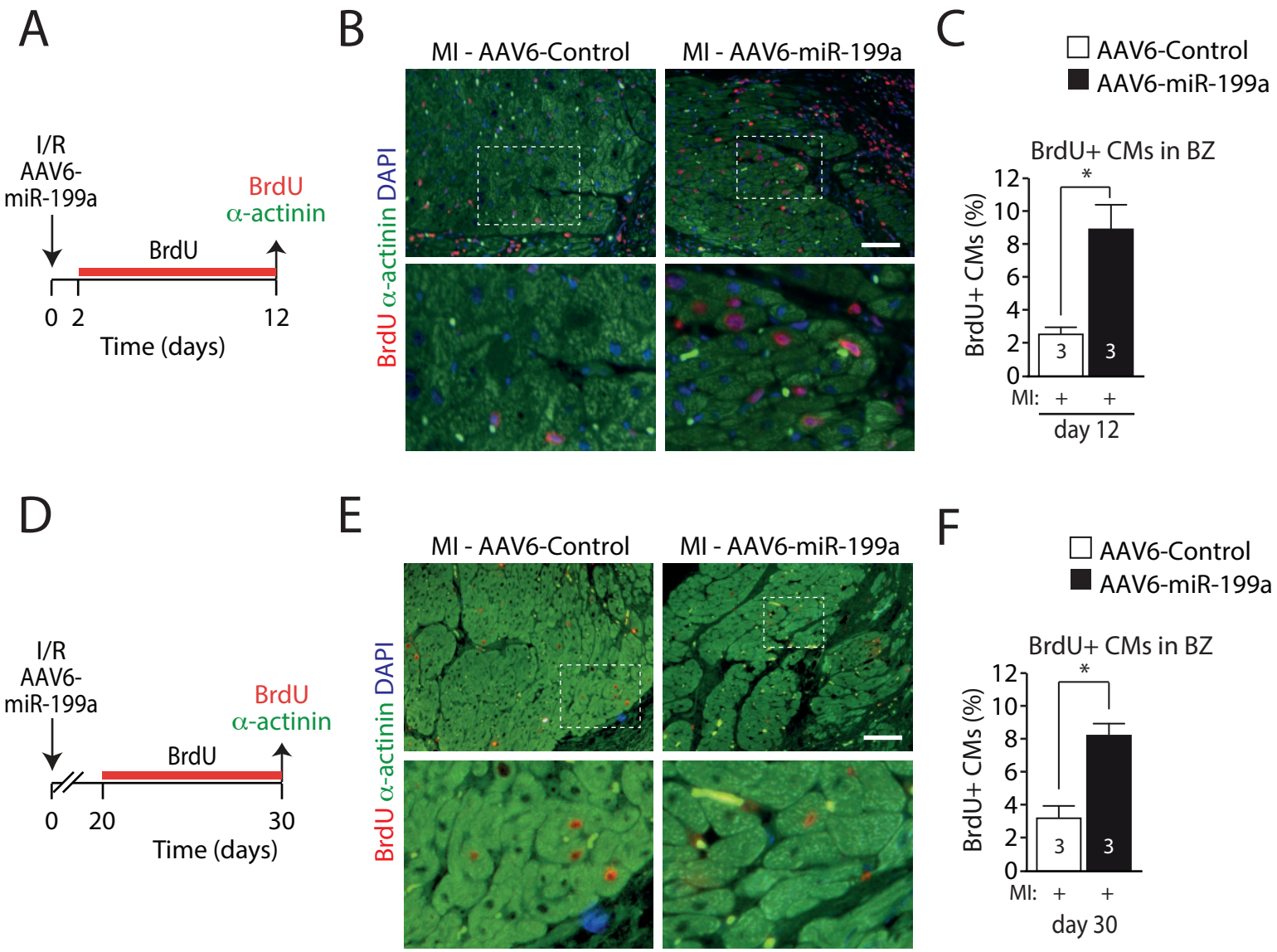
A
I/R
AAV6-
miR-199a
BrdU
α-actinin
BrdU
0 2
12
Time (days)
B
MI - AAV6-Control
MI - AAV6-miR-199a
BrdU α-actinin DAPI
C
AAV6-Control
AAV6-miR-199a
BrdU+ CMs in BZ
BrdU+ CMs (%)
12
10
8
6
4
2
0
*
3
3
MI: + +
day 12
D
I/R
AAV6-
miR-199a
BrdU
α-actinin
BrdU
0 20
30
Time (days)
E
MI - AAV6-Control
MI - AAV6-miR-199a
BrdU α-actinin DAPI
F
AAV6-Control
AAV6-miR-199a
BrdU+ CMs in BZ
BrdU+ CMs (%)
12
10
8
6
4
2
0
*
3
3
MI: + +
day 30

Figure 11

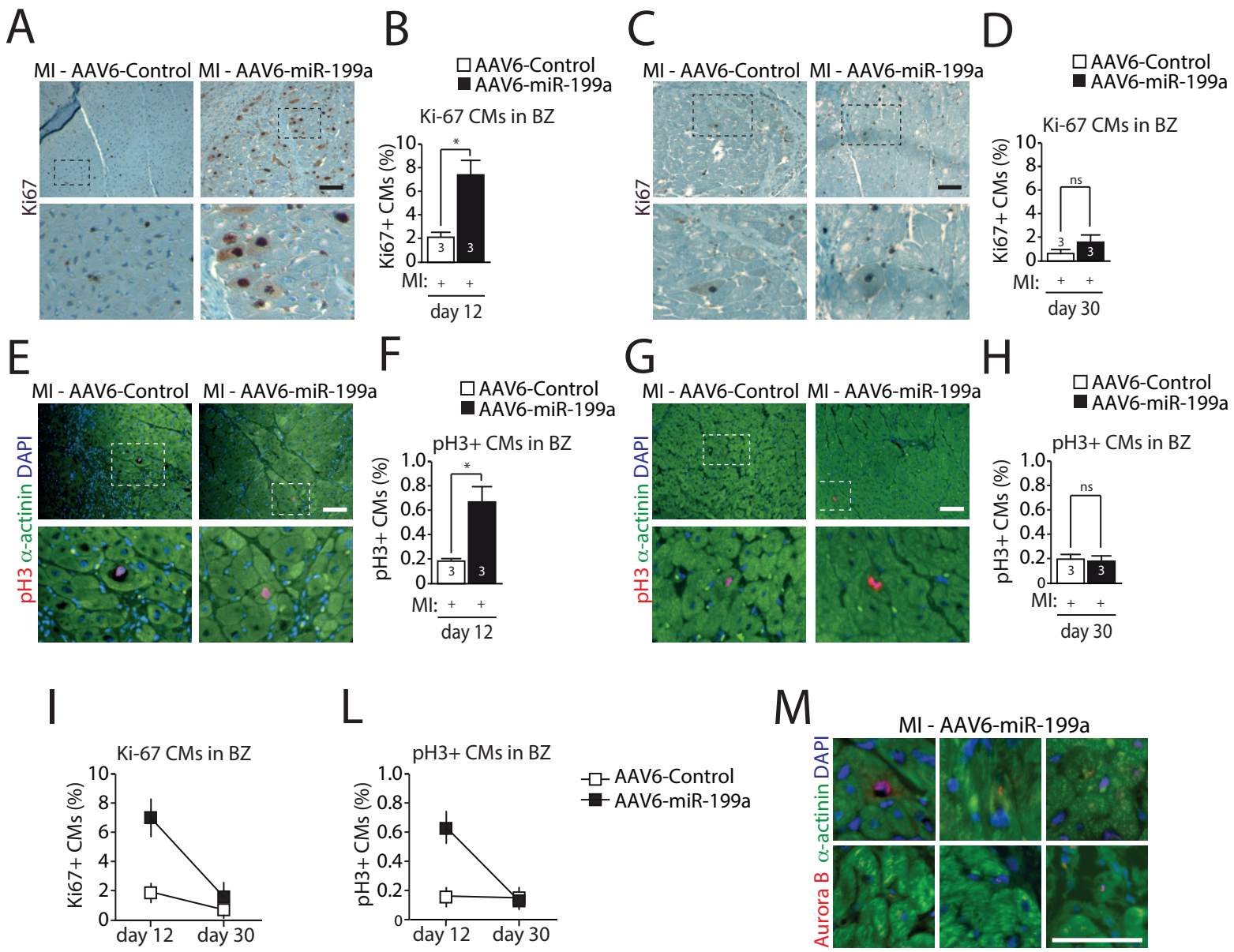
A
MI - AAV6-Control
MI - AAV6-miR-199a
Ki67
B
AAV6-Control
AAV6-miR-199a
Ki-67 CMs in BZ
Ki67+ CMs (%)
MI:
day 12
C
MI - AAV6-Control
MI - AAV6-miR-199a
Ki67
D
AAV6-Control
AAV6-miR-199a
Ki-67 CMs in BZ
Ki67+ CMs (%)
ns
MI:
day 30
E
MI - AAV6-Control
MI - AAV6-miR-199a
pH3 α-actinin DAPI
F
AAV6-Control
AAV6-miR-199a
pH3+ CMs in BZ
pH3+ CMs (%)
MI:
day 12
G
MI - AAV6-Control
MI - AAV6-miR-199a
pH3 α-actinin DAPI
H
AAV6-Control
AAV6-miR-199a
pH3+ CMs in BZ
pH3+ CMs (%)
ns
MI:
day 30
I
Ki-67 CMs in BZ
Ki67+ CMs (%)
day 12
day 30
L
pH3+ CMs in BZ
pH3+ CMs (%)
AAV6-Control
AAV6-miR-199a
day 12
day 30
M
MI - AAV6-miR-199a
Aurora B α-actinin DAPI

Figure 12

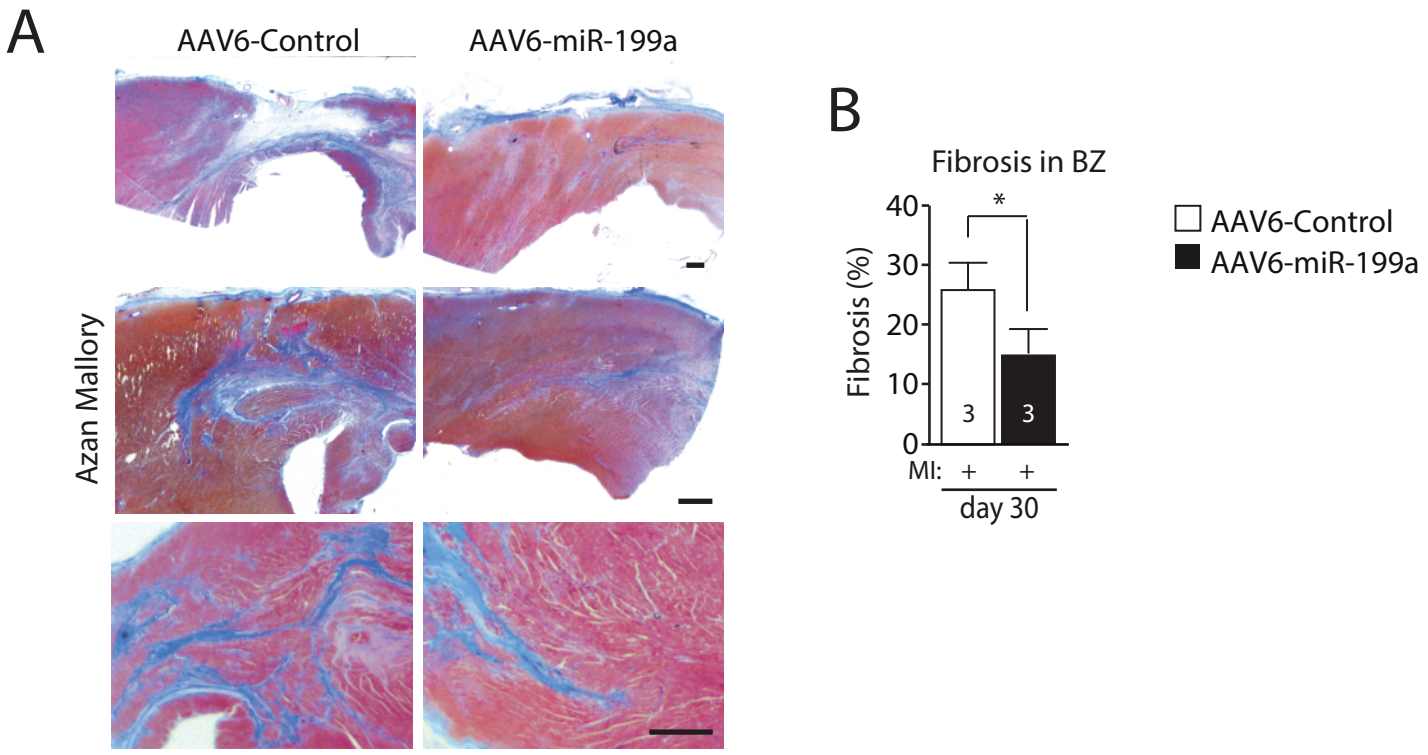
A
AAV6-Control
AAV6-miR-199a
Azan Mallory
B
Fibrosis in BZ
Fibrosis (%)
40
30
20
10
0
*
3
3
MI: + +
day 30
AAV6-Control
AAV6-miR-199a

Figure 13

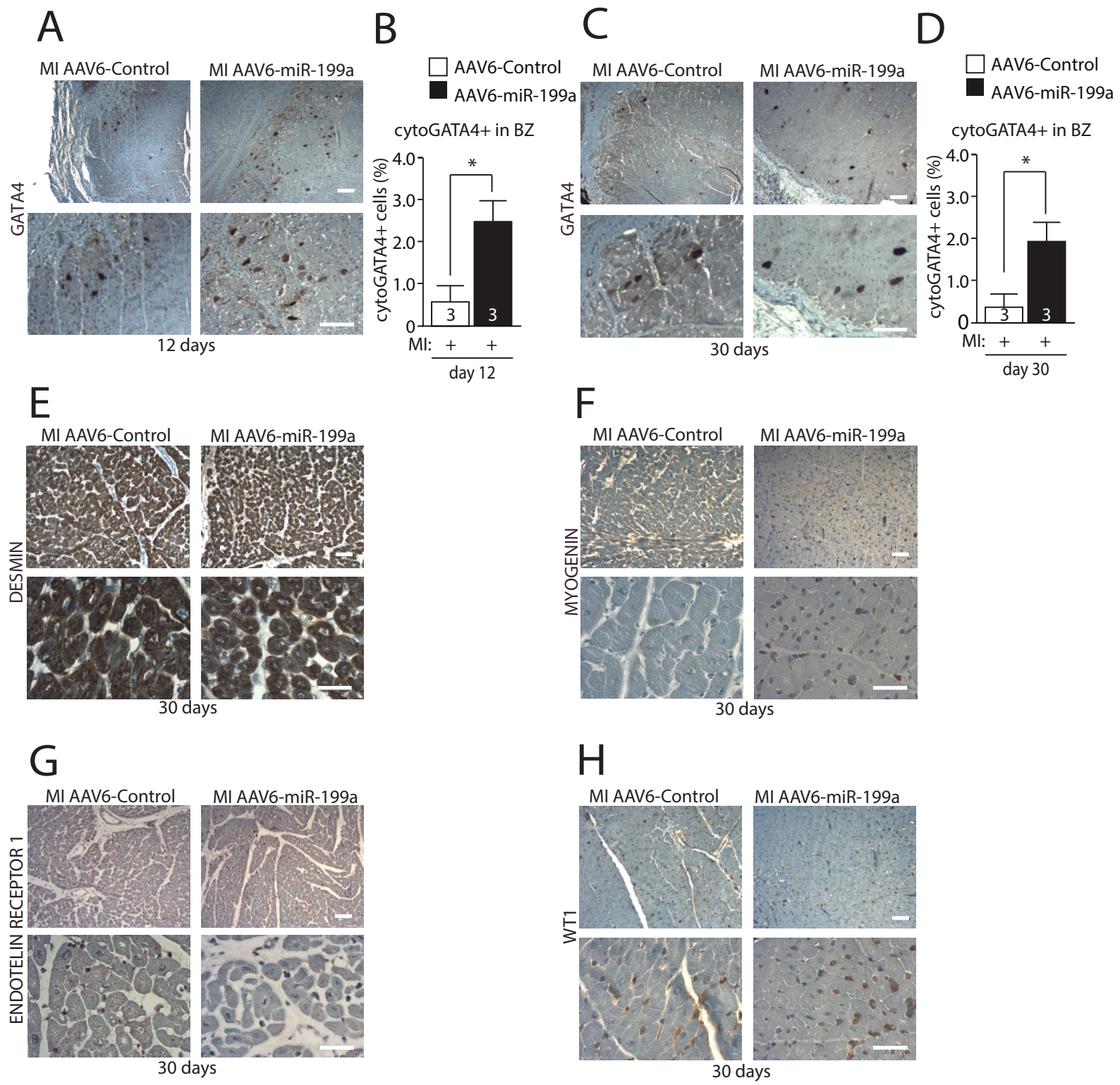
A
MI AAV6-Control
MI AAV6-miR-199a
GATA4
12 days
B
AAV6-Control
AAV6-miR-199a
cytoGATA4+ in BZ
cytoGATA4+ cells (%)
4.0
3.0
2.0
1.0
0
*
3
3
MI: + +
day 12
C
MI AAV6-Control
MI AAV6-miR-199a
GATA4
30 days
D
AAV6-Control
AAV6-miR-199a
cytoGATA4+ in BZ
cytoGATA4+ cells (%)
4.0
3.0
2.0
1.0
0
*
3
3
MI: + +
day 30
E
MI AAV6-Control
MI AAV6-miR-199a
DESMIN
30 days
F
MI AAV6-Control
MI AAV6-miR-199a
MYOGENIN
30 days
G
MI AAV6-Control
MI AAV6-miR-199a
ENDOTELIN RECEPTOR 1
30 days
H
MI AAV6-Control
MI AAV6-miR-199a
WT1
30 days

Figure 14

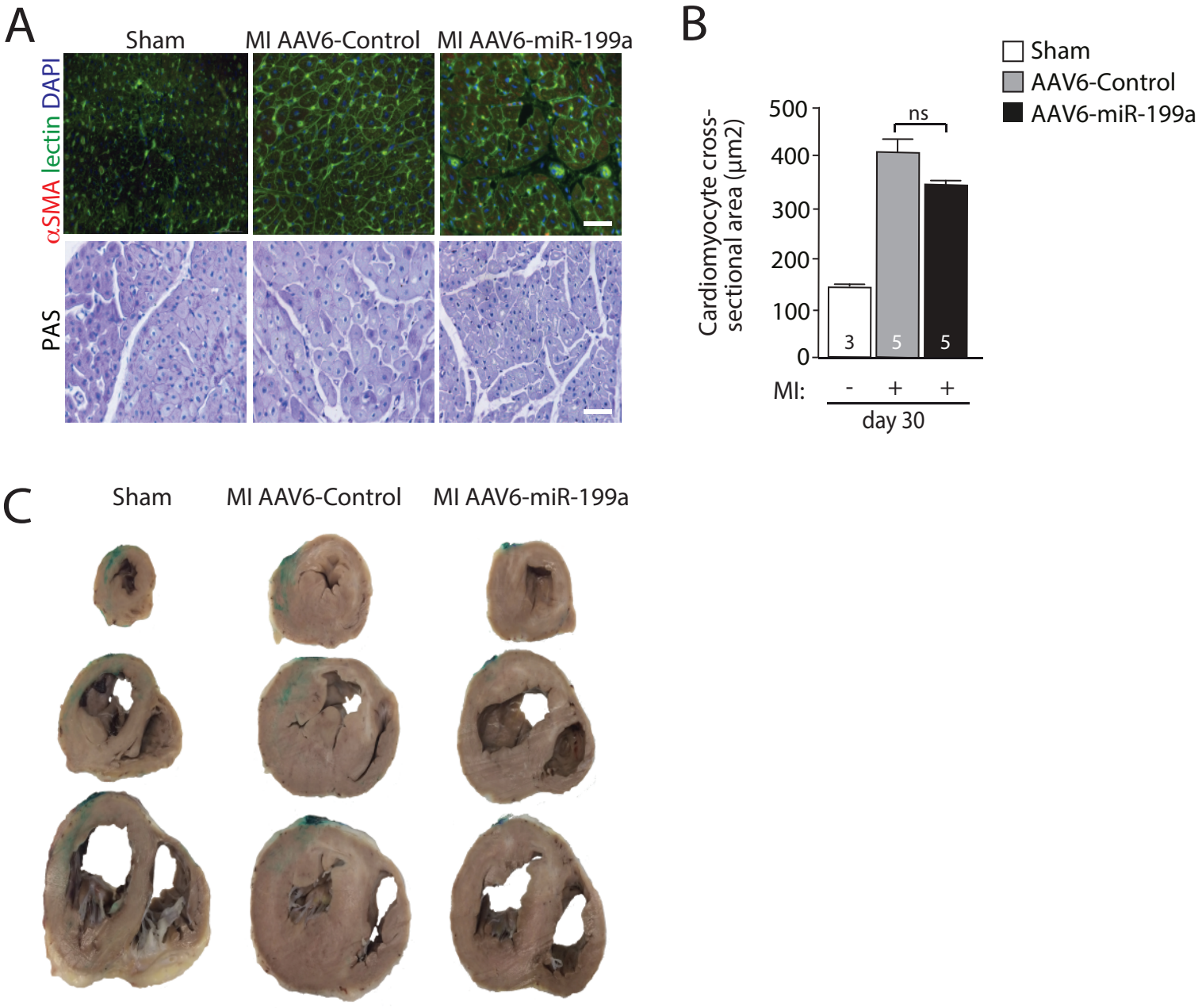
A
Sham
MI AAV6-Control
MI AAV6-miR-199a
αSMA lectin DAPI
PAS
B
Sham
AAV6-Control
AAV6-miR-199a
Cardiomyocyte cross-sectional area (µm2)
500
400
300
200
100
0
ns
3
5
5
MI:
-
+
+
day 30
C
Sham
MI AAV6-Control
MI AAV6-miR-199a

Figure 15

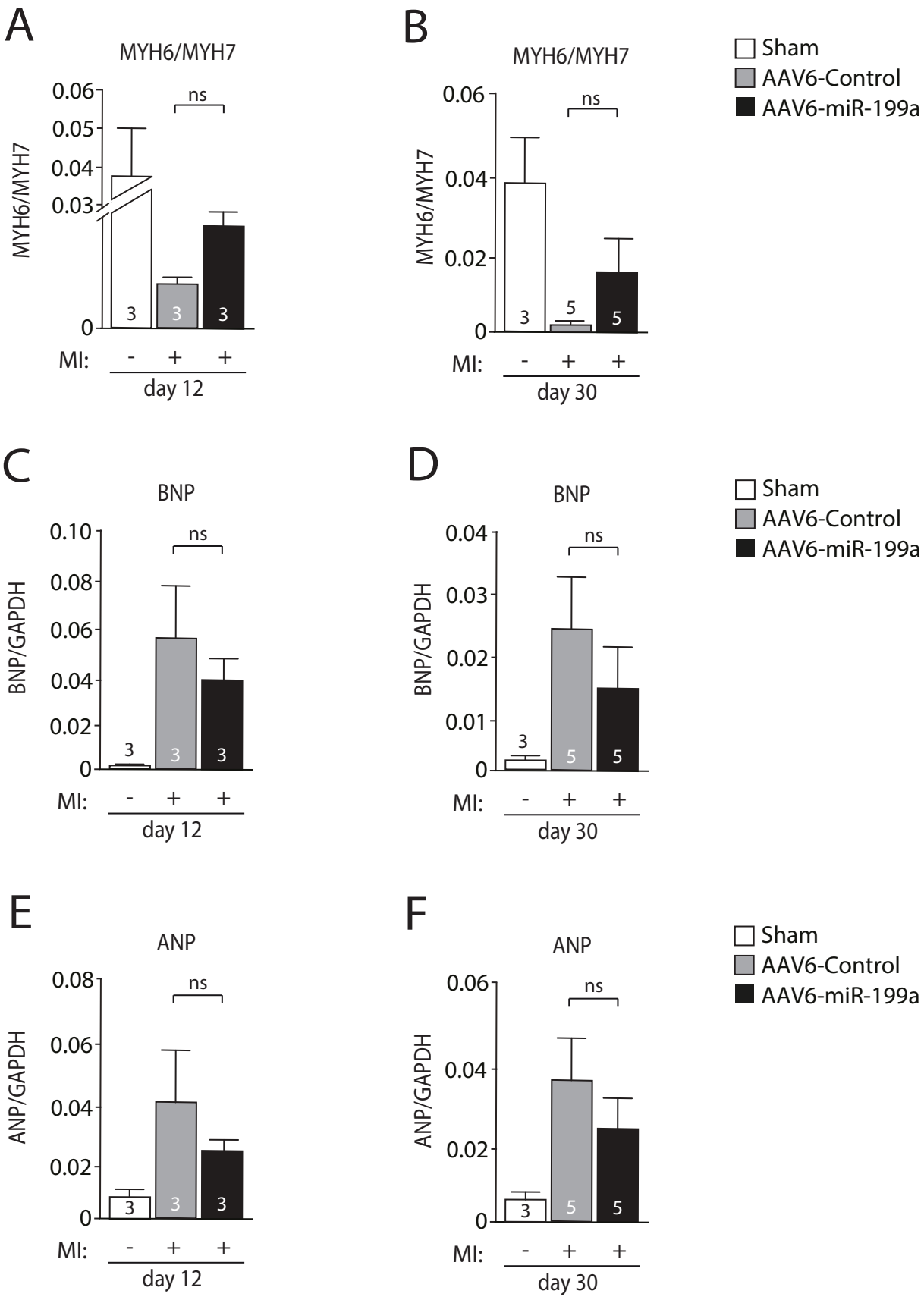
A
MYH6/MYH7
MYH6/MYH7
0.06
0.05
0.04
0.03
0
ns
3
3
3
MI: - + +
day 12
B
MYH6/MYH7
MYH6/MYH7
0.06
0.04
0.02
0
ns
3
5
5
MI: - + +
day 30
Sham
AAV6-Control
AAV6-miR-199a
C
BNP
BNP/GAPDH
0.10
0.08
0.06
0.04
0.02
0
ns
3
3
3
MI: - + +
day 12
D
BNP
BNP/GAPDH
0.04
0.03
0.02
0.01
0
ns
3
5
5
MI: - + +
day 30
Sham
AAV6-Control
AAV6-miR-199a
E
ANP
ANP/GAPDH
0.08
0.06
0.04
0.02
0
ns
3
3
3
MI: - + +
day 12
F
ANP
ANP/GAPDH
0.06
0.04
0.02
0
ns
3
5
5
MI: - + +
day 30
Sham
AAV6-Control
AAV6-miR-199a

Figure 16

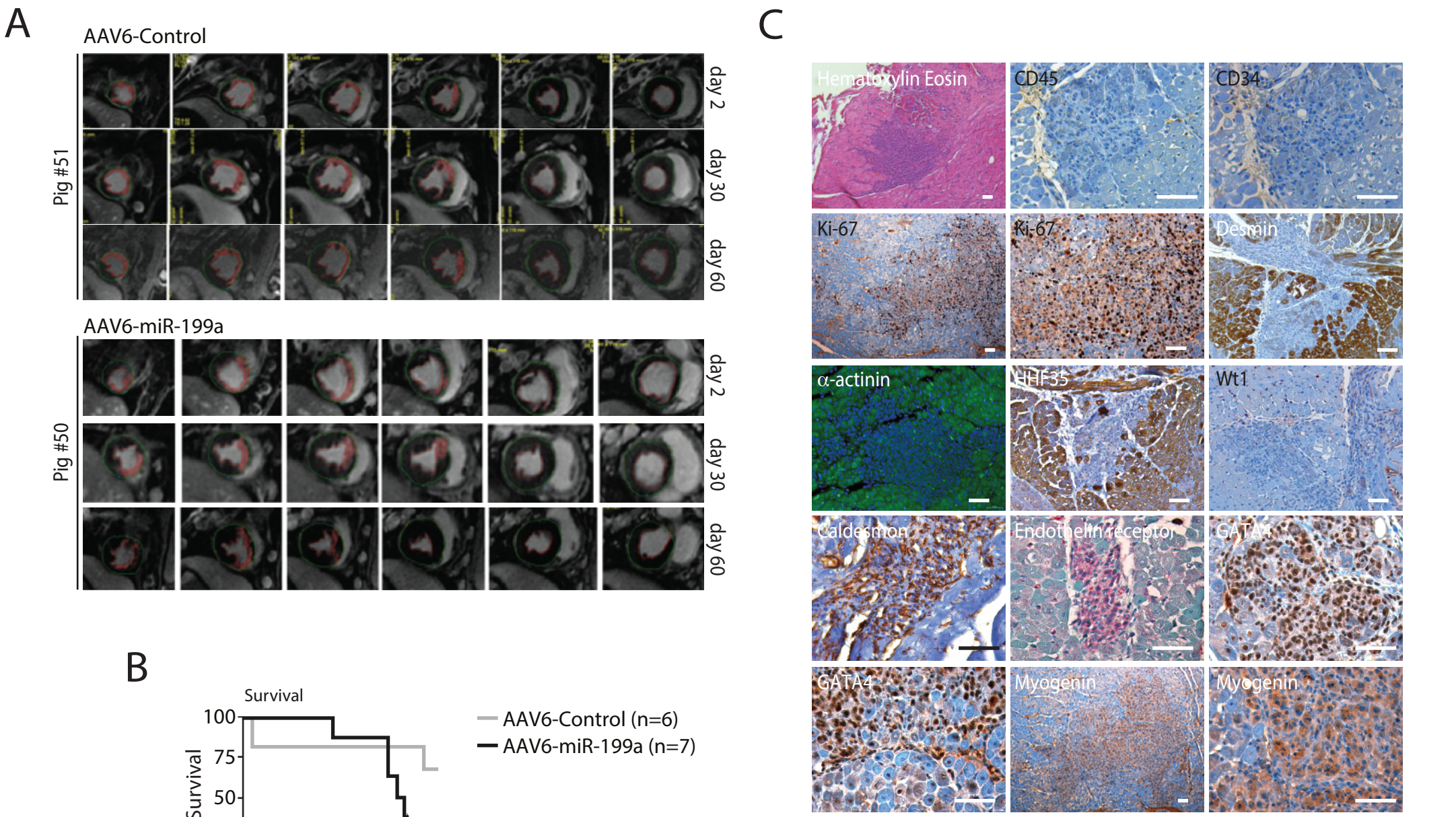
A
AAV6-Control
Pig #51
day 2
day 30
day 60
AAV6-miR-199a
Pig #50
day 2
day 30
day 60
B
Survival
% Survival
100
75
50
25
0
0
20
40
60
Days
AAV6-Control (n=6)
AAV6-miR-199a (n=7)
C
Hematoxylin Eosin
CD45
CD34
Ki-67
Ki-67
Desmin
α-actinin
HHF35
Wt1
Caldesmon
Endothelin receptor
GATA4
GATA4
Myogenin
Myogenin

Figure 17

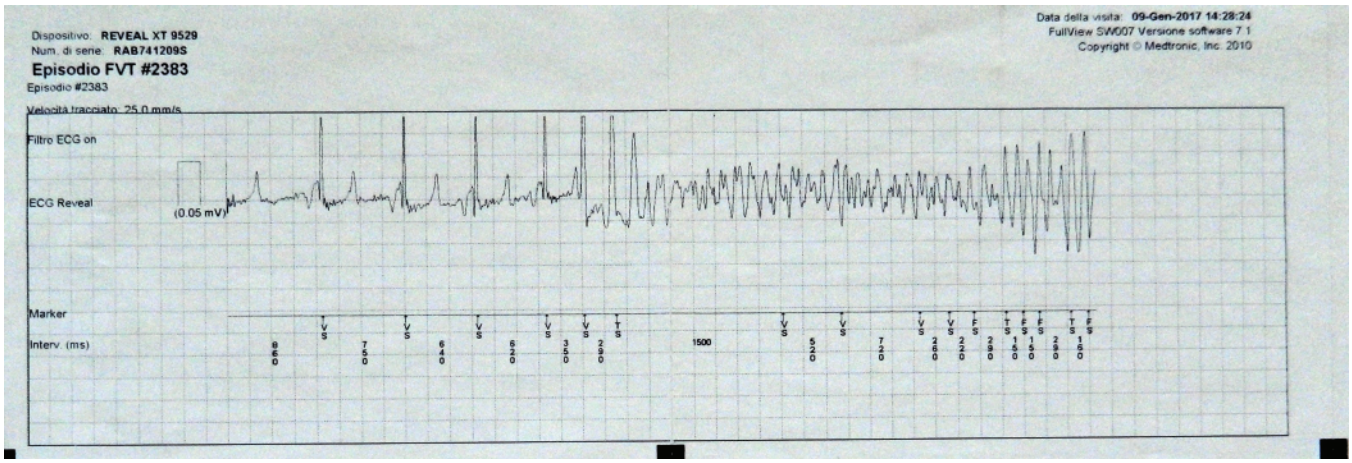
Dispositivo: REVEAL XT 9529
Num. di serie: RAB741209S
Episodio FVT #2383
Episodio #2383
Velocità tracciato: 25.0 mm/s
Filtro ECG on
ECG Reveal
(0.05 mV)
Marker
Interv. (ms)
Data della visita: 09-Gen-2017 14:28:24
FullView SW007 Versione software 7.1
Copyright © Medtronic, Inc. 2010

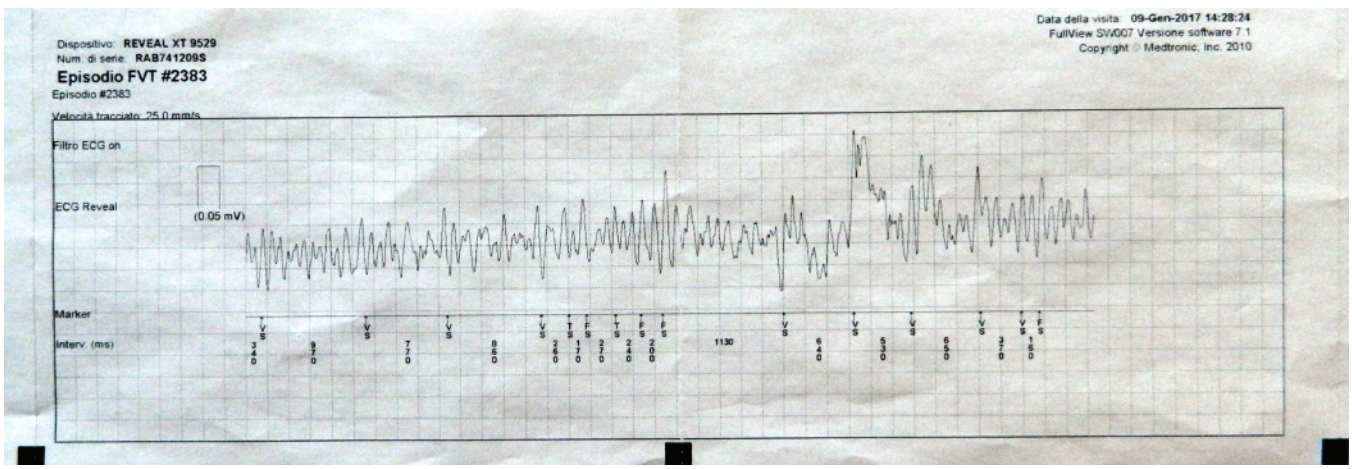
Dispositivo: REVEAL XT 9529
Num. di serie: RAB741209S
Episodio FVT #2383
Episodio #2383
Velocità tracciato: 25.0 mm/s
Filtro ECG on
ECG Reveal
(0.05 mV)
Marker
Interv. (ms)
Data della visita: 09-Gen-2017 14:28:24
FullView SW007 Versione software 7.1
Copyright © Medtronic, Inc. 2010

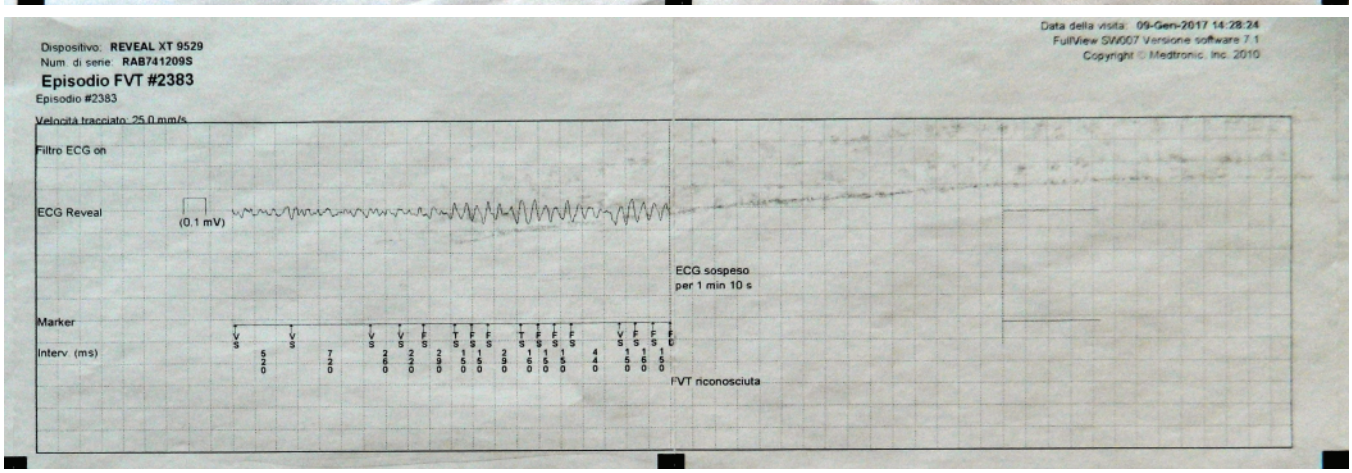
Dispositivo: REVEAL XT 9529
Num. di serie: RAB741209S
Episodio FVT #2383
Episodio #2383
Velocità tracciato: 25.0 mm/s
Filtro ECG on
ECG Reveal
(0.1 mV)
ECG sospeso
per 1 min 10 s
Marker
Interv. (ms)
FVT riconosciuta
Data della visita: 09-Gen-2017 14:28:24
FullView SW007 Versione software 7.1
Copyright © Medtronic, Inc. 2010

Figure 18

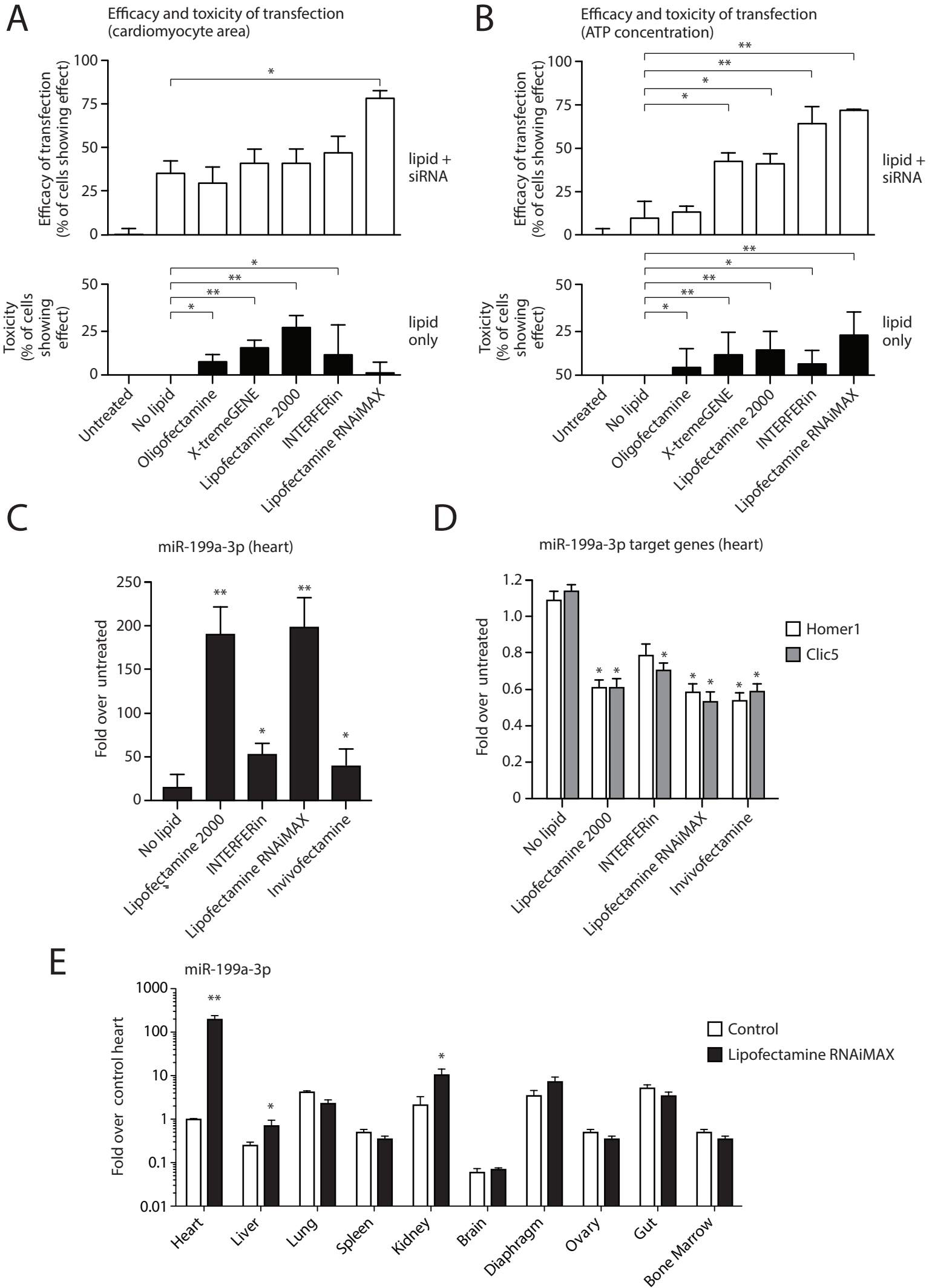
A
Efficacy and toxicity of transfection
(cardiomyocyte area)
Efficacy of transfection
(% of cells showing effect)
lipid +
siRNA
Toxicity
(% of cells
showing
effect)
lipid
only
Untreated
No lipid
Oligofectamine
X-tremeGENE
Lipofectamine 2000
INTERFERin
Lipofectamine RNAiMAX
B
Efficacy and toxicity of transfection
(ATP concentration)
C
miR-199a-3p (heart)
Fold over untreated
No lipid
Lipofectamine 2000
INTERFERin
Lipofectamine RNAiMAX
Invivofectamine
D
miR-199a-3p target genes (heart)
Homer1
Clic5
E
miR-199a-3p
Fold over control heart
Control
Lipofectamine RNAiMAX
Heart
Liver
Lung
Spleen
Kidney
Brain
Diaphragm
Ovary
Gut
Bone Marrow

Figure 19

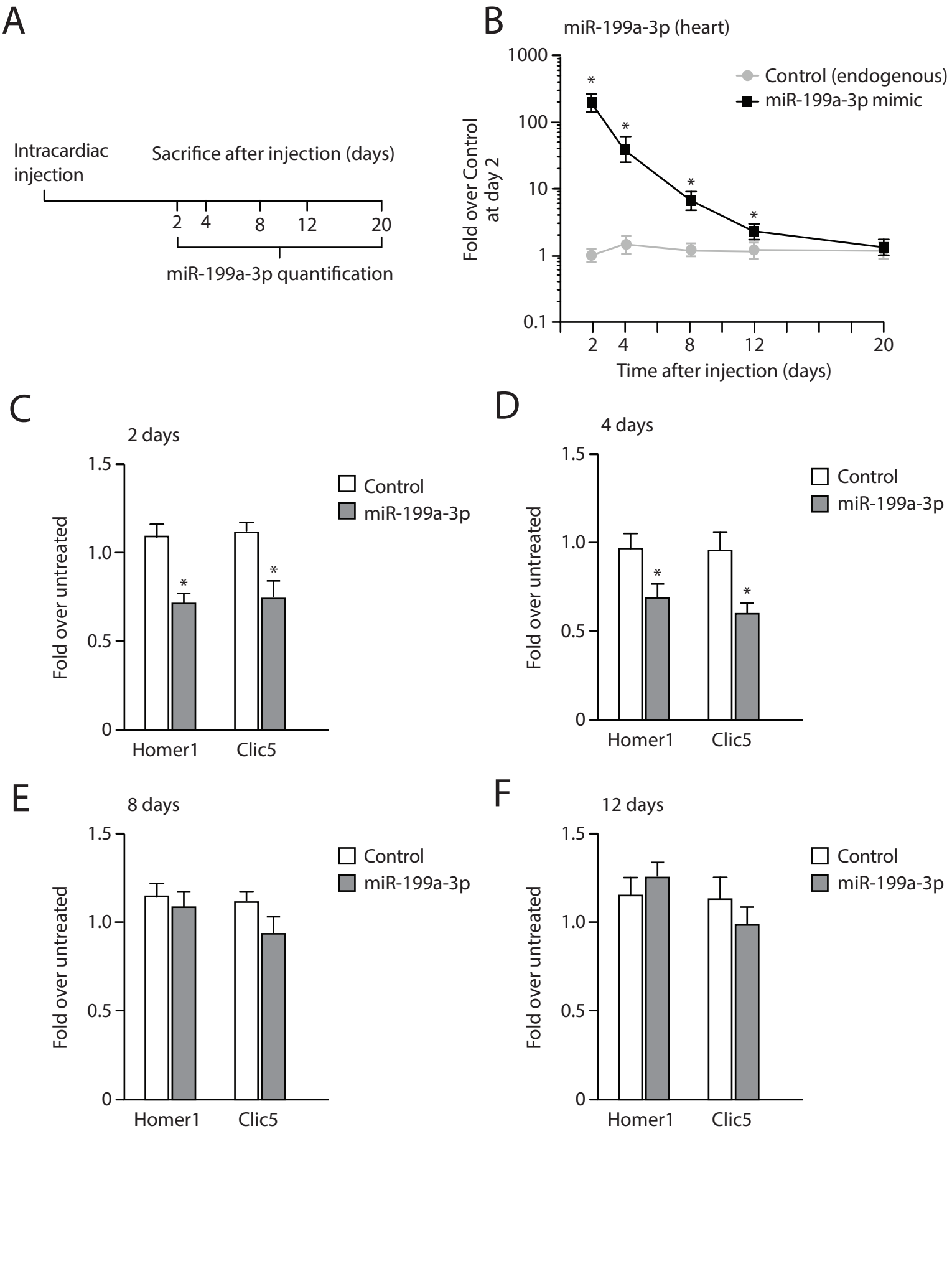
A
Intracardiac injection
Sacrifice after injection (days)
2
4
8
12
20
miR-199a-3p quantification
B
miR-199a-3p (heart)
Control (endogenous)
miR-199a-3p mimic
Fold over Control at day 2
1000
100
10
1
0.1
Time after injection (days)
C
2 days
Control
miR-199a-3p
Fold over untreated
1.5
1.0
0.5
0
Homer1
Clic5
D
4 days
E
8 days
F
12 days

Figure 20

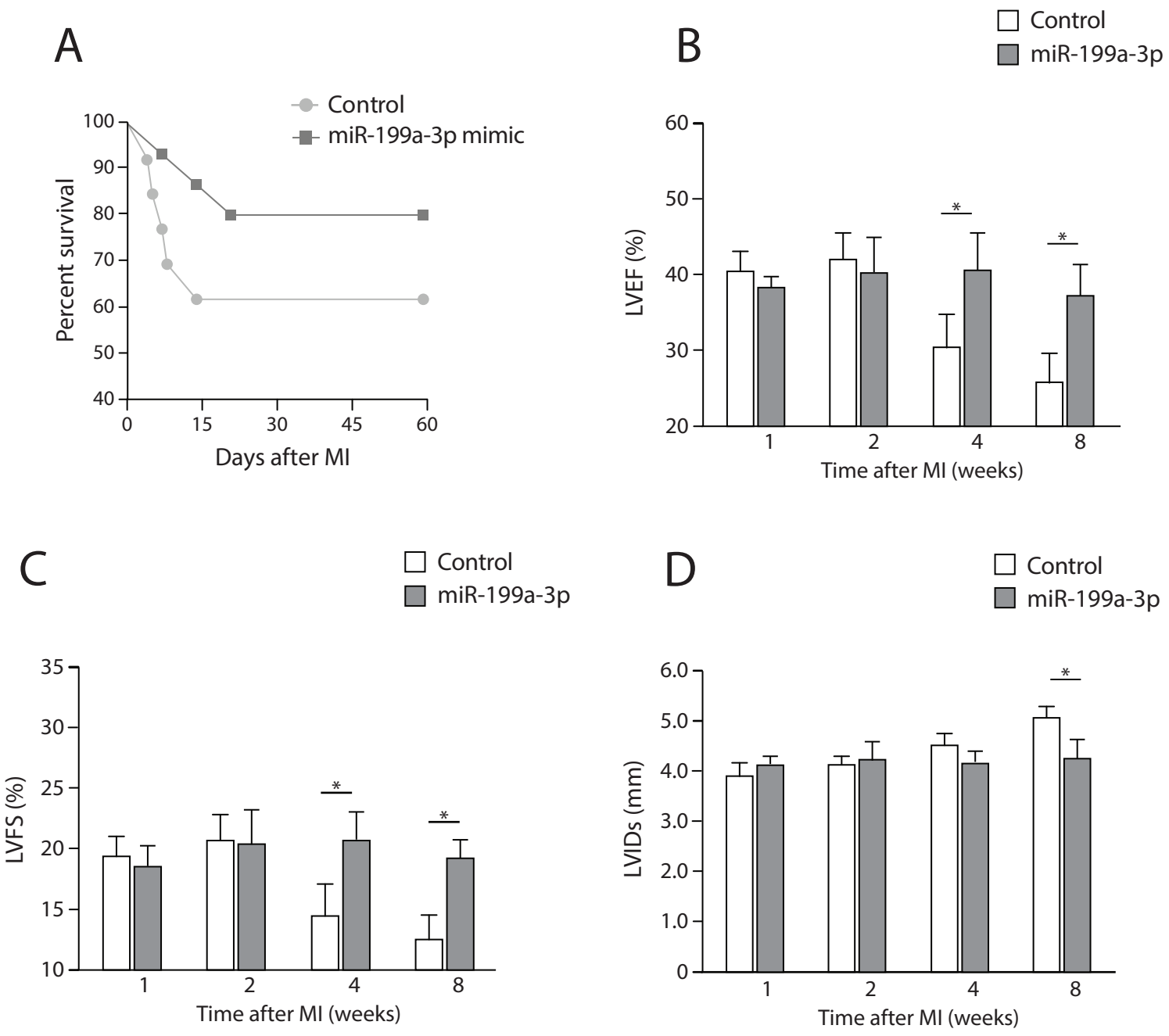
A
Control
miR-199a-3p mimic
Percent survival
100
90
80
70
60
50
40
0
15
30
45
60
Days after MI
B
Control
miR-199a-3p
LVEF (%)
60
50
40
30
20
*
*
1
2
4
8
Time after MI (weeks)
C
Control
miR-199a-3p
LVFS (%)
35
30
25
20
15
10
*
*
1
2
4
8
Time after MI (weeks)
D
Control
miR-199a-3p
LVIDs (mm)
6.0
5.0
4.0
3.0
2.0
1.0
0
*
1
2
4
8
Time after MI (weeks)

Figure 21

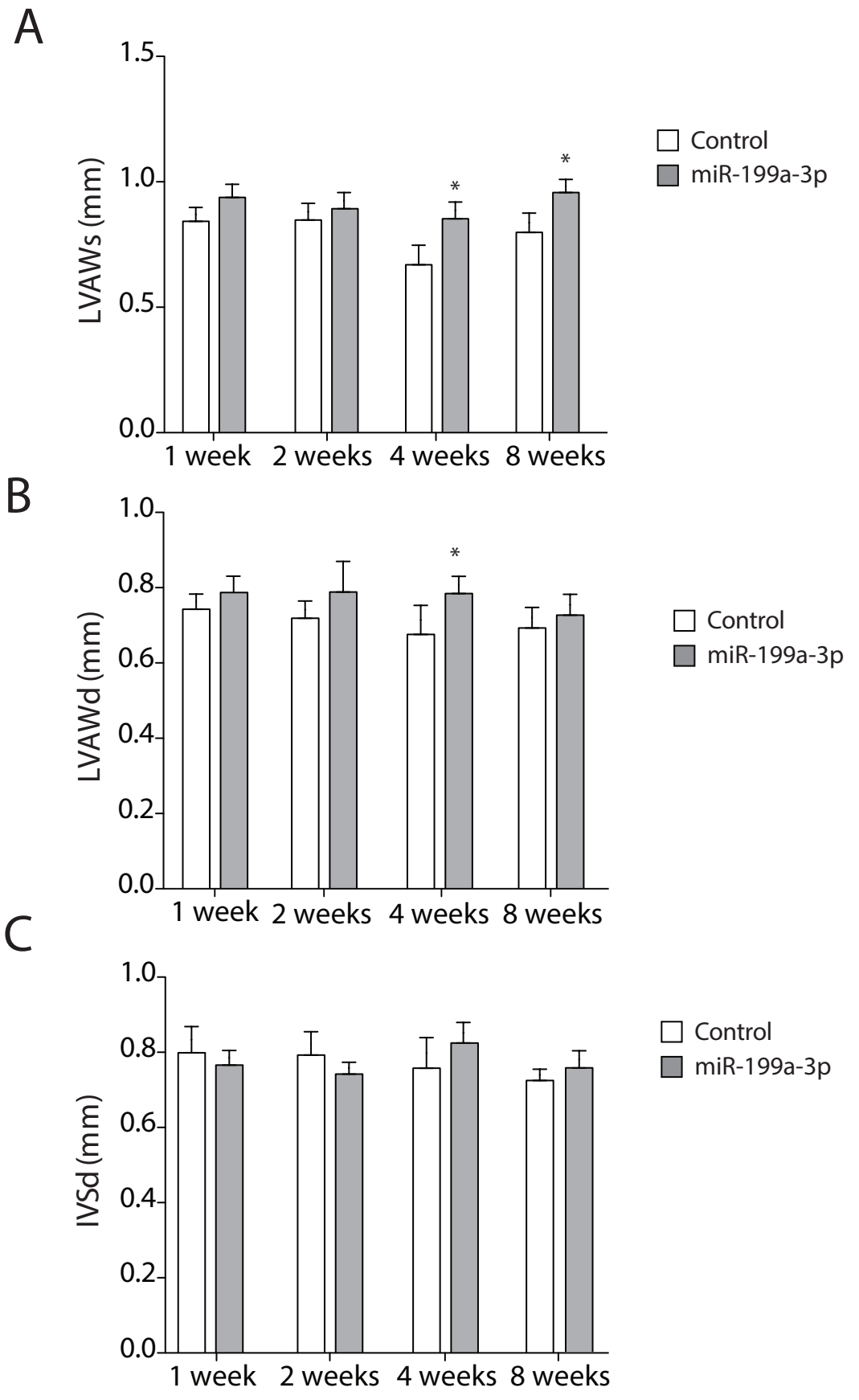
A
1.5
1.0
0.5
0.0
LVAWs (mm)
*
*
1 week
2 weeks
4 weeks
8 weeks
Control
miR-199a-3p
B
1.0
0.8
0.6
0.4
0.2
0.0
LVAWd (mm)
*
1 week
2 weeks
4 weeks
8 weeks
Control
miR-199a-3p
C
1.0
0.8
0.6
0.4
0.2
0.0
IVSd (mm)
1 week
2 weeks
4 weeks
8 weeks
Control
miR-199a-3p

Figure 22

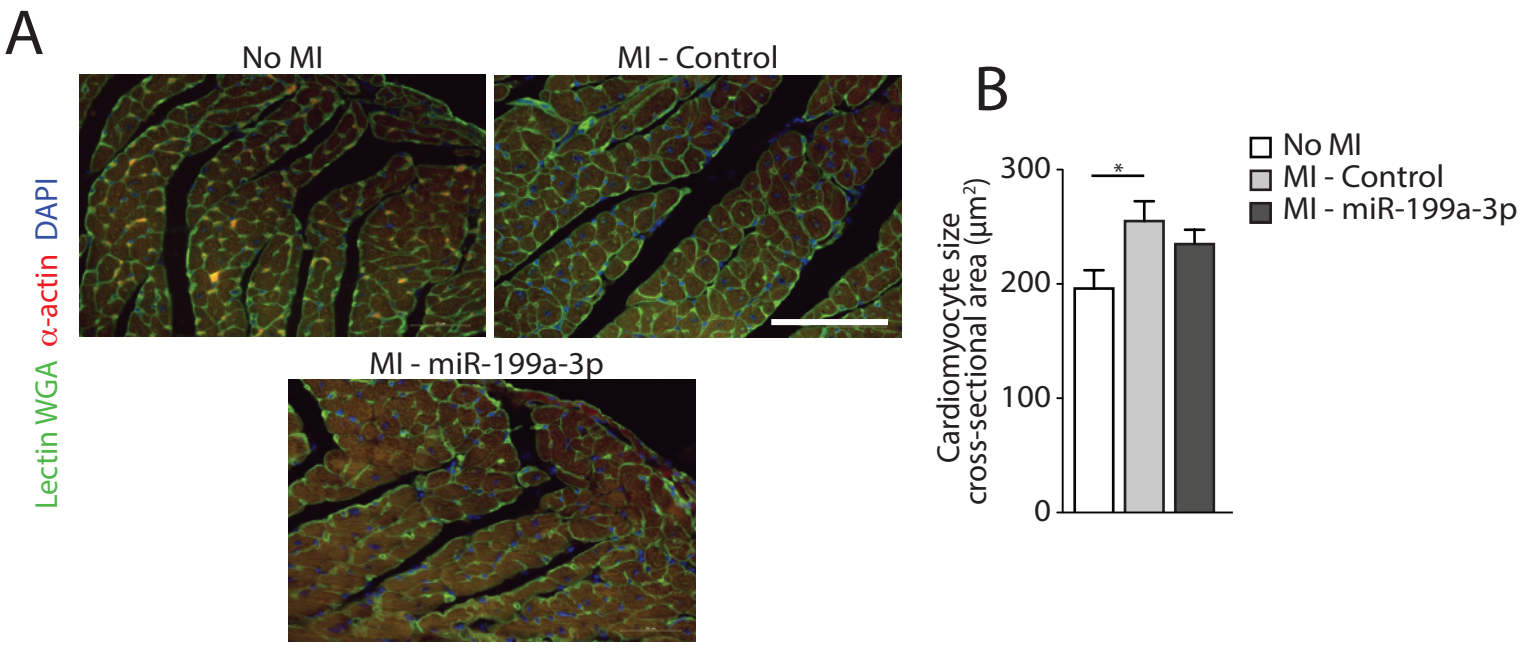
A
No MI
MI - Control
MI - miR-199a-3p
Lectin WGA α-actin DAPI
B
Cardiomyocyte size cross-sectional area (µm²)
300
200
100
0
*
No MI
MI - Control
MI - miR-199a-3p

Figure 23

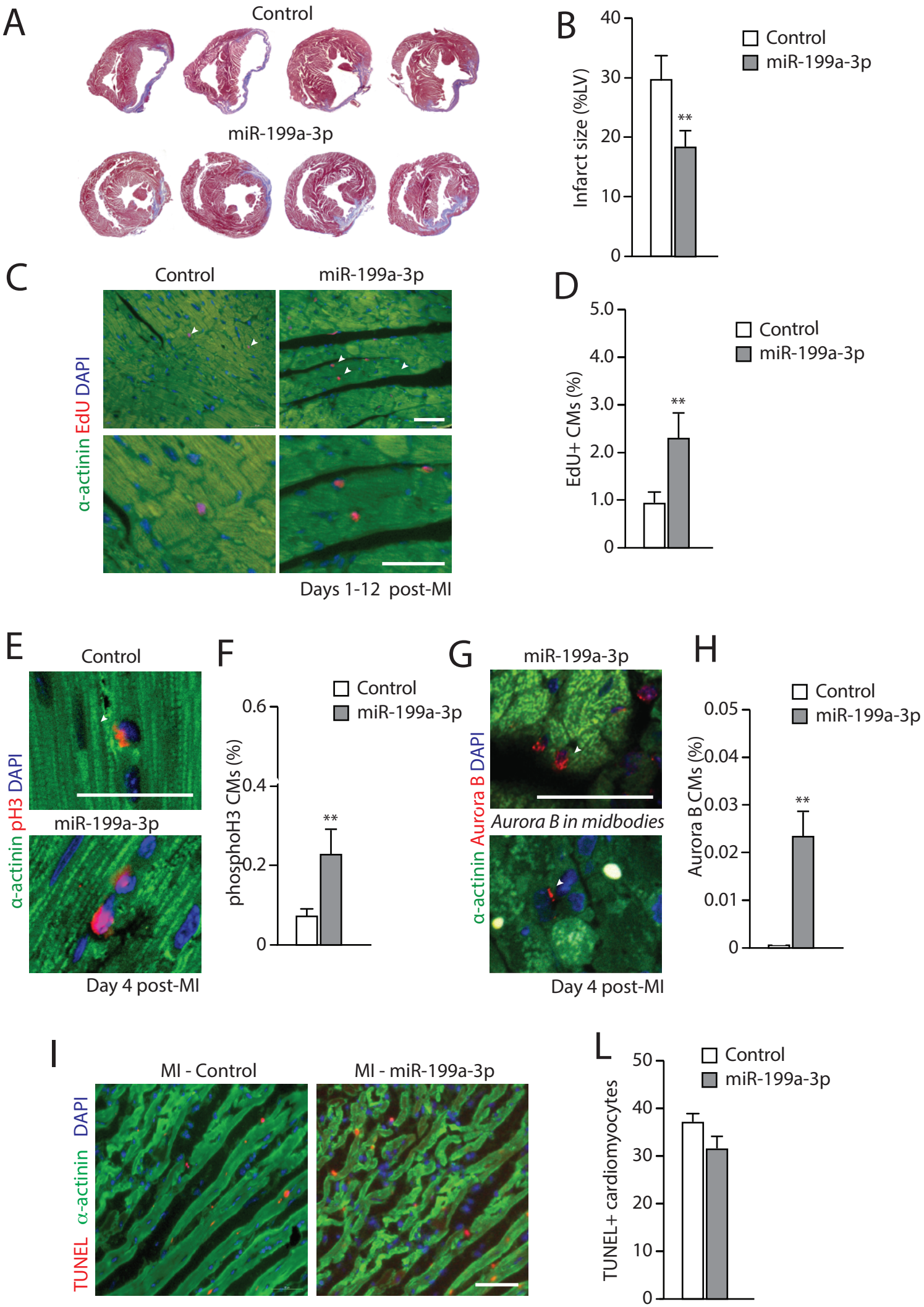
A
Control
miR-199a-3p
B
Infarct size (%LV)
40
30
20
10
0
**
Control
miR-199a-3p
C
Control
miR-199a-3p
α-actinin EdU DAPI
Days 1-12 post-MI
D
EdU+ CMs (%)
5.0
4.0
3.0
2.0
1.0
0
**
Control
miR-199a-3p
E
Control
miR-199a-3p
α-actinin pH3 DAPI
Day 4 post-MI
F
phosphoH3 CMs (%)
0.6
0.4
0.2
0
**
Control
miR-199a-3p
G
miR-199a-3p
α-actinin Aurora B DAPI
Aurora B in midbodies
Day 4 post-MI
H
Aurora B CMs (%)
0.05
0.04
0.03
0.02
0.01
0
**
Control
miR-199a-3p
I
MI - Control
MI - miR-199a-3p
TUNEL α-actinin DAPI
L
TUNEL+ cardiomyocytes
50
40
30
20
10
0
Control
miR-199a-3p

Figure 24

A

Name:	Chemical modifications:	Provided by:
E1	LNA + phosphorothioate stabilization at 5′ and 3′	Exiqon
E2	LNA + phosphorothioate stabilization at 5′ and 3 + 2′-O-Me modification on the passanger	Exiqon
E3	2-F mimic + phosphorothioate stabilization + 2′-O-Me modification on the passanger (design A)	Exiqon
E4	2-F mimic + phosphorothioate stabilization + 2′-O-Me modification on the passanger (design B)	Exiqon
I	2′-O-Me modification on the driver – passenger inactivated so he can not enter the RISC	IDT

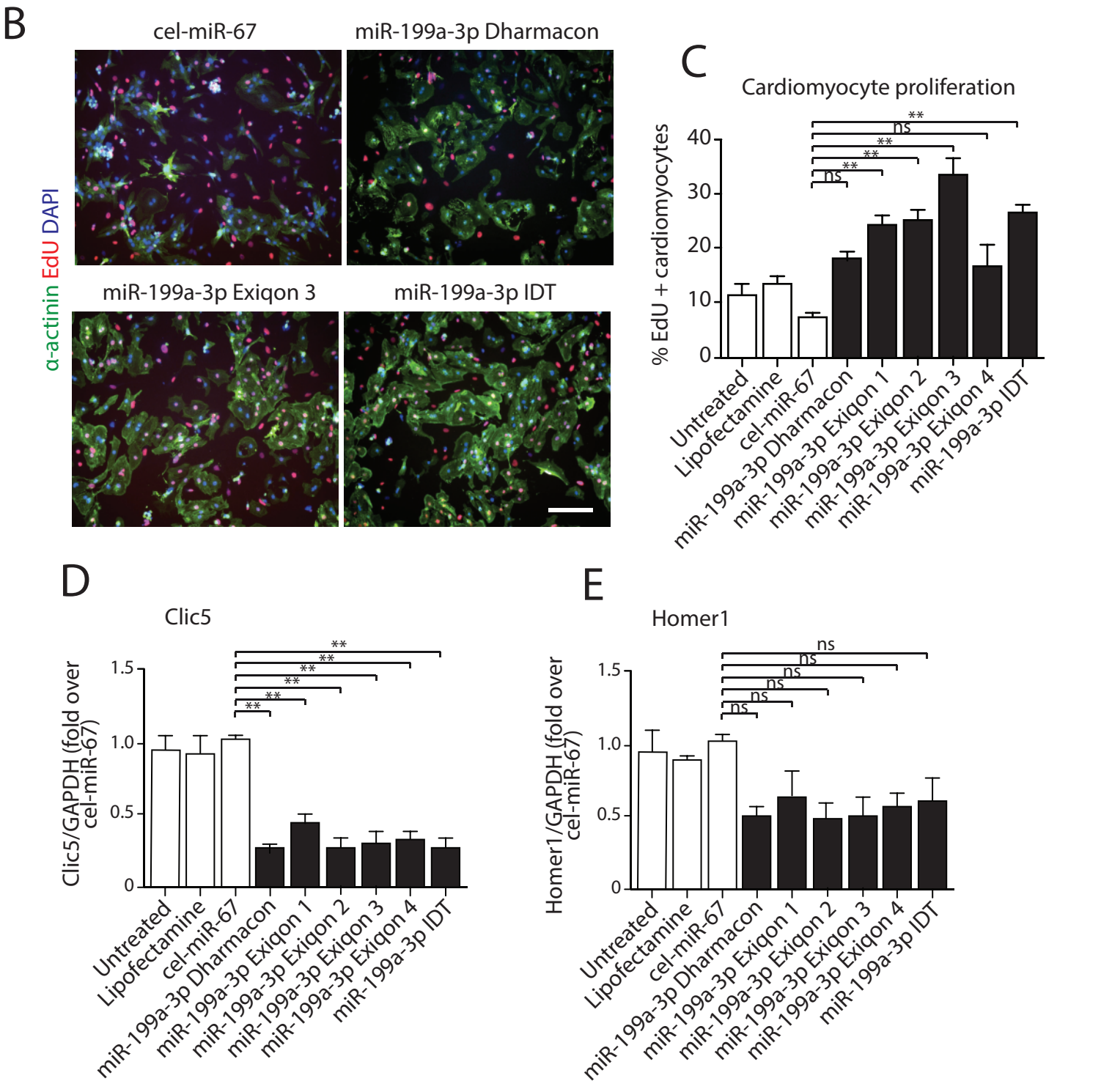

Figure 25

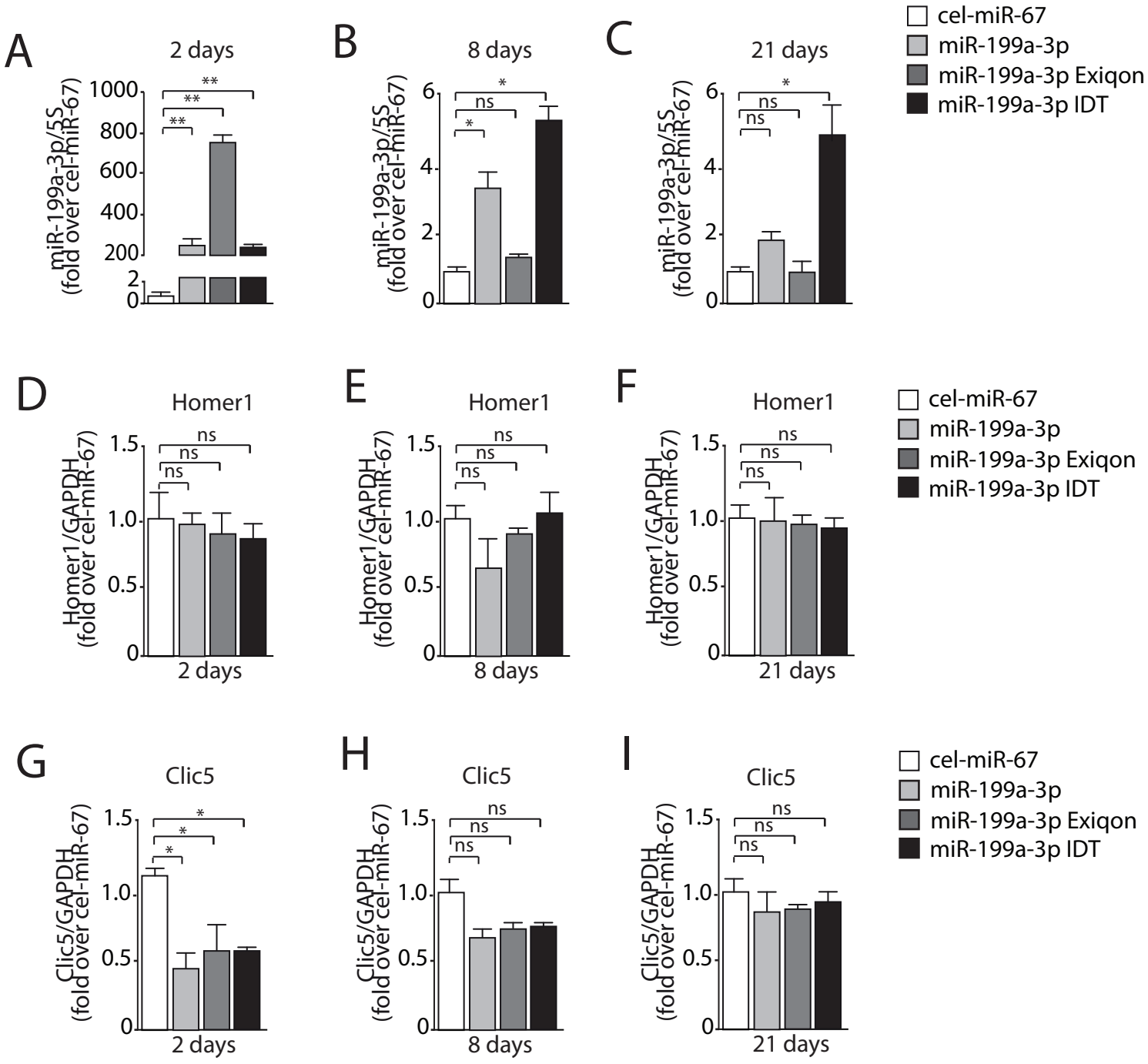
A
2 days
miR-199a-3p/5S
(fold over cel-miR-67)
1000
800
600
400
200
2
0
**
**
**
B
8 days
miR-199a-3p/5S
(fold over cel-miR-67)
6
4
2
0
*
ns
*
C
21 days
miR-199a-3p/5S
(fold over cel-miR-67)
6
4
2
0
*
ns
ns
cel-miR-67
miR-199a-3p
miR-199a-3p Exiqon
miR-199a-3p IDT
D
Homer1
Homer1/GAPDH
(fold over cel-miR-67)
1.5
1.0
0.5
0
ns
ns
ns
2 days
E
Homer1
Homer1/GAPDH
(fold over cel-miR-67)
1.5
1.0
0.5
0
ns
ns
ns
8 days
F
Homer1
Homer1/GAPDH
(fold over cel-miR-67)
1.5
1.0
0.5
0
ns
ns
ns
21 days
cel-miR-67
miR-199a-3p
miR-199a-3p Exiqon
miR-199a-3p IDT
G
Clic5
Clic5/GAPDH
(fold over cel-miR-67)
1.5
1.0
0.5
0
*
*
*
2 days
H
Clic5
Clic5/GAPDH
(fold over cel-miR-67)
1.5
1.0
0.5
0
ns
ns
ns
8 days
I
Clic5
Clic5/GAPDH
(fold over cel-miR-67)
1.5
1.0
0.5
0
ns
ns
ns
21 days
cel-miR-67
miR-199a-3p
miR-199a-3p Exiqon
miR-199a-3p IDT

Figure 26

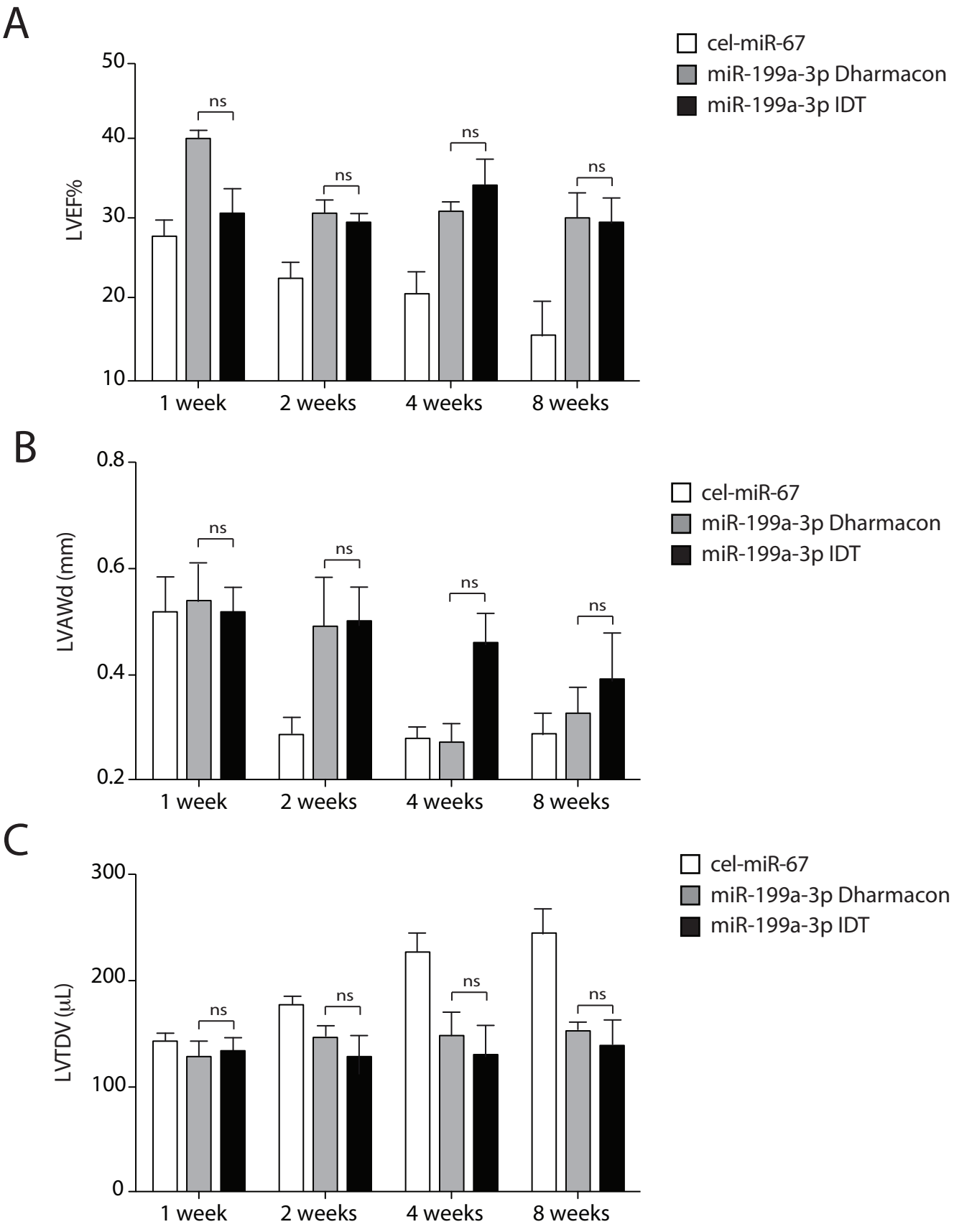
A
cel-miR-67
miR-199a-3p Dharmacon
miR-199a-3p IDT
LVEF%
50
40
30
20
10
ns
1 week
2 weeks
4 weeks
8 weeks
B
LVAWd (mm)
0.8
0.6
0.4
0.2
C
LVTDV (µL)
300
200
100
0

FIGURE LEGENDS

Figure 1. Therapeutic strategies for heart regeneration and signaling pathways involved.

The heart is commonly considered a post-mitotic organ, unable to replace cardiomyocyte loss with new functional cells after ischemic damage. Substitution of dead cardiomyocytes is the fundamental condition to re-establish cardiac structural and functional integrity. **A)** In the last decade different research lines have aimed at restoring cardiomyocyte loss by transplanting or activating cardiomyocyte progenitors, transplanting exogenous ES- or iPS-derived cardiomyocytes, direct reprogramming of fibroblast to cardiomyocyte or activating pre-exsisting cardiomyocyte proliferation (adapted from [190]. **B)** Schematic and simplified representation of the major signaling pathways involved in cardiomyocyte cell-cycle re-entry.

Figure 2. MiR-199a conservation among species and its mRNA targets.

A) Representation of miR-199a-1 and miR-199a-2 precursors. Mature miR-199a-5p and miR-199a-3p sequences are in green. **B)** Mature miR-199a-5p and miR-199a-3p sequences are conserved in human, mouse, rat and pig. Their seed sequence is in light blue and red respectively. **C)** Schematic and simplified representation of the major miR-199a transcriptional regulators and mRNA targets of miR-199a-5p and miR-199a-3p. Adapted from [90].

Figure 3. MicroRNA biogenesis.

The scheme represents microRNA biogenesis. This starts in the nucleus, where a pri-miRNA is transcribed by RNA Polymerase II or III. Subsequently, this pri-miRNA is cleaved by the microprocessor complex Drosha-DGCR8, thus generating a pre-miRNA, which is then exported into the cytoplasm by Exportin-5. Once in the cytoplasm, Dicer cleaves the pre-miRNA hairpin to produce a 20-22-nucleotide long, doublestranded RNA, the mature microRNA. Mature, double stranded RNA is loaded with Ago2 into the RISC complex, where the functional strand of the microRNA silences specific targets. Adapted from [61].

Figure 4. MicroRNA sequences and conservation.

A) List of human microRNAs tested in human fetal cardiomyocytes, their relative sequences in human, mouse, pig and rat and relative accession numbers (miRBase 21).

Figure 5. Identification of the most effective microRNA in inducing heart regeneration in human primary cultures.

A) Human fetal cardiomyocyte isolation workflow. **B)** Representative images of human fetal cardiomyocytes during isolation are shown in the upper panels. Lower panels show bright-field (left side) and fluorescence (right side) microscopy images of AAV6-GFP transduced human fetal cardiomyocytes one day after transduction. **C)** Schematic representation of the experimental procedure carried out to identify the proliferative effect of the microRNAs under investigation. **D)** Representative microscopy images of human fetal cardiomyocytes transfected with selected microRNA mimics or mock-transfected control cells. **E)** Quantification of human fetal cardiomyocyte proliferation 72 hours after selected microRNA mimic transfection. The graph represents the percentage of EdU-positive cardiomyocytes over the total number of cardiomyocytes. Data are mean±SEM of 3 independent experiments; $^{**}P<0.01$. **F)** Microscopy images of human fetal cardiomyocytes transduced with AAV6 expressing the selected microRNA precursors or AAV6-GFP (control). **G)** Quantification of human fetal cardiomyocyte proliferation 72 hours after AAV6 transduction with microRNA precursors or GFP. Data are mean±SEM of 3 indipendent experiments; $^{*}P<0.05$, $^{**}P<0.01$. Scale bar = 100 μ m.

Figure 6. Adeno-associated virus 6 (AAV) is the most effective serotype for porcine heart transduction.

A and **B)** Graphs representing viral genomes and EGFP mRNA levels, respectively, one month after direct intracardiac injection of AAV6, AAV8 and AAV9 carrying the EGFP transgene. Data are mean±SEM; n=3 per group; $^{**}P<0.01$. **C, D** and **E)** Representative images taken during porcine surgery. After thoracotomy, pericardial sac is removed **(C),** LAD is exposed **(D),** and its second branch is occluded for 90 minutes. Ten minutes after reperfusion, AAV6-Control or AAV6-miR-199a are injected in the infarcted border zone **(E). F)** Schematic representation of pig heart sectioning after sacrifice. **G** and **H)** Graphs representing miR-199a-3p quantification 12 days and 1 month after infarction and vector delivery, respectively. Data are represented as fold over endogenous levels

(AAV6-Control injected animals). Data are mean±SEM; n=3 per group for 12 days and n=4 and n=5 for AAV6-Control and AAV6-miR-199a respectively for the 30 days time-point; $^{**}P<0.01$. **I)** The scheme represents the protocol used for this study. After ischemia/reperfusion and AAV6 direct injection, animals underwent cardiac MRI at day 2 and at day 30. A group of pigs received BrdU daily from day 2 to day 12 after surgery before being sacrificed at day 12 (n=3), while an other set of animals received the analogue from day 20 to the day of sacrifice (day 30) (n=3). **L** and **M)** Graphs representing viral genomes and miR-199a levels respectively in lung, spleen, kidney, liver and heart, one month after direct intracardiac injection of AAV6-Control or AAV6-miR-199a. Data are shown as fold AAV6-Control hearts. Data are mean±SEM; n=3, $^{**}P<0.01$.

Figure 7. miR-199a treatment reduces infarct scar size.

A) Examples of T2-weighted CMRI image showing cardiac edema (a), with corresponding late gadolinium enhancement (LGE) CMR images (b) at day 2 post-MI. **B)** Edema (%LV) at two days after MI. Data are mean±SEM; n=4 AAV6-Control, n=5 AAV6-miR-199a. **C)** LGE mass (g) and size (%LV), at day 2 and day 28 post-MI. Data are mean±SEM; n=5 per group at day 2; n=9 AAV6-Control and n=10 AAV6-miR-199a at day 30; $^{*}P<0.05$. **D** and **E)** Gross anatomy of cardiac slices with corresponding LGE-MRI images in representative AAV6-Control and AAV6-miR-199a treated pig hearts, at 28 days post-MI. **F)** Cardiac MRI representative images of AAV6-Control and AAV6-miR-199a treated pig hearts 2 and 28 days after MI, from heart apex (a) to base (e) as shown in the schematic representation **(G). H)** Identification of infarct scar and gray zone by LGE-MRI. **I)** Infarct gray zone, infarct core and their ratio 28 days post-MI measured by LGE-MRI. Data are mean±SEM; n=9 AAV6-Control and n=10 AAV6-miR-199a; $^{*}P<0.05$.

Figure 8. miR-199a delivery improves global and regional cardiac function.

A) LV ejection fraction (EF, %) and **(B)** stroke volume (ml) measured by cMRI in non infarcted controls and infarcted animals at day 2 and day 28 post-MI and AAV6-Control and AAV6-miR-199a injection. **C** and **D)** LV end systolic and end diastolic volumes (ml) 2 and 28 days after MI and treatment injection, measured by cMRI. Data are mean±SEM; numbers in the bar graphs indicate the sample size; $^{*}P<0.05$.

Figure 9. AAV6-miR-199a injection after ischemia/reperfusion ameliorates regional contractility.

A) An example of cardiac short axis image with the tagging grid in diastole and systole. **B)** Subdivision of the LV short axis in 8 circumferential segments and their corresponding infarct core, border zone and the remote zone. The syringe indicates the border injected with AAVs. IS, inferoseptal; S, septal, AS, anteroseptal; A, anterior; AL, anterolateral; L, lateral; IL, inferolateral; I, inferior. **C** and **D)** Eight-segment curves corresponding to LV radial (LVE*rr)* (**C**) and circumferential (LVE*cc*) (**D**) strain at 28 days after MI. **E)** Schematic example of calculation of the area under curve (AUC) in arbitrary units. **F** and **G)** AUC for E*rr* (**F**) and Ecc (**G**). **H)** Percent segmental LV end-systolic wall thickening (LVWT). **I)** AUC for LVWT. Numbers in the bars indicate the sample size. Data are mean±SEM;. **P*<0.05 vs Sham, #*P*<0.05 vs AAV6-control at day 28.

Figure 10. AAV6-miR-199a injection increases the number of cells in S-phase.

A) Schematic representation of the experimental procedure. Briefly, animals underwent ischemia-reperfusion and concomitant AAV6 injection. At day 2 after surgery, they were daily injected with BrdU until sacrifice at day 12. **B)** Representative images of BrdU immunostaining in the infarct border zone of AAV6-Control- and AAV6-miR-199a-treated animals, 12 days post MI. **C)** Quantification of BrdU-positive cardiomyocytes over the total number of cardiomyocytes in AAV6-Control and AAV6-miR-199a treated animals, 12 days post MI. Data are mean±SEM; n=3 per group; $^{*}P$<0.05. **D)** Schematic representation of the experimental procedure. Operated and injected animals received BrdU daily from day 20 to sacrifice at day 30. **E)** BrdU immunostaining in the infarct border zone of AAV6-Control- and AAV6-miR-199a-treated animals, 30 days post MI. **F)** Quantification of BrdU positive cardiomyocytes over the total number of cardiomyocytes in AAV6-Control- and AAV6-miR-199a-treated animals, 30 days pot MI. Data are mean±SEM; n=3 per group; $^{*}P$<0.05. Scale bar=100 μ m.

Figure 11. AAV6-miR-199a injection induces heart regeneration after MI by increasing cardiomyocyte proliferation.

A and **B)** Representative Ki-67 immunohistochemistry images of AAV6-Control- and AAV6-miR-199a-treated pigs 12 days after surgery, and relative quantification. Data are mean±SEM; n=3 per group; $^{*}P$<0.05. **C** and **D)** Representative Ki-67

immunohistochemistry images of AAV6-Control- and AAV6-miR-199a-treated pigs 30 days after surgery and relative quantification. Data are mean±SEM; n=3 per group; $^{*}P<0.05$. **E** and **F)** Phospho-histone 3 immunofluorescence images of pig heart sections 12 days after MI and AAV injection and relative quantification. Data are mean±SEM; n=3 per group; $^{*}P<0.05$. **G** and **H)** Phospho-histone 3 immunofluorescence images of pig heart sections 30 days after MI and AAV injection and relative quantification. Data are mean±SEM; n=3 per group. **I** and **L)** Graphs represent variations between 12 and 30 days, of the percentage of positive Ki-67 (**I**) and phospho-histone 3 (**L**) cardiomyocytes over the total number of cardiomyocytes. Data are mean±SEM; n=3. **M)** Aurora B immunofluorescence images showing localization in the nucleus or in midbodies, in AAV6-miR-199a treated animals, 12 days post MI. Scale bar= 100 μ m.

Figure 12. AAV6-miR-199a treatment significantly reduces scar size one month after ischemia-reperfusion.

A) Azan Mallory tricrome staining representative images of transverse heart sections of AAV6-Control and AAV6-miR-199a injected pig hearts one month after surgery. **B**) Quantification of infarct size. Data are mean±SEM; n=3 per group; *P<0.05. Scale bar= 250 μ m.

Figure 13. AAV6-miR-199a treatment after ischemia-reperfusion enhances GATA+ cytoplasmic localization in pig myocardium.

A and **B)** GATA4 immunohistochemistry representative images in AAV6-Contro- and AAV6-miR-199a-injected pigs, 12 days after treatment and quantification of cells showing GATA4 cytoplasmic localization (**B**). Data are mean±SEM; n=3. $^{*}P<0.05$. **C** and **D)** GATA4 immunohistochemistry representative images in AAV6-Control- and AAV6-miR-199a-injected pigs, 30 days after treatment and quantification of cells showing GATA4 cytoplasmic localization (**B**). Data are mean±SEM; n=3. $^{*}P<0.05$. **E, F, G** and **H)** Images of desmin (**E**), myogenin (**F**), endotelin receptor 1 (**G**) and Wt1 (**H**) immunohistochemistry on AAV6-Control- and AAV6-miR-199a-treated pigs, 30 days after infarction. Scale bar=100 μ m.

Figure 14. AAV6-miR-199a injection reduces cardiomyocyte area 1 month after infarction.

A) Lectin immunofluorescence and PAS staining images on sham, AAV6-Control- and AAV6-miR-199a-treated pig sections, 30 days after infarction. **B)** Cardiomyocyte cross-sectional area (μ m2) quantification of sham, AAV6-Control- and AAV6-miR-199a-treated pig sections, 30 days after infarction. Data are mean±SEM; n=3 for Sham group, n=5 for AAV6-Control and AAV6-miR-199a-treated pigs. **C)** Representative picture of sham, AAV6-Control- and AAV6-miR-199a-treated pig hearts sectioned in slices of 1 cm starting from the apex to the base. Scale bar=100 μ m.

Figure 15. AAV6-miR-199a injection reduces pathological hypertrophy up to 2 months after infarction and increases contractility.

A and **B)** MYH6/MYH7 ratio quantification by qRT-PCR, in sham, AAV6-Control and AAV6-miR-199a treated pig hearts, 12 days (**A**) and one month (**B**) after surgery. Data are mean±SEM; n=3 for 12 days, n=5 for the other time-point. $^{*}P<0.05$. **C** and **D)** BNP quantification by qRT-PCR, in sham, AAV6-Control and AAV6-miR-199a treated pig hearts, 12 days (**C**) and 1 month (**D**) after surgery. Data are mean±SEM; n=3 for 12 days, n=5 for the other time-point. $^{*}P<0.05$. **E** and **F)** ANP quantification by qRT-PCR, in sham, AAV6-Control and AAV6-miR-199a treated pig hearts, 12 days (**E**) and 1 month (**F**) after surgery. Data are mean±SEM; n=3 for 12 days, n=5 for the other time-point. $^{*}P<0.05$.

Figure 16. Long-term expression of miR-199a causes sudden death.

A) The Kaplan Meier curve represents mortality after myocardial infarction and AAV6-Control (n=6) and AAV6-miR-199a (n=7) injection. **B)** Cardiac MRI representative images of AAV6-Control and AAV6-miR-199a treated pigs, 2 days, 1 month and two months after myocardial infarction. **C)** Hematoxylin and eosin, Ki67, CD45, CD34, GATA4, desmin, myogenin, caldesmon and HHF35 immohistochemistry and immunofluorescence representative images on AAV6-miR-199a treated pig heart sections, 2 months after surgery. Scale bar = 100 µm.

Figure 17. miR-199a long-term-expression causes ventricular fibrillation.

The image represents the ECG tracked by a subcutaneously implanted recorder (Reveal Medtronic) during an episode of tachyarrhythmia evolved into ventricular fibrillation in an AAV6-miR-199a treated animal, 7 weeks after surgery.

Figure 18. Comparing different commercial lipid formulations to deliver miRNA mimic in vitro and in vivo.

A and **B)** Neonatal rat cardiomyoctes were transfected with an siRNA against the *UBC* gene, which is essential for cell viability, using different commercial lipid formulations. Three days after transfection, cell viability and toxicity were assessed by immunostaining for α-sarcomeric actinin to detect cardiomyocytes or by measuring ATP production. White bars represent the percentage of dead cell compared to the untreated control, thus indicating transfection efficiency. Black bars represent the toxicity of each lipid when delivered alone, in the absence of *UBC* siRNA. Panel **A** represents efficiency and toxicity of selected lipid formulations assessed by cardiomyocyte specific α-s sarcomeric actinin immunostaining. Panel **B** represents efficiency and toxicity of the same lipid formulations assessed by ATP production. Data are mean±SEM of 5 independent experiments; $^{*}P<0.05$, $^{**}P<0.01$. **C)** The graph represents miR-199a-3p level quantification 2 days after intracardiac injection using the indicated lipid formulations. Data are mean±SEM; n=6 per group; $^{*}P<0.05$, $^{**}P<0.01$. **D)** MiR-199a-3p target mRNA (Homer1 and Clic5) levels 2 days after intracardiac injection using the indicated lipid formulations. Data are mean±SEM; n=6 per group; $^{*}P<0.05$, $^{**}P<0.01$. **E)** MiR-199a-3p levels in the indicated organs 2 days after intracardiac injection using Lipofectamine RNAiMax (black bars). White bars represent miR-199a-3p in cel-miR-67 injected animals, thus represent miR-199a-3p endogenous levels. Data are mean±SEM; n=6 per group; $^{*}P<0.05$, $^{**}P<0.01$.

Figure 19. MiR-199a-3p mimic persistence after RNAiMax-mediated intracardiac injection.

A) Experimental workflow of the procedure. **B)** MiR-199a-3p levels in free left ventricle anterior wall, 2, 4, 8, 12 and 20 days after intacardiac injection. Grey line represents miR-199a-3p levels in cel-miR-67 injected animals, thus represent miR-199a-3p endogenous levels, while black one represents miR-199a-3p injected mice. Note that qRT-PCR

primers do not discriminate between endogenous microRNA and mimic. Data are mean±SEM; n=6 per group; $^{*}P<0.01$. **C, D, E** and **F)** Homer1 and Clic5 mRNA levels in cel-miR-67 (control) and miR-199a-3p injected hearts, 2, 4, 8, 12 and 20 days after surgery. Data are mean±SEM; n=6 per group; $^{*}P<0.01$.

Figure 20. MiR-199a-3p mimic injection improves survival and heart function parameters after myocardial infarction.

A) The Kaplan Meier curve shows mortality after myocardial infarction induction and cel-miR-67 (control, n=13, light grey) and miR-199a-3p (n=20, dark grey) mimic injection. **B, C** and **D)** Graphs represent LV ejection fraction, fractional shortening and internal diameter measured by echocardiography, 1, 2, 4 and 8 weeks after myocardial infarction and mimic injection. Data are mean±SEM; n=13 and n=20 respectively per group; $^{*}P<0.05$, $^{**}P<0.01$.

Figure 21. MiR-199a-3p mimic injection improves cardiac wall thickness after MI.

A, B and C) Left ventricular anterior wall (LVAW) thickness at end-systole and end-diastole and interventricular septum (IVS) thickness at end-diastole were assessed by echocardiography. Data are mean±SEM; n=13-20 per group; *$P<0.05$ relative to Control (cel-miR-67).

Figure 22. MiR-199a-3p mimic treatment after MI does not increase cardiomyocyte cross sectional area.

A) Representative images of cardiomyocyte cross-sectional area in non-infarcted animals and in infarcted animals after miRNA mimic treatment at day 12 after MI. **B)** Quantification of cardiomyocyte cross-sectional area relative to Control (untreated animals). Data are mean±SEM; n=6 per group; *$P<0.05$. Scale bar= 100 μ m.

Figure 23. MiR-199a-3p mimic injection reduces scar size after myocardial infarction by increasing cardiomyocyte proliferation.

A) Masson's tricrome staining representative images of transverse heart sections of cel-miR-67 (control)- and miR-199a-3p mimic-injected mice after myocardial infarction. **B)** Quantification of infarct size. Data are mean±SEM; n=13 and n=20 respectively per

group; $^{*}P<0.05$, $^{**}P<0.01$. **C** and **D)** EdU immunofluorescence representative images of myocardial infarction and cel-miR-67 (control) or miR-199a-3p mimics injected animals 12 days after surgery and relative quantification. Data are mean±SEM; n=6; $^{**}P<0.01$. **E** and **F)** Phospho-histone H3 immunofluorescence in myocardial infarction and cel-miR-67 (control)- or miR-199a-3p mimic-injected animals, 4 days after surgery and relative quantification. Data are mean±SEM; n=6; $^{**}P<0.01$. **G** and **H)** Aurora B nuclear (upper image) and in midbodies (lower image) immunostaining in myocardial infarction and miR-199a-3p mimic injected animals, 4 days after surgery and relative quantification. Data are mean±SEM; n=6; $^{**}P<0.01$. **I** and **L)** Visualization of TUNEL+ cardiomyocytes in infarcted and injected animals 2 days after surgery. Representative images (**I**) and quantification (**L**) are shown. Data are mean±SEM; n=6. Scale bar=50 μ m.

Figure 24. miR-199a-3p mimic chemical modifications increases neonatal rat cardiomyocyte proliferation.

A) List of different miR-199a-3p mimic chemical modifications and their relative commercial suppliers. **B** and **C)** EdU immunofluorescence representative images of neonatal rat cardiomyocytes 72 hours after transfection with miR-199a-3p mimics carrying chemical modifications or cel-miR-67 (Control) and relative quantification. Data are mean±SEM of 3 independent experiments. $^{**}P<0.01$. **D** and **E)** *Clic5* and *Homer1* mRNA levels in cardiomyocytes transfected with cel-miR-67 (Control) or miR-199a-3p mimics carrying chemical modifications 72 hours after treatment. Data are mean±SEM of 3 independent experiments. $^{**}P<0.01$. Scale bar= 100 μ m.

Figure 25. miR-199a-3p mimic chemical modifications stability upon intracardiac injection in mice.

A, B and **C)** Graphs represent the quantification of miR-199a-3p levels upon miR-199a-3p Dharmacon, Exiqon3 and IDT mimics intracardiac injection, 2, 8 and 21 days after surgery. MiR-199a-3p mimic levels were normalized with respect to the amount of the endogenously expressed microRNA (cel-miR-67 injected animals). Data are mean±SEM; n=6 per group; $^{*}P<0.05$, $^{**}P<0.01$. **D, E** and **F)** Homer1 and Clic5 **(G, H** and **I)** mRNA levels in the left ventricle anterior wall, 2, 8 and 21 days after intracardiac injection. Data are mean±SEM; n=6 per group; $^{*}P<0.05$, $^{**}P<0.01$.

Figure 26. MiR-199a-3p mimic IDT exerts the same beneficial effect after myocardial infarction as standard miR-199a-3p mimic.

Graphs represent LV ejection fraction **(A),** anterior wall thickness at the end of diastole **(B)** and telediastolic volume **(C)** measured by echocardiography, 1, 2, 4 and 8 weeks after myocardial infarction and mimic injection. Data are mean±SEM; n=6 per group.

TABLES

Table 1. List of reagents

Supplier:	**List of reagents:**
Applied Biosystems	TaqMan Universal PCR Master mix
BioOptica	Masson's trichrome staining kit
BioOptica	Bioclear
CORNING	96 multiwell primaria tissue culture dishes
Dharmacon	microRNAs mimic
Dharmacon	siRNAs smart pool
Dharmacon	siRNA/microRNA resuspension buffer
Exiqon	miRCURY LNA Universal RT microRNA PCR
Exiqon	ExiLENT SYBR Green Master Mix kit
Falcon	Transparent 96 multiwell tissue cultured plates
Gibco	DMEM, low glucose, GlutaMAX™ Supplement, pyruvate
Gibco	DMEM, high glucose, GlutaMAX[a] Supplement, pyruvate
Gibco	Opti-MEM I Reduced Serum Media
Invitrogen	TRIZOL
Life Technologies	Hoechst 33342
Life Technologies	Fetal bovine serum
NEST	100 mm tissue cultured dishes
PerkinElmer	ATPlite Luminescence Assay
Quiagen	RNeasy mini kits
Roche	bovine serum albumin (BSA)
Roche	MagNA Lyser Instrument
Roche	MagNA Lyser green beads
Sigma	Vitamin B12
Sigma	Trypsin
Sigma	penicillin/streptomycin
Sigma	PARAFORMALDEHYDE
Sigma	Tryton X-100
Sigma	PAS staining kit
Sigma	Eukitt mounting medium
Sigma	Ethanol
Sigma	Chloroform
Sigma	DNAse
Sigma	Eppendorf microtubes
Sigma	Xylene
Sigma	HCl
Sigma	Sodium Borate
Sigma	Tween 20
Sigma	DMSO
Sigma	BrdU
Sigma	ketamine
Sigma	xylazine

Thermo Fisher	Taqman probes for qRT-PCR
Thermo Fisher	Lipofectamine RNAiMAX Reagent
Thermo Fisher	Falcon Cell Strainers
Thermo Fisher	M-MLV Reverse Transcriptase
Thermo Fisher	Triton X-100
ThermoFIsher	Click-IT EdU 594 Imaging kit
ThermoFIsher	EdU
ThermoFIsher	ALEXA-594-α-mouse
ThermoFIsher	ALEXA-488-α-mouse
ThermoFIsher	ALEXA-594-α-Rabbit
Vectastain	ABC KIT
Vector	ImmPACT DAB

Table 2. List of primers and probes

Gene:	Probe:	Supplier:
mmu GAPDH	Mm99999915_g1	Thermo Fisher
mmu Clic5	Mm00553931_m1	Thermo Fisher
mmu Homer1	Mm00516275_m1	Thermo Fisher
rno GAPDH	Rn01775763_g1	Thermo Fisher
rno Clic5	Rn00585964_m1	Thermo Fisher
rno Homer1	Rn00581785_m1	Thermo Fisher
hsa 18S	Hs03003631_g1	Thermo Fisher
ssc GAPDH	Ss03375629_u1	Thermo Fisher
ssc HPRT	Ss03388274_m1	Thermo Fisher
ssc NNPA	Ss03394501_g1	Thermo Fisher
ssc BNP	Ss03392411_m1	Thermo Fisher
ssc MYH6	SscCIP0038305	Biorad
ssc MYH7	SscCEP0040082	Biorad
GFP	Ac03989638_mr	Thermo Fisher
Gene:	Primer mix:	Supplier:
hsa U6	339306 YP00203907	Exiqon
hsa 5S	339306 YP00203906	Exiqon
hsa-199a-3p	339306 YP00204536	Exiqon
hsa-199a-5p	339306 YP00204494	Exiqon

BIBLIOGRAPHY

1. Roger, V.L., *Epidemiology of heart failure.* Circ Res, 2013. **113**(6): p. 646-59.
2. Braunwald, E., *The war against heart failure: the Lancet lecture.* Lancet, 2015. **385**(9970): p. 812-24.
3. Packer, M., *Treatment of chronic heart failure.* Lancet, 1992. **340**(8811): p. 92-5.
4. Lymperopoulos, A., G. Rengo, and W.J. Koch, *Adrenergic nervous system in heart failure: pathophysiology and therapy.* Circ Res, 2013. **113**(6): p. 739-53.
5. Porrello, E.R., et al., *Transient regenerative potential of the neonatal mouse heart.* Science, 2011. **331**(6020): p. 1078-80.
6. Porrello, E.R., et al., *Regulation of neonatal and adult mammalian heart regeneration by the miR-15 family.* Proc Natl Acad Sci U S A, 2013. **110**(1): p. 187-92.
7. Senyo, S.E., et al., *Mammalian heart renewal by pre-existing cardiomyocytes.* Nature, 2013. **493**(7432): p. 433-6.
8. Haubner, B.J., et al., *Functional Recovery of a Human Neonatal Heart After Severe Myocardial Infarction.* Circ Res, 2016. **118**(2): p. 216-21.
9. Fratz, S., et al., *Long-term myocardial scarring after operation for anomalous left coronary artery from the pulmonary artery.* Ann Thorac Surg, 2011. **92**(5): p. 1761-5.
10. Mollova, M., et al., *Cardiomyocyte proliferation contributes to heart growth in young humans.* Proc Natl Acad Sci U S A, 2013. **110**(4): p. 1446-51.
11. Bergmann, O., et al., *Evidence for cardiomyocyte renewal in humans.* Science, 2009. **324**(5923): p. 98-102.
12. Orlic, D., et al., *Transplanted adult bone marrow cells repair myocardial infarcts in mice.* Ann N Y Acad Sci, 2001. **938**: p. 221-9; discussion 229-30.
13. Murry, C.E., et al., *Haematopoietic stem cells do not transdifferentiate into cardiac myocytes in myocardial infarcts.* Nature, 2004. **428**(6983): p. 664-8.
14. Strauer, B.E., et al., *Repair of infarcted myocardium by autologous intracoronary mononuclear bone marrow cell transplantation in humans.* Circulation, 2002. **106**(15): p. 1913-8.
15. Perin, E.C., et al., *Transendocardial, autologous bone marrow cell transplantation for severe, chronic ischemic heart failure.* Circulation, 2003. **107**(18): p. 2294-302.
16. Wollert, K.C., et al., *Intracoronary autologous bone-marrow cell transfer after myocardial infarction: the BOOST randomised controlled clinical trial.* Lancet, 2004. **364**(9429): p. 141-8.
17. Lunde, K., et al., *Intracoronary injection of mononuclear bone marrow cells in acute myocardial infarction.* N Engl J Med, 2006. **355**(12): p. 1199-209.
18. Schachinger, V., et al., *Intracoronary bone marrow-derived progenitor cells in acute myocardial infarction.* N Engl J Med, 2006. **355**(12): p. 1210-21.
19. Janssens, S., et al., *Autologous bone marrow-derived stem-cell transfer in patients with ST-segment elevation myocardial infarction: double-blind, randomised controlled trial.* Lancet, 2006. **367**(9505): p. 113-21.
20. Perin, E.C., et al., *Effect of transendocardial delivery of autologous bone marrow mononuclear cells on functional capacity, left ventricular function, and perfusion in chronic heart failure: the FOCUS-CCTRN trial.* JAMA, 2012. **307**(16): p. 1717-26.

21. Surder, D., et al., *Intracoronary injection of bone marrow-derived mononuclear cells early or late after acute myocardial infarction: effects on global left ventricular function.* Circulation, 2013. **127**(19): p. 1968-79.
22. Choudry, F., et al., *A randomized double-blind control study of early intra-coronary autologous bone marrow cell infusion in acute myocardial infarction: the REGENERATE-AMI clinical trialdagger.* Eur Heart J, 2016. **37**(3): p. 256-63.
23. Laflamme, M.A. and C.E. Murry, *Heart regeneration.* Nature, 2011. **473**(7347): p. 326-35.
24. Orlic, D., et al., *Bone marrow cells regenerate infarcted myocardium.* Nature, 2001. **410**(6829): p. 701-5.
25. Ellison, G.M., et al., *Adult c-kit(pos) cardiac stem cells are necessary and sufficient for functional cardiac regeneration and repair.* Cell, 2013. **154**(4): p. 827-42.
26. van Berlo, J.H., et al., *c-kit+ cells minimally contribute cardiomyocytes to the heart.* Nature, 2014. **509**(7500): p. 337-41.
27. Tzahor, E. and K.D. Poss, *Cardiac regeneration strategies: Staying young at heart.* Science, 2017. **356**(6342): p. 1035-1039.
28. Eschenhagen, T., et al., *Cardiomyocyte Regeneration: A Consensus Statement.* Circulation, 2017. **136**(7): p. 680-686.
29. van Laake, L.W., et al., *Human embryonic stem cell-derived cardiomyocytes survive and mature in the mouse heart and transiently improve function after myocardial infarction.* Stem Cell Res, 2007. **1**(1): p. 9-24.
30. Caspi, O., et al., *Transplantation of human embryonic stem cell-derived cardiomyocytes improves myocardial performance in infarcted rat hearts.* J Am Coll Cardiol, 2007. **50**(19): p. 1884-93.
31. Shiba, Y., et al., *Human ES-cell-derived cardiomyocytes electrically couple and suppress arrhythmias in injured hearts.* Nature, 2012. **489**(7415): p. 322-5.
32. Chong, J.J., et al., *Human embryonic-stem-cell-derived cardiomyocytes regenerate non-human primate hearts.* Nature, 2014. **510**(7504): p. 273-7.
33. Shiba, Y., et al., *Allogeneic transplantation of iPS cell-derived cardiomyocytes regenerates primate hearts.* Nature, 2016. **538**(7625): p. 388-391.
34. Anderson, M.E., et al., *Embryonic stem cell-derived cardiac myocytes are not ready for human trials.* Circ Res, 2014. **115**(3): p. 335-8.
35. Ieda, M., et al., *Direct reprogramming of fibroblasts into functional cardiomyocytes by defined factors.* Cell, 2010. **142**(3): p. 375-86.
36. Jayawardena, T.M., et al., *MicroRNA-mediated in vitro and in vivo direct reprogramming of cardiac fibroblasts to cardiomyocytes.* Circ Res, 2012. **110**(11): p. 1465-73.
37. Song, K., et al., *Heart repair by reprogramming non-myocytes with cardiac transcription factors.* Nature, 2012. **485**(7400): p. 599-604.
38. Chaudhry, H.W., et al., *Cyclin A2 mediates cardiomyocyte mitosis in the postmitotic myocardium.* J Biol Chem, 2004. **279**(34): p. 35858-66.
39. Bicknell, K.A., C.H. Coxon, and G. Brooks, *Forced expression of the cyclin B1-CDC2 complex induces proliferation in adult rat cardiomyocytes.* Biochem J, 2004. **382**(Pt 2): p. 411-6.
40. Pasumarthi, K.B., et al., *Targeted expression of cyclin D2 results in cardiomyocyte DNA synthesis and infarct regression in transgenic mice.* Circ Res, 2005. **96**(1): p. 110-8.
41. Mahmoud, A.I., et al., *Meis1 regulates postnatal cardiomyocyte cell cycle arrest.* Nature, 2013. **497**(7448): p. 249-253.
42. Bersell, K., et al., *Neuregulin1/ErbB4 signaling induces cardiomyocyte proliferation and repair of heart injury.* Cell, 2009. **138**(2): p. 257-70.

43. Reuter, S., et al., *Recombinant neuregulin 1 does not activate cardiomyocyte DNA synthesis in normal or infarcted adult mice.* PLoS One, 2014. **9**(12): p. e115871.
44. D'Uva, G., et al., *ERBB2 triggers mammalian heart regeneration by promoting cardiomyocyte dedifferentiation and proliferation.* Nat Cell Biol, 2015. **17**(5): p. 627-38.
45. Daniel J. Lenihan, S.A.A., Carrie Geisberg Lenneman, Evan Brittain, James A. S. Muldowney, Lisa Mendes, Ping Z. Zhao, Jennifer Iaci, Stephen Frohwein, Ronald Zolty, Andrew Eisen, Douglas B. Sawyer, Anthony O. Caggiano, *A Phase I, Single Ascending Dose Study of Cimaglermin Alfa (Neuregulin 1β3) in Patients With Systolic Dysfunction and Heart Failure.* JACC: Basic to Translational Science, 2016. **Volume 1**(Issue 7): p. 576-586.
46. Engel, F.B., et al., *FGF1/p38 MAP kinase inhibitor therapy induces cardiomyocyte mitosis, reduces scarring, and rescues function after myocardial infarction.* Proc Natl Acad Sci U S A, 2006. **103**(42): p. 15546-51.
47. Wei, K., et al., *Epicardial FSTL1 reconstitution regenerates the adult mammalian heart.* Nature, 2015. **525**(7570): p. 479-85.
48. Saucedo, L.J. and B.A. Edgar, *Filling out the Hippo pathway.* Nat Rev Mol Cell Biol, 2007. **8**(8): p. 613-21.
49. Pan, D., *The hippo signaling pathway in development and cancer.* Dev Cell, 2010. **19**(4): p. 491-505.
50. Heallen, T., et al., *Hippo pathway inhibits Wnt signaling to restrain cardiomyocyte proliferation and heart size.* Science, 2011. **332**(6028): p. 458-61.
51. Yamamoto, S., et al., *Activation of Mst1 causes dilated cardiomyopathy by stimulating apoptosis without compensatory ventricular myocyte hypertrophy.* J Clin Invest, 2003. **111**(10): p. 1463-74.
52. Matsui, Y., et al., *Lats2 is a negative regulator of myocyte size in the heart.* Circ Res, 2008. **103**(11): p. 1309-18.
53. Xin, M., et al., *Hippo pathway effector Yap promotes cardiac regeneration.* Proc Natl Acad Sci U S A, 2013. **110**(34): p. 13839-44.
54. Heallen, T., et al., *Hippo signaling impedes adult heart regeneration.* Development, 2013. **140**(23): p. 4683-90.
55. Xin, M., et al., *Regulation of insulin-like growth factor signaling by Yap governs cardiomyocyte proliferation and embryonic heart size.* Sci Signal, 2011. **4**(196): p. ra70.
56. Morikawa, Y., et al., *Dystrophin-glycoprotein complex sequesters Yap to inhibit cardiomyocyte proliferation.* Nature, 2017. **547**(7662): p. 227-231.
57. Bassat, E., et al., *The extracellular matrix protein agrin promotes heart regeneration in mice.* Nature, 2017. **547**(7662): p. 179-184.
58. Bartel, D.P., *MicroRNAs: target recognition and regulatory functions.* Cell, 2009. **136**(2): p. 215-33.
59. Borchert, G.M., W. Lanier, and B.L. Davidson, *RNA polymerase III transcribes human microRNAs.* Nat Struct Mol Biol, 2006. **13**(12): p. 1097-101.
60. Lee, Y., et al., *The nuclear RNase III Drosha initiates microRNA processing.* Nature, 2003. **425**(6956): p. 415-9.
61. Winter, J., et al., *Many roads to maturity: microRNA biogenesis pathways and their regulation.* Nat Cell Biol, 2009. **11**(3): p. 228-34.
62. Yi, R., et al., *Exportin-5 mediates the nuclear export of pre-microRNAs and short hairpin RNAs.* Genes Dev, 2003. **17**(24): p. 3011-6.
63. Bajan, S. and G. Hutvagner, *Another "loophole" in miRNA processing.* Mol Cell, 2011. **44**(3): p. 345-7.

64. Ruegger, S. and H. Grosshans, *MicroRNA turnover: when, how, and why.* Trends Biochem Sci, 2012. **37**(10): p. 436-46.
65. Khvorova, A., A. Reynolds, and S.D. Jayasena, *Functional siRNAs and miRNAs exhibit strand bias.* Cell, 2003. **115**(2): p. 209-16.
66. Chistiakov, D.A., A.N. Orekhov, and Y.V. Bobryshev, *Cardiac-specific miRNA in cardiogenesis, heart function, and cardiac pathology (with focus on myocardial infarction).* J Mol Cell Cardiol, 2016. **94**: p. 107-121.
67. Hata, A., *Functions of microRNAs in cardiovascular biology and disease.* Annu Rev Physiol, 2013. **75**: p. 69-93.
68. Creemers, E.E., A.J. Tijsen, and Y.M. Pinto, *Circulating microRNAs: novel biomarkers and extracellular communicators in cardiovascular disease?* Circ Res, 2012. **110**(3): p. 483-95.
69. Bernardo, B.C., et al., *miRNA therapeutics: a new class of drugs with potential therapeutic applications in the heart.* Future Med Chem, 2015. **7**(13): p. 1771-92.
70. van Rooij, E., et al., *Control of stress-dependent cardiac growth and gene expression by a microRNA.* Science, 2007. **316**(5824): p. 575-9.
71. van Rooij, E., et al., *Dysregulation of microRNAs after myocardial infarction reveals a role of miR-29 in cardiac fibrosis.* Proc Natl Acad Sci U S A, 2008. **105**(35): p. 13027-32.
72. Thum, T., et al., *MicroRNA-21 contributes to myocardial disease by stimulating MAP kinase signalling in fibroblasts.* Nature, 2008. **456**(7224): p. 980-4.
73. Li, Q., et al., *Attenuation of microRNA-1 derepresses the cytoskeleton regulatory protein twinfilin-1 to provoke cardiac hypertrophy.* J Cell Sci, 2010. **123**(Pt 14): p. 2444-52.
74. Care, A., et al., *MicroRNA-133 controls cardiac hypertrophy.* Nat Med, 2007. **13**(5): p. 613-8.
75. van Rooij, E., et al., *A signature pattern of stress-responsive microRNAs that can evoke cardiac hypertrophy and heart failure.* Proc Natl Acad Sci U S A, 2006. **103**(48): p. 18255-60.
76. da Costa Martins, P.A., et al., *MicroRNA-199b targets the nuclear kinase Dyrk1a in an auto-amplification loop promoting calcineurin/NFAT signalling.* Nat Cell Biol, 2010. **12**(12): p. 1220-7.
77. Ucar, A., et al., *The miRNA-212/132 family regulates both cardiac hypertrophy and cardiomyocyte autophagy.* Nat Commun, 2012. **3**: p. 1078.
78. Nagalingam, R.S., et al., *A cardiac-enriched microRNA, miR-378, blocks cardiac hypertrophy by targeting Ras signaling.* J Biol Chem, 2013. **288**(16): p. 11216-32.
79. Gladka, M.M., P.A. da Costa Martins, and L.J. De Windt, *Small changes can make a big difference - microRNA regulation of cardiac hypertrophy.* J Mol Cell Cardiol, 2012. **52**(1): p. 74-82.
80. Zhao, Y., et al., *Dysregulation of cardiogenesis, cardiac conduction, and cell cycle in mice lacking miRNA-1-2.* Cell, 2007. **129**(2): p. 303-17.
81. Liu, N., et al., *microRNA-133a regulates cardiomyocyte proliferation and suppresses smooth muscle gene expression in the heart.* Genes Dev, 2008. **22**(23): p. 3242-54.
82. Eulalio, A., et al., *Functional screening identifies miRNAs inducing cardiac regeneration.* Nature, 2012. **492**(7429): p. 376-81.
83. Zhao, Y., E. Samal, and D. Srivastava, *Serum response factor regulates a muscle-specific microRNA that targets Hand2 during cardiogenesis.* Nature, 2005. **436**(7048): p. 214-20.

84. Xu, T., et al., *MicroRNA-195 suppresses tumorigenicity and regulates G1/S transition of human hepatocellular carcinoma cells.* Hepatology, 2009. **50**(1): p. 113-21.
85. Liu, N., et al., *An intragenic MEF2-dependent enhancer directs muscle-specific expression of microRNAs 1 and 133.* Proc Natl Acad Sci U S A, 2007. **104**(52): p. 20844-9.
86. Olive, V., I. Jiang, and L. He, *mir-17-92, a cluster of miRNAs in the midst of the cancer network.* Int J Biochem Cell Biol, 2010. **42**(8): p. 1348-54.
87. Tiscornia, G. and J.C. Izpisua Belmonte, *MicroRNAs in embryonic stem cell function and fate.* Genes Dev, 2010. **24**(24): p. 2732-41.
88. Chen, J., et al., *mir-17-92 cluster is required for and sufficient to induce cardiomyocyte proliferation in postnatal and adult hearts.* Circ Res, 2013. **112**(12): p. 1557-66.
89. Tian, Y., et al., *A microRNA-Hippo pathway that promotes cardiomyocyte proliferation and cardiac regeneration in mice.* Sci Transl Med, 2015. **7**(279): p. 279ra38.
90. Gu, S. and W.Y. Chan, *Flexible and versatile as a chameleon-sophisticated functions of microRNA-199a.* Int J Mol Sci, 2012. **13**(7): p. 8449-66.
91. Desvignes, T., A. Contreras, and J.H. Postlethwait, *Evolution of the miR199-214 cluster and vertebrate skeletal development.* RNA Biol, 2014. **11**(4): p. 281-94.
92. Kim, S., et al., *MicroRNA miR-199a* regulates the MET proto-oncogene and the downstream extracellular signal-regulated kinase 2 (ERK2).* J Biol Chem, 2008. **283**(26): p. 18158-66.
93. Fujita, S. and H. Iba, *Putative promoter regions of miRNA genes involved in evolutionarily conserved regulatory systems among vertebrates.* Bioinformatics, 2008. **24**(3): p. 303-8.
94. Lee, Y.B., et al., *Twist-1 regulates the miR-199a/214 cluster during development.* Nucleic Acids Res, 2009. **37**(1): p. 123-8.
95. Loebel, D.A., et al., *A conserved noncoding intronic transcript at the mouse Dnm3 locus.* Genomics, 2005. **85**(6): p. 782-9.
96. Sakurai, K., et al., *MicroRNAs miR-199a-5p and -3p target the Brm subunit of SWI/SNF to generate a double-negative feedback loop in a variety of human cancers.* Cancer Res, 2011. **71**(5): p. 1680-9.
97. Sayed, D. and M. Abdellatif, *AKT-ing via microRNA.* Cell Cycle, 2010. **9**(16): p. 3213-7.
98. Rane, S., et al., *An antagonism between the AKT and beta-adrenergic signaling pathways mediated through their reciprocal effects on miR-199a-5p.* Cell Signal, 2010. **22**(7): p. 1054-62.
99. Jia, X.Q., et al., *Lentivirus-mediated overexpression of microRNA-199a inhibits cell proliferation of human hepatocellular carcinoma.* Cell Biochem Biophys, 2012. **62**(1): p. 237-44.
100. Shen, Q., et al., *Role of microRNA-199a-5p and discoidin domain receptor 1 in human hepatocellular carcinoma invasion.* Mol Cancer, 2010. **9**: p. 227.
101. Nam, E.J., et al., *MicroRNA expression profiles in serous ovarian carcinoma.* Clin Cancer Res, 2008. **14**(9): p. 2690-5.
102. Tsukigi, M., et al., *Re-expression of miR-199a suppresses renal cancer cell proliferation and survival by targeting GSK-3beta.* Cancer Lett, 2012. **315**(2): p. 189-97.
103. Wang, F., et al., *Correlation and quantitation of microRNA aberrant expression in tissues and sera from patients with breast tumor.* Gynecol Oncol, 2010. **119**(3): p. 586-93.

104. Ichimi, T., et al., *Identification of novel microRNA targets based on microRNA signatures in bladder cancer.* Int J Cancer, 2009. **125**(2): p. 345-52.
105. Magrelli, A., et al., *Altered microRNA Expression Patterns in Hepatoblastoma Patients.* Transl Oncol, 2009. **2**(3): p. 157-63.
106. Song, G., et al., *miR-199a regulates the tumor suppressor mitogen-activated protein kinase kinase kinase 11 in gastric cancer.* Biol Pharm Bull, 2010. **33**(11): p. 1822-7.
107. Murakami, Y., et al., *Regulation of the hepatitis C virus genome replication by miR-199a.* J Hepatol, 2009. **50**(3): p. 453-60.
108. Zhang, G.L., et al., *Suppression of hepatitis B virus replication by microRNA-199a-3p and microRNA-210.* Antiviral Res, 2010. **88**(2): p. 169-75.
109. Santhakumar, D., et al., *Combined agonist-antagonist genome-wide functional screening identifies broadly active antiviral microRNAs.* Proc Natl Acad Sci U S A, 2010. **107**(31): p. 13830-5.
110. Watanabe, T., et al., *Dnm3os, a non-coding RNA, is required for normal growth and skeletal development in mice.* Dev Dyn, 2008. **237**(12): p. 3738-48.
111. el Azzouzi, H., et al., *The hypoxia-inducible microRNA cluster miR-199a approximately 214 targets myocardial PPARdelta and impairs mitochondrial fatty acid oxidation.* Cell Metab, 2013. **18**(3): p. 341-54.
112. Song, X.W., et al., *MicroRNAs are dynamically regulated in hypertrophic hearts, and miR-199a is essential for the maintenance of cell size in cardiomyocytes.* J Cell Physiol, 2010. **225**(2): p. 437-43.
113. Zhang, H., et al., *Qiliqiangxin Attenuates Phenylephrine-Induced Cardiac Hypertrophy through Downregulation of MiR-199a-5p.* Cell Physiol Biochem, 2016. **38**(5): p. 1743-51.
114. Li, Z., et al., *miR-199a impairs autophagy and induces cardiac hypertrophy through mTOR activation.* Cell Death Differ, 2017. **24**(7): p. 1205-1213.
115. Haghikia, A., et al., *Signal transducer and activator of transcription 3-mediated regulation of miR-199a-5p links cardiomyocyte and endothelial cell function in the heart: a key role for ubiquitin-conjugating enzymes.* Eur Heart J, 2011. **32**(10): p. 1287-97.
116. Rane, S., et al., *Downregulation of miR-199a derepresses hypoxia-inducible factor-1alpha and Sirtuin 1 and recapitulates hypoxia preconditioning in cardiac myocytes.* Circ Res, 2009. **104**(7): p. 879-86.
117. Park, K.M., et al., *Carvedilol-responsive microRNAs, miR-199a-3p and -214 protect cardiomyocytes from simulated ischemia-reperfusion injury.* Am J Physiol Heart Circ Physiol, 2016. **311**(2): p. H371-83.
118. World Medical, A., *World Medical Association Declaration of Helsinki: ethical principles for medical research involving human subjects.* JAMA, 2013. **310**(20): p. 2191-4.
119. Weaver, M.E., et al., *A quantitative study of the anatomy and distribution of coronary arteries in swine in comparison with other animals and man.* Cardiovasc Res, 1986. **20**(12): p. 907-17.
120. Peters, M.J., et al., *Genome-wide association study meta-analysis of chronic widespread pain: evidence for involvement of the 5p15.2 region.* Ann Rheum Dis, 2013. **72**(3): p. 427-36.
121. Nikolaou, K., et al., *MRI and CT in the diagnosis of coronary artery disease: indications and applications.* Insights Imaging, 2011. **2**(1): p. 9-24.
122. Grothues, F., et al., *Interstudy reproducibility of right ventricular volumes, function, and mass with cardiovascular magnetic resonance.* Am Heart J, 2004. **147**(2): p. 218-23.

123. Zerhouni, E.A., et al., *Human heart: tagging with MR imaging--a method for noninvasive assessment of myocardial motion.* Radiology, 1988. **169**(1): p. 59-63.
124. Gotte, M.J., et al., *Myocardial strain and torsion quantified by cardiovascular magnetic resonance tissue tagging: studies in normal and impaired left ventricular function.* J Am Coll Cardiol, 2006. **48**(10): p. 2002-11.
125. Doltra, A., et al., *Emerging concepts for myocardial late gadolinium enhancement MRI.* Curr Cardiol Rev, 2013. **9**(3): p. 185-90.
126. Ikenishi, A., et al., *Cell cycle regulation in mouse heart during embryonic and postnatal stages.* Dev Growth Differ, 2012. **54**(8): p. 731-8.
127. Shapiro, S.D., et al., *Cyclin A2 induces cardiac regeneration after myocardial infarction through cytokinesis of adult cardiomyocytes.* Sci Transl Med, 2014. **6**(224): p. 224ra27.
128. Tao, Z., et al., *Coexpression of VEGF and angiopoietin-1 promotes angiogenesis and cardiomyocyte proliferation reduces apoptosis in porcine myocardial infarction (MI) heart.* Proc Natl Acad Sci U S A, 2011. **108**(5): p. 2064-9.
129. Koudstaal, S., et al., *Sustained delivery of insulin-like growth factor-1/hepatocyte growth factor stimulates endogenous cardiac repair in the chronic infarcted pig heart.* J Cardiovasc Transl Res, 2014. **7**(2): p. 232-41.
130. Hinkel, R., et al., *Inhibition of microRNA-92a protects against ischemia/reperfusion injury in a large-animal model.* Circulation, 2013. **128**(10): p. 1066-75.
131. Bellera, N., et al., *Single intracoronary injection of encapsulated antagomir-92a promotes angiogenesis and prevents adverse infarct remodeling.* J Am Heart Assoc, 2014. **3**(5): p. e000946.
132. Atchison, R.W., B.C. Casto, and W.M. Hammon, *Adenovirus-Associated Defective Virus Particles.* Science, 1965. **149**(3685): p. 754-6.
133. Bohenzky, R.A., R.B. LeFebvre, and K.I. Berns, *Sequence and symmetry requirements within the internal palindromic sequences of the adeno-associated virus terminal repeat.* Virology, 1988. **166**(2): p. 316-27.
134. Ni, T.H., et al., *Cellular proteins required for adeno-associated virus DNA replication in the absence of adenovirus coinfection.* J Virol, 1998. **72**(4): p. 2777-87.
135. Srivastava, A., E.W. Lusby, and K.I. Berns, *Nucleotide sequence and organization of the adeno-associated virus 2 genome.* J Virol, 1983. **45**(2): p. 555-64.
136. Wu, Z., A. Asokan, and R.J. Samulski, *Adeno-associated virus serotypes: vector toolkit for human gene therapy.* Mol Ther, 2006. **14**(3): p. 316-27.
137. Girod, A., et al., *The VP1 capsid protein of adeno-associated virus type 2 is carrying a phospholipase A2 domain required for virus infectivity.* J Gen Virol, 2002. **83**(Pt 5): p. 973-8.
138. Summerford, C. and R.J. Samulski, *Membrane-associated heparan sulfate proteoglycan is a receptor for adeno-associated virus type 2 virions.* J Virol, 1998. **72**(2): p. 1438-45.
139. Pillay, S., et al., *An essential receptor for adeno-associated virus infection.* Nature, 2016. **530**(7588): p. 108-12.
140. Nicolson, S.C. and R.J. Samulski, *Recombinant adeno-associated virus utilizes host cell nuclear import machinery to enter the nucleus.* J Virol, 2014. **88**(8): p. 4132-44.
141. Stahnke, S., et al., *Intrinsic phospholipase A2 activity of adeno-associated virus is involved in endosomal escape of incoming particles.* Virology, 2011. **409**(1): p. 77-83.

142. Seisenberger, G., et al., *Real-time single-molecule imaging of the infection pathway of an adeno-associated virus.* Science, 2001. **294**(5548): p. 1929-32.
143. Lux, K., et al., *Green fluorescent protein-tagged adeno-associated virus particles allow the study of cytosolic and nuclear trafficking.* J Virol, 2005. **79**(18): p. 11776-87.
144. Johnson, J.S. and R.J. Samulski, *Enhancement of adeno-associated virus infection by mobilizing capsids into and out of the nucleolus.* J Virol, 2009. **83**(6): p. 2632-44.
145. Alexander, I.E., D.W. Russell, and A.D. Miller, *DNA-damaging agents greatly increase the transduction of nondividing cells by adeno-associated virus vectors.* J Virol, 1994. **68**(12): p. 8282-7.
146. Cervelli, T., et al., *Processing of recombinant AAV genomes occurs in specific nuclear structures that overlap with foci of DNA-damage-response proteins.* J Cell Sci, 2008. **121**(Pt 3): p. 349-57.
147. Zentilin, L., A. Marcello, and M. Giacca, *Involvement of cellular double-stranded DNA break binding proteins in processing of the recombinant adeno-associated virus genome.* J Virol, 2001. **75**(24): p. 12279-87.
148. Tratschin, J.D., I.L. Miller, and B.J. Carter, *Genetic analysis of adeno-associated virus: properties of deletion mutants constructed in vitro and evidence for an adeno-associated virus replication function.* J Virol, 1984. **51**(3): p. 611-9.
149. Inagaki, K., et al., *Robust systemic transduction with AAV9 vectors in mice: efficient global cardiac gene transfer superior to that of AAV8.* Mol Ther, 2006. **14**(1): p. 45-53.
150. Zincarelli, C., et al., *Comparative cardiac gene delivery of adeno-associated virus serotypes 1-9 reveals that AAV6 mediates the most efficient transduction in mouse heart.* Clin Transl Sci, 2010. **3**(3): p. 81-9.
151. Mussolino, C., et al., *AAV-mediated photoreceptor transduction of the pig cone-enriched retina.* Gene Ther, 2011. **18**(7): p. 637-45.
152. Louboutin, J.P., L. Wang, and J.M. Wilson, *Gene transfer into skeletal muscle using novel AAV serotypes.* J Gene Med, 2005. **7**(4): p. 442-51.
153. Blankinship, M.J., et al., *Efficient transduction of skeletal muscle using vectors based on adeno-associated virus serotype 6.* Mol Ther, 2004. **10**(4): p. 671-8.
154. Sands, M.S., *AAV-mediated liver-directed gene therapy.* Methods Mol Biol, 2011. **807**: p. 141-57.
155. Wang, Z., et al., *Widespread and stable pancreatic gene transfer by adeno-associated virus vectors via different routes.* Diabetes, 2006. **55**(4): p. 875-84.
156. Rupaimoole, R. and F.J. Slack, *MicroRNA therapeutics: towards a new era for the management of cancer and other diseases.* Nat Rev Drug Discov, 2017. **16**(3): p. 203-222.
157. van Rooij, E. and E.N. Olson, *MicroRNA therapeutics for cardiovascular disease: opportunities and obstacles.* Nat Rev Drug Discov, 2012. **11**(11): p. 860-72.
158. Garzon, R., G. Marcucci, and C.M. Croce, *Targeting microRNAs in cancer: rationale, strategies and challenges.* Nat Rev Drug Discov, 2010. **9**(10): p. 775-89.
159. Chen, P.Y., et al., *Strand-specific 5'-O-methylation of siRNA duplexes controls guide strand selection and targeting specificity.* RNA, 2008. **14**(2): p. 263-74.
160. Montgomery, R.L., et al., *MicroRNA mimicry blocks pulmonary fibrosis.* EMBO Mol Med, 2014. **6**(10): p. 1347-56.
161. Chiu, Y.L. and T.M. Rana, *siRNA function in RNAi: a chemical modification analysis.* RNA, 2003. **9**(9): p. 1034-48.
162. van Rooij, E., A.L. Purcell, and A.A. Levin, *Developing microRNA therapeutics.* Circ Res, 2012. **110**(3): p. 496-507.

163. Braasch, D.A. and D.R. Corey, *Locked nucleic acid (LNA): fine-tuning the recognition of DNA and RNA.* Chem Biol, 2001. **8**(1): p. 1-7.
164. Esau, C., et al., *miR-122 regulation of lipid metabolism revealed by in vivo antisense targeting.* Cell Metab, 2006. **3**(2): p. 87-98.
165. Lennox, K.A. and M.A. Behlke, *A direct comparison of anti-microRNA oligonucleotide potency.* Pharm Res, 2010. **27**(9): p. 1788-99.
166. Levin, A.A., *A review of the issues in the pharmacokinetics and toxicology of phosphorothioate antisense oligonucleotides.* Biochim Biophys Acta, 1999. **1489**(1): p. 69-84.
167. Lionetti, V., et al., *Mismatch between uniform increase in cardiac glucose uptake and regional contractile dysfunction in pacing-induced heart failure.* Am J Physiol Heart Circ Physiol, 2007. **293**(5): p. H2747-56.
168. Bogaert, J. and F.E. Rademakers, *Regional nonuniformity of normal adult human left ventricle.* Am J Physiol Heart Circ Physiol, 2001. **280**(2): p. H610-20.
169. Warltier, D.C., et al., *Subendocardial versus transmural myocardial infarction: relationship to the collateral circulation in canine and porcine hearts.* Can J Physiol Pharmacol, 1982. **60**(12): p. 1700-6.
170. Lesizza, P., et al., *Single-Dose Intracardiac Injection of Pro-Regenerative MicroRNAs Improves Cardiac Function After Myocardial Infarction.* Circ Res, 2017. **120**(8): p. 1298-1304.
171. Zacchigna, S., L. Zentilin, and M. Giacca, *Adeno-associated virus vectors as therapeutic and investigational tools in the cardiovascular system.* Circ Res, 2014. **114**(11): p. 1827-46.
172. Kikuchi, K., et al., *Primary contribution to zebrafish heart regeneration by gata4(+) cardiomyocytes.* Nature, 2010. **464**(7288): p. 601-5.
173. Chen, D., et al., *Dual function of the UNC-45b chaperone with myosin and GATA4 in cardiac development.* J Cell Sci, 2012. **125**(Pt 16): p. 3893-903.
174. Capetanaki, Y., D.J. Milner, and G. Weitzer, *Desmin in muscle formation and maintenance: knockouts and consequences.* Cell Struct Funct, 1997. **22**(1): p. 103-16.
175. Faralli, H. and F.J. Dilworth, *Turning on myogenin in muscle: a paradigm for understanding mechanisms of tissue-specific gene expression.* Comp Funct Genomics, 2012. **2012**: p. 836374.
176. Maguire, J.J. and A.P. Davenport, *Endothelin@25 - new agonists, antagonists, inhibitors and emerging research frontiers: IUPHAR Review 12.* Br J Pharmacol, 2014. **171**(24): p. 5555-72.
177. Menke, A.L., A.J. van der Eb, and A.G. Jochemsen, *The Wilms' tumor 1 gene: oncogene or tumor suppressor gene?* Int Rev Cytol, 1998. **181**: p. 151-212.
178. Ryu, K.Y., et al., *The mouse polyubiquitin gene UbC is essential for fetal liver development, cell-cycle progression and stress tolerance.* EMBO J, 2007. **26**(11): p. 2693-706.
179. Felician, G., et al., *Epigenetic modification at Notch responsive promoters blunts efficacy of inducing notch pathway reactivation after myocardial infarction.* Circ Res, 2014. **115**(7): p. 636-49.
180. Barroso-del Jesus, A., G. Lucena-Aguilar, and P. Menendez, *The miR-302-367 cluster as a potential stemness regulator in ESCs.* Cell Cycle, 2009. **8**(3): p. 394-8.
181. Xu, S., et al., *DNA damage responsive miR-33b-3p promoted lung cancer cells survival and cisplatin resistance by targeting p21(WAF1/CIP1).* Cell Cycle, 2016. **15**(21): p. 2920-2930.

182. Qu, J., et al., *MicroRNA-33b inhibits lung adenocarcinoma cell growth, invasion, and epithelial-mesenchymal transition by suppressing Wnt/beta-catenin/ZEB1 signaling.* Int J Oncol, 2015. **47**(6): p. 2141-52.
183. Lovric, J., et al., *Terminal differentiation of cardiac and skeletal myocytes induces permissivity to AAV transduction by relieving inhibition imposed by DNA damage response proteins.* Mol Ther, 2012. **20**(11): p. 2087-97.
184. Ferrarini, M., et al., *Adeno-associated virus-mediated transduction of VEGF165 improves cardiac tissue viability and functional recovery after permanent coronary occlusion in conscious dogs.* Circ Res, 2006. **98**(7): p. 954-61.
185. Battistoni, A., S. Rubattu, and M. Volpe, *Circulating biomarkers with preventive, diagnostic and prognostic implications in cardiovascular diseases.* Int J Cardiol, 2012. **157**(2): p. 160-8.
186. Han, P., et al., *Epigenetic response to environmental stress: Assembly of BRG1-G9a/GLP-DNMT3 repressive chromatin complex on Myh6 promoter in pathologically stressed hearts.* Biochim Biophys Acta, 2016. **1863**(7 Pt B): p. 1772-81.
187. Yu, F.X., B. Zhao, and K.L. Guan, *Hippo Pathway in Organ Size Control, Tissue Homeostasis, and Cancer.* Cell, 2015. **163**(4): p. 811-28.
188. Schindler, Y.L., et al., *Hand2 elevates cardiomyocyte production during zebrafish heart development and regeneration.* Development, 2014. **141**(16): p. 3112-22.
189. Lv, H., et al., *Toxicity of cationic lipids and cationic polymers in gene delivery.* J Control Release, 2006. **114**(1): p. 100-9.
190. Cahill, T.J., R.P. Choudhury, and P.R. Riley, *Heart regeneration and repair after myocardial infarction: translational opportunities for novel therapeutics.* Nat Rev Drug Discov, 2017. **16**(10): p. 699-717.